Frustrated Magnetism in Charge Disordered Ln_2ScNbO_7 Pyrochlores

by

Cole D. MAUWS

A thesis submitted to the Facutly of Graduate Studies of
The University of Manitoba
in partial fulfillment of the requirements for the degree of

Doctor of Philosophy

Department of Chemistry
University of Manitoba
Winnipeg

UNIVERSITY OF MANITOBA

Abstract

Faculty of Science

Department of Chemistry

Frustrated Magnetism in Charge Disordered Ln_2ScNbO_7 Pyrochlores

by Cole D. MAUWS

The pyrochlore structure is well studied in the field of frustrated magnetism as it provides a platform for investigating many magnetic cations on a corner-sharing tetrahedral network. Here the rare earth charge-disordered Ln_2ScNbO_7 pyrochlores are studied as well as the last remaining member of the titanate series, $Sm_2Ti_2O_7$, for an in depth investigation of its magnetic ground state. The charge disordered pyrochlores provide an extreme example of non-magnetic chemical disorder in a frustrated rare earth system and can provide insight into the effects of disorder on underlying magnetic ground states. In the Ln_2ScNbO_7 (Ln = La, Pr, Nd, Sm, Gd, Tb, Dy) pyrochlores the non-magnetic B-site is occupied by a mixture of Sc^{+3} and Nb^{+5} ions, while leaving the magnetic sublattice nominally unchanged. Structural investigation by x-ray and neutron, diffraction and total scattering measurements show that there are significant short-range correlations between Sc^{+3} and Nb^{+5} ions that are not evident in the crystallographic results. These correlations approach charge ice correlations in the large cation members of the series, Ln = La, Pr, Nd and the correlations appear to fall off for smaller cation members of the series (with Ln = Tb as the only viable example).

Magnetic studies are presented on Ln = Nd, Gd, Dy and $Sm_2Ti_2O_7$. Ising antiferromagnetism is observed in Nd_2ScNbO_7 alongside diffuse scattering indicative of moment fragmentation. A glassy magnetic ground state is observed in Gd_2ScNbO_7 although emergent xy spin ordering, similar to the parent compounds, is observed on a short length scale. Differing from the parent compounds, Dy_2ScNbO_7 is not a classical spin ice, and instead freezes into a glassy ground state with on average isotropic spins. Despite nominally having the single ion symmetry requirements for moment fragmentation, $Sm_2Ti_2O_7$ does not show signatures of the phenomenon; instead a well ordered Ising antiferromagnetic ground state is observed. Although discussions of non-magnetic disorder are usually limited to structural distortions altering exchange interactions, these systems show that in rare earth pyrochlores the distortion of the local crystal field environments is equally relevant to structural distortions and can fundamentally change the single ion symmetry and anisotropy of the rare earth ions. The lack of a universal single ion symmetry changes how these rare earth systems need to be approached in comparison to how rare earth systems are normally treated. The single ion symmetry and anisotropy typically restricts the possible magnetic ground states. Comparisons to spin-glass systems can be drawn in the Gd_2ScNbO_7 and Dy_2ScNbO_7 cases. However, in Dy_2ScNbO_7 the mechanistic differences to conventional diluted magnetic ion spin-glasses may necessitate study into something akin to anisotropy-disordered magnetic glasses, which to our knowledge have not been studied theoretically in rare earth pyrochlore systems.

Contents

List of Figures

Chapter 1

Introduction

1.1 Motivation

The field of quantum materials focuses on elucidating new states of matter in order to develop a better understanding of unconventional phenomena. The work in this field could potentially lead to the development of a new technological revolution through so called quantum devices. It is a broad field that encompasses the study of varied phenomena including; the Mott transition, superconductivity, topological insulators, colossal magnetoresistance, multiferroics, heavy fermion metals, the fractional quantum Hall effect and magnetic frustration [1–5]. The synthesis and structural characterization of new and existing quantum materials is a fruitful research area for solid state chemists [6].

Magnetic frustration, the focus of this thesis, is the study of magnetic systems under competing interactions that inhibit long-range magnetic order, or induce magnetic order through unconventional interactions leading to new physical phenomena. These competing interactions can include; lattice geometries, chemical disorder, single ion electronic properties, and competing inter-ion magnetic interactions. Some combinations of these interactions can allow for strong coupling between magnetic moments over short and long-range distances, without forming periodically ordered magnetic states. These spin liquid and spin glass states can present interesting physics including the formation of new quasiparticles [7, 8].

Crystalline disorder or semi-crystalline materials affect a broad range of phenomenon in materials science, but quantum materials tend to have particularly dramatic responses to disorder and defects. These responses to disorder can range

from topological insulators which are not affected by disorder due to symmetry protections, to type II superconductors which often require small amounts of chemical doping to exhibit superconductivity [9]. While chemical disorder has been studied extensively in these systems, its role in magnetic frustration is less robustly understood, despite many interesting magnetically frustrated systems showing chemical disorder [10–14].

The goal of this project is to investigate the magnetic ground states of several rare earth pyrochlores to search for new phases in quantum matter. In particular, the Ln_2ScNbO_7 (Ln = La, Pr, Nd, Sm, Gd, Tb, Dy) pyrochlores are studied to determine how their intrinsic charge disorder impacts the underlying magnetism of these magnetically frustrated systems. Additionally, the magnetic ground state of $Sm_2Ti_2O_7$ is investigated, which is the last member of the $Ln_2Ti_2O_7$ series that until now has not had an extensive investigation of its magnetic ground state.

1.2 Pyrochlores

TABLE 1.1: Wyckoff positions of the pyrochlore unit cell, in the $Fd\bar{3}m$ unit cell (unit cell origin 2) [15].

Atom	Site	x (r.l.u.)	y (r.l.u.)	z (r.l.u.)
Ln(III)	16d	$\frac{1}{2}$	$\frac{1}{2}$	$\frac{1}{2}$
B(IV)	16c	0	0	0
O	8b	$\frac{3}{8}$	$\frac{3}{8}$	$\frac{3}{8}$
O	48f	x	$\frac{1}{8}$	$\frac{1}{8}$

The pyrochlore structure is named after the isostructural mineral $(Na,Ca)_2Nb_2O_6(OH)$, with the general formula $A_2B_2X_6X'$. The pyrochlore structure is typically reported by its cubic unit cell with space group $Fd\bar{3}m$. The sites within the unit cell are reported in table 1.1, where the x parameter of O_{48f} can range from x = 0.3125 to x = 0.375 as these positions form either an octahedron around the B-site or a cube around the A-site respectively (the parameter typically ranges from x = 0.32 to x = 0.345 [15]). Figure 1.1 shows the pyrochlore structure consisting of distorted cubic environments around the A-site and distorted octahedral local environments around the B-site, each

with D_{3d} local symmetry. From the perspective of magnetic frustration, the fact that each site forms a network of corner sharing tetrahedra is of interest as a frustrated geometry. Figure 1.1 (b, c) shows the A-site network of tetrahedra, with the O_{8b} site sitting at the centre of each tetrahedron.

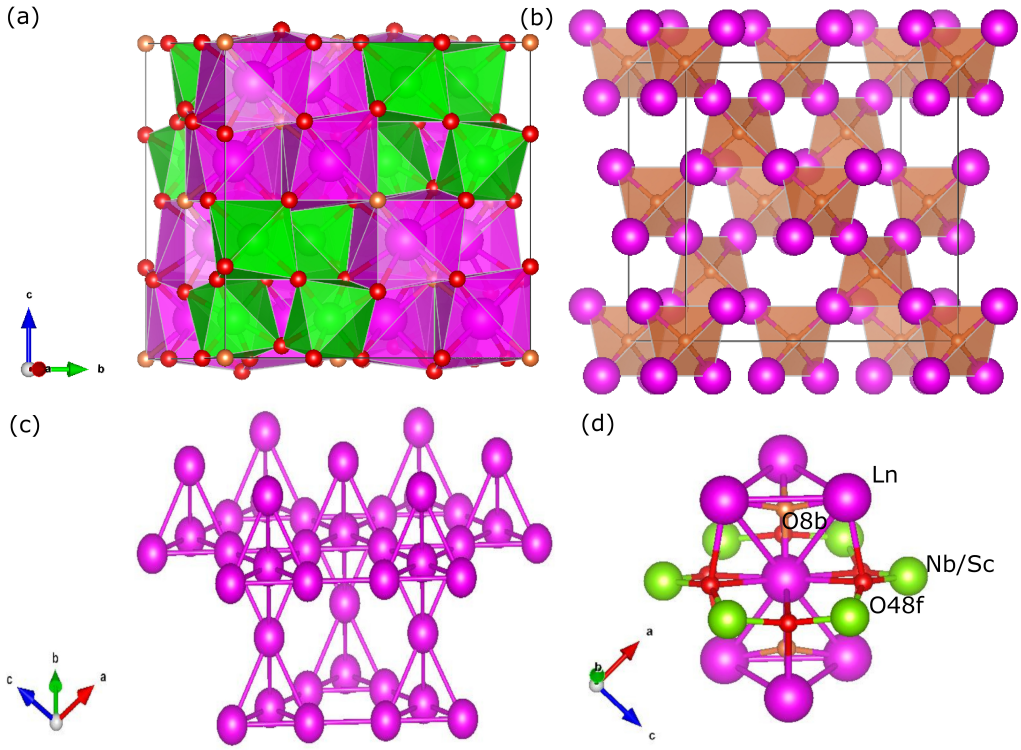

FIGURE 1.1: The cubic $Fd\bar{3}m$ pyrochlore structure shown from various perspectives. (a) The unit cell with all of the atomic positions, Ln^{+3} (purple), B^{+4} (green), O_{48f} (red), and O_{8b} (orange). (b) The connectivity of the A-site, forming a network of corner sharing tetrahedra, with O_{8b} sites in the centre of each tetrahedron. (c) Another angle of the A-site connectivity, with the (1,1,1) direction projected upward, emphasizing the planes of connected hexagons and triangles fromed by the tetrahedra. (d) The local configurations of two A-site tetrahedra, with a surrounding hexagon of B-site ions connected through O_{48f} ions.

While the pyrochlore structure encompasses a broad class of materials, this work will focus on the rare earth pyrochlores with a lanthanide (Ln) on the A-site and non-magnetic transition metals on the B-site, with the form $Ln_2^{+3}B_2O_7$. Figure 1.2 roughly outlines the stability regime of the pyrochlore structure by the relative cation radii. When r_{Ln}/r_b is too small ($\lessapprox 1.36$) the cations mix sites and a defect fluorite is formed. When r_{Ln}/r_b is too large ($\gtrapprox 1.71$) a monoclinic distortion is typically introduced, destroying the tetrahedral symmetry of the cations. It is possible to extend beyond these conventional limits using high pressure techniques that allow for larger r_{Ln}/r_b

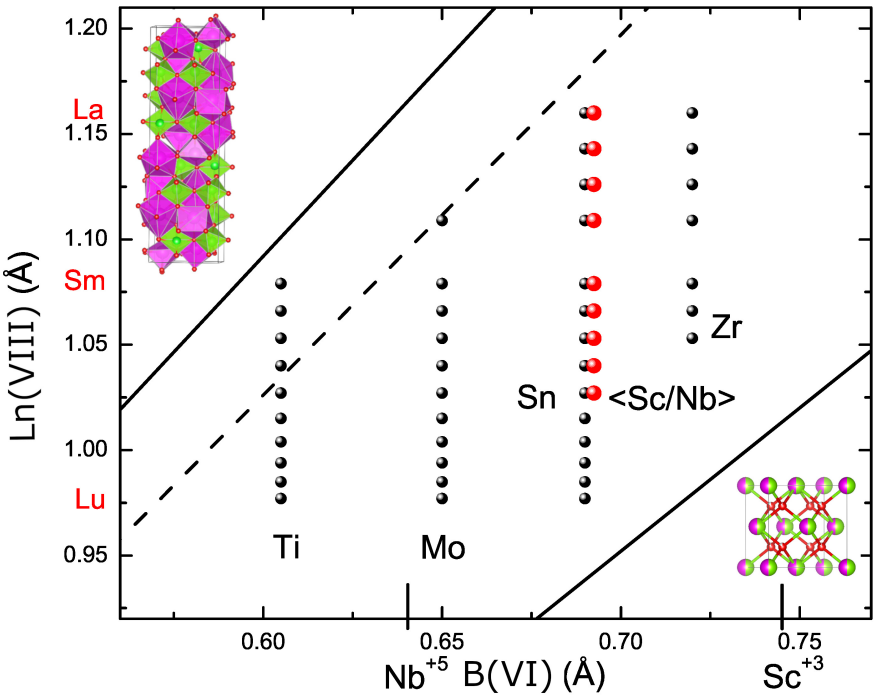

FIGURE 1.2: A non-complete phase stability diagram of the rare earth pyrochlores. Radii are reported as ionic radii [16]. Various series are labeled by their B-cation. The radii of Nb^{+5} and Sc^{+3} are reported on the B-site axis with the series placed on the mean radii of Sc^{+3} and Nb^{+5}. Labeled structures are the common resulting structures on either side of the phase stability region, a monoclinic distortion (top-left) and the cation-disordered defect fluorite structure (bottom-right). Lines represent reported limits of the phase stability, with the dashed line being the conventionally reported upper limit and the solid upper line representing the upper limit. Figure is modified from Gardner *et al.* [15].

[17].

The work here will focus largely on the Ln_2ScNbO_7 pyrochlores where the B-site, typically a +4 cation, is split with mixed occupancy between Sc^{+3} and Nb^{+5}. The $Ln_2Sn_2O_7$ pyrochlores can be formed with any lanthanide, due to the middling size of Sn^{+4} (0.69 Å) compared to other B-site ions that form the pyrochlore structure. Despite (Sc/Nb) having a similar average radius to Sn^{+4} the Ln_2ScNbO_7 pyrochlores cannot be formed with cations smaller than Dy^{+3}, likely due to the oversized Sc^{+3} [18].

1.3 Frustrated Magnetism in Rare Earth Pyrochlores

The interest of frustrated magnetism on the pyrochlore lattice began with the theory of the Heisenberg antiferromagnet on the pyrochlore lattice. Early theories predicted that this configuration would give rise to a spin liquid with no finite freezing temperature [19]. This was later revised by Palmer and Chalker [20] to show that real systems under these conditions would undergo magnetic long-range order. However the discovery of spin-ice on the pyrochlore lattice spurred additional investigation into rare earth pyrochlore magnetism. Further theoretical work would also push for research into the smaller moment lanthanides on the pyrochlore lattice for various quantum phenomena.

To understand magnetism in rare earth pyrochlores, three underlying factors need to be considered; the geometry of the lattice (Fig. 1.1), the anisotropy and symmetry of the ground state crystal field (Fig. 1.3), and the interaction of the exchange Hamiltonian, which can also include classical dipole-dipole interactions.

Crystal fields in rare earth compounds typically need to be considered under the weak field case, where the ground state is predominantly composed of the Hund's value of the total angular momentum J; J = L - S for less than half-filled shells, J = L + S for greater than half-filled shells, typically written as $^{2S+1}L_J$. This ground state has a multiplicity of 2J+1 in the free ion case. Only then is the Hund's ground state multiplet split by the crystal electric field, typically in the range of 1-200 meV for lanthanide oxides. Crystal electric fields are a perturbation on electronic energies induced by the electric potential exerted by neighboring ions. The energy scale of this perturbation is typically larger in transition metal systems, but in f-electron systems there is significant shielding from the valence electrons lowering the energy scale of the crystal electric field.

Normally, the symmetry of crystal fields can be described as point group symmetries. A point group is a closed group that categorizes the possible ways a point can transform under rotation, mirror, inversion and unity symmetries. The possible symmetry representations of a point group (or the other group sets that will be discussed here) can be described as a linear combination of irreducible representations. For

crystal fields, each set of energy levels can be described by these irreducible representations. Herein the irreducible representations of various systems will be described for point groups, double groups and space groups, which fundamentally describe how that orbital, spin-state, or vector transform under the symmetry operations of its group. This can prove useful for simplifying underlying properties of a system, such as which exchange interactions are symmetry-allowed, differentiating between symmetrically distinct magnetic grounds states which may look similar visually, or generally simplifying fitting methods by reducing the parameter space.

As some of the rare earth ions have half integer J-values conventional point group symmetries cannot be used for describing their crystal electric field, as a C_1 full rotation is not an identity operator. This can be shown as the character (χ) for the rotation of a spin j is $\chi(\alpha) = \frac{sin(\alpha(j+\frac{1}{2}))}{sin(\frac{\alpha}{2})}$ for a rotation of α. If α is 2π and j is $\frac{1}{2}$, χ is indeterminate instead of one as would be expected of an identity operator (as assumed by point group symmetry)[21]. Instead, the double groups are used to describe the crystal field ground states, which introduce the symmetry operator of time inversion, doubling the size of each point group to account for half-integer spin systems. An important symmetry result of this is that each half-integer spin has a lowest allowed symmetry of a doublet in the absence of a magnetic field, and therefore must be magnetic. The single integer spins can be magnetic or non-magnetic dependant on the ground state crystal field. The magnetic irreducible representations of the D_3 double group are Γ_3 for integer spins and Γ_4 and $\Gamma_{5,6}$ for half-integer spins.

The Landé g-factor describes the coupling between spin and orbital moments of an electron system to a small, external magnetic field, giving the effective magnetic moment; $\mu_J = Jg_J\,\mu_B$. The spin-orbit coupling that occurs due to these crystal field splittings also introduces magnetic anisotropy, a directional preference of the magnetic moment creating a Landé g-factor tensor, instead of the typical scalar; $\vec{\mu_J} = \overline{g_J}\vec{J}\,\mu_B$. In the D_{3d} symmetry this simplifies to a two-component Landé g-factor such that $\mu = -\mu_B[g_z\hat{z}J^z + g_{xy}(\hat{x}J^x + \hat{y}J^y)]$ [22], using a common literature convention that treats J^i as a pseudo-spin 1/2 (as these magnetic systems are typically doublets) that places the moment magnitude on g_i. These anisotropies often strongly prefer one of the two directions g_z or g_{xy} which are depicted in figure 1.3. These two depictions show the dominant g_{xy} case, just called the xy case, and the dominant g_z case, called

the Ising case. These directional preferences affect not only the response to an external magnetic field, but also dictate moment directions in a magnetically ordered system.

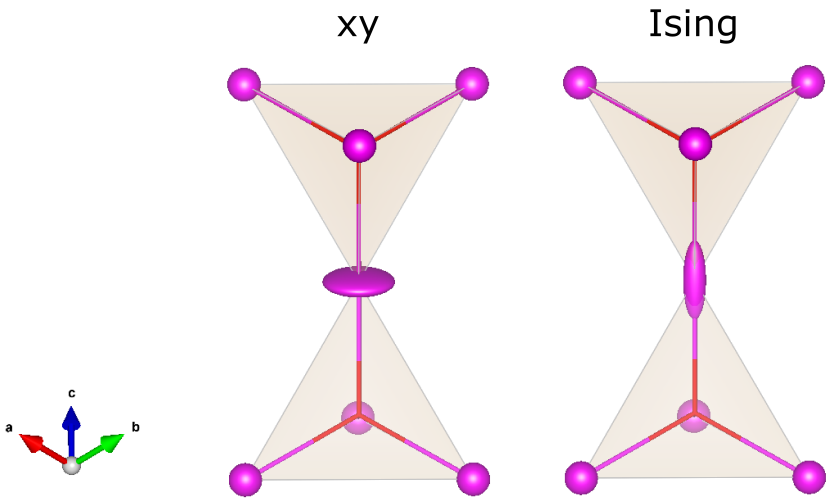

FIGURE 1.3: The central atom shows the prominent anisotropies in the pyrochlore lattice, either along or normal to the primary Ising axis, which is along the local (111) axis.

The ground state crystal field symmetry also affects the magnetic exchange Hamiltonian (see Rau and Gingras (2019) [22] for a more comprehensive review). Briefly, ignoring classical dipole-dipole and higher order multipole interactions an exchange Hamiltonian can be written as

$$H = \sum_{ij} \vec{S}_i \overline{J_{ij}} \vec{S}_j + b_{ii} \tag{1.1}$$

where $\overline{J_{ij}}$ is an order-2 tensor connecting the pseudo-spin 1/2 vectors, and the constant b_{ii} is due to the single ion crystal field. Due to symmetry constraints J_{ij} has at most 4 independent terms depending on the underlying crystal field ground state in this dipole exchange simplification.

Of interest here (chapters 4 and 7) is the $\Gamma_{5,6}$ crystal field symmetry, also called the dipole-octupole symmetry as S_x transforms under symmetry as an octupole ($C_2 : S_x \Rightarrow S_x$) [23]. This symmetry yields a Hamiltonian that can be simplified to

$$H_{di-oct} = \sum_{ij} [\tilde{J}_x \tilde{S}_i^x \tilde{S}_j^x + \tilde{J}_y \tilde{S}_i^y \tilde{S}_j^y + \tilde{J}_z \tilde{S}_i^z \tilde{S}_j^z] \tag{1.2}$$

[24]. Although it should be noted here that $\tilde{x}$ and $\tilde{z}$ are not Cartesian $\hat{z}$ and $\hat{x}$ (this 'pseudospin rotation' is explained in Benton (2016) [24]). This becomes important as

in the Ising case, one would expect J_y and J_x to be zero, instead $\tilde{J}_x$ is non-zero giving a two-component Hamiltonian.

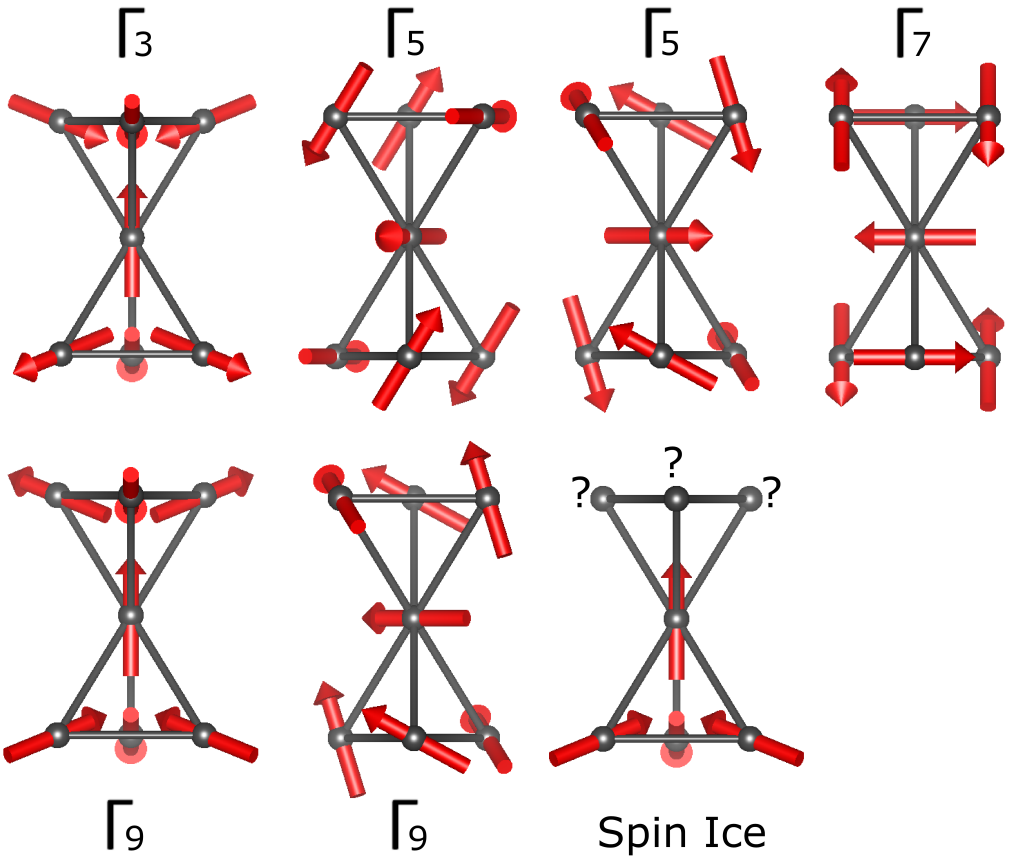

FIGURE 1.4: The **k** = (000) ordered states of the pyrochlore lattice, as well as a graphic for disordered spin ice. Γ_i represents the irreducible representation of the Fd$\bar{3}$m unit cell that each ordered state belongs to. Although $\Gamma_5^{\phi(2,3)}$, $\Gamma_7^{\phi(4,5,6)}$, $\Gamma_9^{\phi(7-12)}$ have multiple basis vectors (where ϕ are the bases), only those that are visually distinct are shown.

To describe the magnetic ground state structures, irreducible representations of the space group are commonly used. Similar to crystallographic symmetries, irreducible representations dramatically reduced the parameterization of magnetic structure determinations and also relates back to the underlying physics of the system. Magnetic structures are defined by a propagation vector **k**, that describe the periodicity of the magnetic structure relative to an underlying structural unit cell. A propagation vector of **k** = (000) would indicate a magnetic structure that maps directly onto the underlying unit cell. While rare earth pyrochlores can have non-(000) propagation vectors [25], the ordered systems typically show **k** = (000) propagation vectors. Within the Fd$\bar{3}$m unit cell for the 16c rare earth ion there are 4 possible irreducible representations and the possible magnetic orderings are spanned

by 12 sets of basis vectors. Figure 1.4 illustrates these magnetic ground states. While this only depicts a subset of the basis vectors, taking linear combinations of these vectors will span all symmetry allowed magnetic configurations. Typically however, only linear combinations of basis vectors within an irreducible representation occur. Considering the span of these vectors, these states can be loosely defined; Γ_3 is an Ising antiferromagnet, Γ_5 is an xy antiferromagnet with free rotation within the xy plane, Γ_7 is an xy antiferromagnet with vectors fixed to the (110) crystallographic direction (in a fully ordered system), and Γ_9 covers ferromagnetic structures of multiple anisotropies.

TABLE 1.2: General information for rare earth pyrochlore magnetism. Ions with nonmagnetic, singlet ground states are excluded. CEF G.S. I.R. refers to the ground state (G.S.) irreducible representation (I.R.) of the crystal electric field (CEF) ground state in the $\overline{D_3d}$ double group. G.S. Anisotropy represents the anisotropy of the ground state, 'mixed' systems have weak anisotropies, whereas 'none' refers to a spin only system. The Magnetic G.S. I.R. refers to the irreducible representations of the typical magnetic ground state in the $Fd\bar{3}m$ space group, SI refers to a spin ice system. [15, 22, 26–29]

Ion (+3)	J	CEF G.S. I.R.	μ_{total} (μ_B)	G.S. Anisotropy	Magnetic G.S. I.R.
Ce	5/2	$\Gamma_{5,6}$	2.5	z	none
Pr	4	Γ_3	3.6	z	none
Nd	9/2	$\Gamma_{5,6}$	3.6	z	Γ_3
Sm	5/2	$\Gamma_{5,6}$	0.8	z	Γ_3
Gd	7/2	multiplet	7.9	none	mixed
Tb	6	Γ_3	9.7	mixed	mixed
Dy	15/2	$\Gamma_{5,6}$	10.6	z	SI
Ho	8	Γ_3	10.6	z	SI
Er	15/2	Γ_4	9.6	xy	mixed Γ_5,Γ_7
Yb	7/2	Γ_4	4.5	mixed	Γ_9

In addition to ordered magnetic states on the pyrochlore lattice, there are disordered liquid-like phases which tend to be of greater interest [7, 30]. The best studied of these systems is the U(1) classical spin liquid, the classical spin ice (Fig. 1.4). This spin ice phase can be seen as a disordered version of the Γ_9 structure, that is induced due to the near-degeneracy of different tetrahedral coordinations. Each tetrahedron in spin ice is ordered ferromagnetically to the greatest extent possible in the Ising manifold, however for each tetrahedron there is a 6/16 degeneracy in each tetrahedron. This leads to a characteristic residual entropy that characterizes the system, $\frac{R}{2}ln(\frac{3}{2})$, often called the Pauling entropy. The classical spin ice phase is present in the

large moment Ising pyrochlore systems, the 'classical' descriptor comes from the fact that direct dipole-dipole interactions as opposed to exchange interactions dominate the spin interactions [31]

$$H_{dipolar} \approx \frac{5}{3}(\frac{\mu_0}{4\pi})\frac{\mu^2}{r_{nn}^3} \tag{1.3}$$

where μ_0 is the magnetic constant, μ is the moment magnitude of the spin and r_{nn} is the nearest neighbor distance between spins. With an energy scale on the order of 2-3 K, this ferromagnetic interaction typically outweighs nearest-neighbor antiferromagnetic exchange interactions. Spin ices that are driven by exchange are also sought after, $Yb_2Ti_2O_7$ does satisfy this ordering into the Ising Γ_9 structure. A 'quantum' variant is also sought after, that remains dynamic at all finite temperatures [30]. In general there are ongoing investigations of many disordered magnetic states in pyrochlores. Table 1.2 gives a summary of the single ion and magnetic ground states of relevant magnetic lanthanides on the pyrochlore lattice. Some of these ions show different ground states depending on the particular ion present, such as Tb^{+3} and Gd^{+3}. J. Gardner *et al.* (2010) [15] provides a review of pyrochlore magnetism.

1.4 Chemical Disorder in Magnetically Frustrated Systems

To preface a discussion on chemical disorder in frustrated systems, it is useful to consider Herbertsmithite, $ZnCu_3(OH)_6Cl_2$. Herbersmithite is one of the best studied and most exciting materials in frustrated magnetism [32]. As a spin-1/2 system on a 2-dimensional kagome lattice, it is a model system of the 2-D Heisenberg antiferromagnet on the kagome lattice, and of particular interest as it is a directly solvable theoretical model that yields a quantum spin liquid under conditions present in Herbertsmithite. Extensive theoretical and experimental work has been performed on Herbertsmithite, confirming that it is a quantum spin liquid (see M. Norman, 2016 [32] for a review). The key result is the observation of 2-D spinons, fractionalized excitations that had only been previously observed in 1-D systems [33]. Although early work considered Herbertsmithite as an idealized system in experimental interpretations, there is a large amount of chemical disorder. The copper ions site mix with the zinc ions, the real structure and composition is $(Zn_{0.85}Cu_{0.15})Cu_3(OH)_6Cl_2$. This formula places a significant amount of magnetic ions into interstitial sites between

the 2-D kagome planes in a disordered fashion [10]. This inherently leads to some skepticism of the experimental results that may be influenced by these inconsistently correlated interstitial copper ions. Increasingly advanced experiments have since resolved this issue, confirming the gapped quantum spin liquid behaviour while accounting for ion disorder, but the experimental contributions of this chemical disorder are certainly non-trivial [34].

The impact of disorder and the questions it presents extends well beyond Herbertsmithite. Another more recent example lies in $YbMgGaO_4$, which presents a 2-dimensional triangular lattice showing spin liquid signatures, with interstitial sites populated randomly by non-magnetic Mg^{+2} and Ga^{+3} [35]. Initial attempts have been made to model the effect of this disorder on the electronic and magnetic ground states, but further work remains to be done [36].

In the case of rare earth pyrochlores, multiple debates that question the impact of chemical disorder on magnetic ground states are still ongoing. The spin liquid $Tb_2Ti_2O_7$ has been studied under the effects of doping $Tb_{2+x}Ti_{2-x}O_{7-\delta}$ by T. Taniguchi *et al.*, 2013 [12] and E. Kermarrec *et al.*, 2015 [13]. At very small levels of doping (x < 0.01) there is a transition between a spin-liquid phase and a long-range ordered magnetic phase. However there is disagreement as to whether the stoichiometric $Tb_2Ti_2O_7$ falls into the long-range ordered or spin-liquid phase, and to whether or not the long-range phase is a true phase transition, or a spin liquid system with particularly long correlation lengths (~ 10 Å). Additionally pyrochlores can suffer from anion disorder, where the 8b oxygen occupies the 8a site at the centre of the B-site tetrahedra, altering the local A-site coordination environment. This is prominent in the $Ln_2Zr_2O_7$ pyrochlores [37, 38], and in the $Ln_2Hf_2O_7$ pyrochlores [39]. Various site mixing effects can lead to large sample dependencies in systems such as $Pr_2Zr_2O_7$ [40], $Tb_2Ti_2O_7$ [12, 13] or $Yb_2Ti_2O_7$ [41]. Even in relatively well behaved pyrochlore systems like $Ho_2Ti_2O_7$, a classical spin ice, doping studies that induce cation disorder can be used to investigate the change of magnetic correlations and dynamics, including the gradual destruction of the spin ice state under doping [42, 43].

More recently, charge disordered pyrochlores are becoming of interest. Similar to the chemical disorder present in $YbMgGaO_4$ (where a non-magnetic site is shared by a +2 and +3 ion with random occupancy), in the charge disordered pyrochlores

the nonmagnetic site is split into two ions of different valence. The best investigated of these systems are the $AA'B_2F_7$ pyrochlores where A is an alkali metal and A' is an alkali earth metal, which allows for magnetic +2 transition metals to be placed on the pyrochlore B-site. Some examples include $NaSrMn_2F_7$, $NaCaFe_2F_7$ [44], and $NaCaCo_2F_7$ [45]. $NaCaCo_2F_7$ in particular has attracted interest as it remains disordered to well below its Weiss temperature, forming xy antiferromagnetic clusters [45].

Materials with similar chemical disorder exist for rare earth pyrochlores, with the form $A_2BB'O_7$ where B = Sc^{+3}, Ga^{+3}, In^{+3} and B' = Nb^{+5}, Sb^{+5} [46, 47]. While this is not necessary for the inclusion of magnetic ions, instead yielding the same average charge (+4) of the parent compounds, it allows for a more direct comparison of these pyrochlores to their parent compound. This configuration of the B-site opens up multiple new series of rare earth pyrochlores to explore. Some initial reports on the magnetic properties of Dy_2ScNbO_7 [48], Yb_2GaSbO_7 [49] and NMR studies of the Ln_2GaSbO_7 pyrochlores [50] have been published. Although limited, by and large, these reports suggest behaviour similar to the parent $Ln_2B_2O_7$ pyrochlores, such as an apparent observation of classical spin ice behaviour in Dy_2ScNbO_7 [48].

This thesis explores the structural and magnetic ordering of the Ln_2ScNbO_7 pyrochlores, and shows that these pyrochlores deviate dramatically from their parent $Ln_2B_2O_7$ pyrochlores in both their electronic and magnetic ground states. Additionally, the last magnetic member of the $Ln_2Ti_2O_7$ series to see extensive research into its magnetic ground state, $Sm_2Ti_2O_7$, is also investigated.

Chapter 2

Methods

2.1 Ceramic Synthesis and Crystal Growth

Solid state preparation of ceramics, metals and intermetallics is a unique area of synthesis. Although perhaps simpler than many solution reactions, there are unique considerations that have to be taken into account due to the mechanistically distinct nature of these reactions. Reaction between primary or binary (M or MX_y) reagents is often favorable due to the increased electronic packing efficiency that can be accomplished in more complex mixtures. However, chemical reactions between solids typically do not occur spontaneously on any reasonable time scale, due to the slow kinetics of the reaction [51]. As these reactions are kinetically limited, solid state reactions are limited by temperature and surface area contact between the solid reagents [51]. The temperatures of these reactions are often >1000 (°C), or even higher for the reaction of the rare earth metals relevant here. The reagents are typically ground together in a mortar and pestle in order to reduce the particle size, increasing surface area and helping to efficiently mix the particles. Mixing is sometimes aided by grinding the particles in a slurry of volatile solvent such as methanol. Additionally, pressure is often applied to the mixed powder in order to cause the particles to pack efficiently, increasing the contact between the flat faces of particles.

Solid state reactions can be done under air or in a controlled atmosphere, but even in air the high temperatures reached can result in a spontaneous reduction of metal species. Although high temperatures are ideal for solid state reactions, reduction of metal species and incongruent melting or sublimation of some reagents typically dictate an upper temperature limit to solid state reactions. An additional

consideration for solid state reactions is the vessel the reactions are performed in, as most species are reactive at these high temperatures. Although platinum or other noble metals are ideal as crucibles for solid state reactions, other ceramics including Al_2O_3 and SiO_2 are often used for convenience. Minimal contact between the reactants and the crucible is desirable (another benefit of pressing the powder mixture instead of reacting a loose powder). One has to remain conscious of the possibility that reaction with the crucible could still occur to a significant degree.

It is possible to grow single crystals of metals and ceramics in multiple ways. In this thesis, the optical floating zone, or zone melting method is used. This is typically employed as a 'self-flux' mode, which means growing a crystal from a melt of the same composition as the final product. A Quantum Design Image Furnace is used in this work for crystal growth. Typically, powders of the desired material are pressed into two rods with a diameter of roughly 8 mm. The rods are suspended by wires within a quartz tube. Lamps with concentric mirrors focus light into a small roughly spherical region with a diameter of roughly 1 cm, heating a small region of the rods. The rods of materials, consisting of an upper 'feed rod' and lower 'seed rod' are melted in this focusing region and joined together by a melt. The rods are counter rotated against each other to improve mixing of the small volume melt, and the rods are slowly lowered at rates of 1-10 mm/h. Crystallization occurs as the 'seed rod' is lowered out of the melt, with the melt being continually supplied with new material from the 'feed rod'. This is an ideal method of growing materials that are congruently melting, which melt within a wide range of high temperatures (500-2500 or higher °C). Similar to methods like Czochralski crystal growths, the floating zone method offers two main advantages over other melt techniques; (1) they are run without a crucible in contact with the melt preventing any contamination, and (2) they have a controllable atmosphere as the quartz reaction tube is sealed away from the heat source of the lamps. This method is known for producing high purity materials as the 'moving melt' can remove impurities from the crystalized product [52].

2.2 Diffraction

Scattering techniques are powerful tools for investigating structures in condensed matter. Although these techniques can be applied to any condensed matter system, they are conventionally used on crystalline systems. The periodicity of a crystal vastly simplifies the scattering equation as it leads to constructive interference of the scattered wave at discrete points and yields a relatively simple means of calculating the scattering pattern from an assumed crystal unit cell. Optimization of an assumed crystalline unit cell to match an experimental scattering pattern through a least-squares refinement yields a crystalline structure. X-ray diffraction experiments on single crystal or powder samples are the most common uses of diffraction, allowing for the determination of molecular and extended solid structures. Additionally, probes such as electrons and neutrons can be used in diffraction to change the scattering interaction. Neutrons in particular allow for the determination of magnetic structures in a similar way to atomic structures as neutrons have a magnetic moment that can diffract off of a periodic magnetic field. Atomic structures can also be determined by neutrons, and neutron diffraction is typically employed to change the contrast of atoms in a structure. Neutrons scatter off of nuclei and not electric fields, changing the scattering power of elements in the sample, and allowing for distinction between elements that may appear similar to an X-ray probe.

In the following sections, techniques of diffraction on non-crystalline, crystalline and magnetic samples will be discussed for both neutrons and X-rays.

2.2.1 Formalism

Generically, atomic diffraction occurs when a probe wavevector ($\vec{k}$) with a wavelength similar to interatomic spacings ($\sim$ 0.1-10 Å) scatters off a sample giving an outgoing wavevector ($\vec{k'}$). If the scattering sample is comprised of a periodic scattering density $\rho(r)$, constructive interference is observed at particular scattering angles between $\vec{k'}$ and $\vec{k}$. This is commonly presented in the simple expression of Bragg's law [53]:

$$2dsin\theta = n\lambda \tag{2.1}$$

Where d is the periodicity of the scattering sample, θ is half of the scattering angle between the wavevectors $\vec{k}$ and $\vec{k'}$, λ is the wavelength of the wavevectors and n is an integer. While Bragg's law is useful for defining the basic scattering condition, in reality there are many scattering conditions that a lattice can satisfy. The relative intensities and positions of these scattering conditions allow us to calculate the structure of a sample.

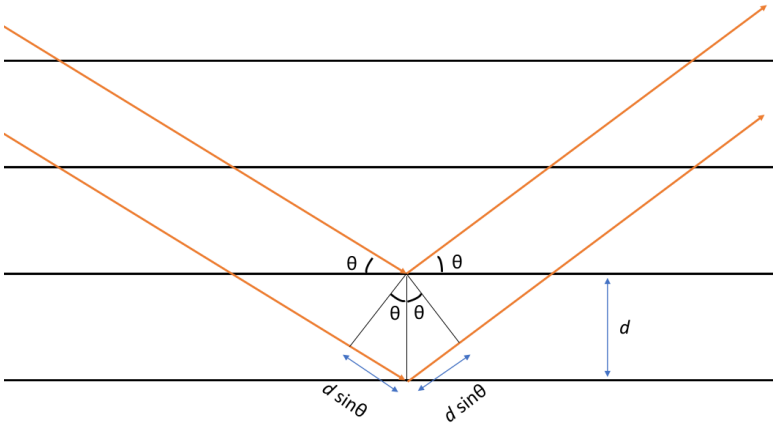

FIGURE 2.1: Visual depiction of Bragg's law. The emphasized distances of $dsin\theta$ where d is the interplane distance (blue) are the additional distance traveled by the second wave path (waves in orange). This additional distance gives rise to the factor of $2dsin\theta$ in equation 2.1. The Black lines represent periodic lattice planes.

From a predefined unit cell, with lattice vectors $\vec{a_1}, \vec{a_2}, \vec{a_3}$ (see [54] for a review of unit cells), a reciprocal lattice is defined:

$$\vec{b_1} = 2\pi \frac{\vec{a_2} \times \vec{a_3}}{\vec{a_1} \cdot \vec{a_2} \times \vec{a_3}} : \vec{b_2} = 2\pi \frac{\vec{a_3} \times \vec{a_1}}{\vec{a_1} \cdot \vec{a_2} \times \vec{a_3}} : \vec{b_3} = 2\pi \frac{\vec{a_1} \times \vec{a_2}}{\vec{a_1} \cdot \vec{a_2} \times \vec{a_3}} \tag{2.2}$$

A scattering vector $\Delta\vec{k}$ is defined from the incoming and outgoing wavevectors:

$$\Delta\vec{k} = \vec{k'} - \vec{k} \tag{2.3}$$

The fundamental scattering function, the structure factor is given by [53]:

$$F(\Delta\vec{k}, t) \propto e^{-i\omega t} \int_V \rho(r) e^{i\Delta\vec{k}\cdot\vec{r}} dV \tag{2.4}$$

where $e^{i\omega t}$ is an undetermined phase that results from the Fourier transform of the scattering density $\rho(r)$, and the volume V is the volume of the scattering sample.

Importantly, the scattering density $\rho(r)$ is dependant on the probe used and the scattering sample. The term $e^{i\vec{\Delta k}\cdot\vec{r}}$ gives the scattering direction and associated intensity of the outgoing waves, at a point $\vec{r}$ in the sample, that has a scattering density $\rho(r)$. This term is integrated over the entire sample volume. Thankfully, this simplifies significantly under a periodic lattice. The intensity of a scattered wave is given by $F(\vec{\Delta k}, t) \cdot F(\vec{\Delta k}, t^*)$ yielding [53]:

$$I(\vec{\Delta k}) \propto |\int_V \rho(r) e^{i\vec{\Delta k}\cdot\vec{r}} dV|^2 \tag{2.5}$$

To simplify to a periodic lattice we define a periodic scattering vector from $\vec{\Delta k}$:

$$\vec{G_{hkl}} = h \cdot \vec{b_1} + k \cdot \vec{b_2} + l \cdot \vec{b_3} \tag{2.6}$$

Where h,k,l are integers that give all of the whole number multiples of the reciprocal lattice vectors and $\vec{G}$ defines the reciprocal lattice and replaces $\vec{\Delta k}$ for crystalline systems. In a periodic system the term $e^{i\vec{\Delta k}\cdot\vec{r}}$ is zero when integrated over the volume except at periodic points in the lattice when $\vec{\Delta k} = \vec{G}$. This allows for a simplification of the integral form to the crystalline diffraction intensity given by:

$$I_{hkl} \propto |\sum^{N} f_N(\vec{G_{hkl}}) e^{i2\pi(\vec{G_{hkl}}\cdot\vec{r}_N)}|^2 \tag{2.7}$$

Which refers to the diffraction intensity for a diffraction peak (h,k,l). The term N refers to an atom N at position $\vec{r}_N$ within the unit cell and the function is summed over all atoms within the unit cell. The form factor $f_N(\vec{G_{khl}})$ is a scattering vector dependant intensity function that gives the scattering power of each species in the unit cell. If the scattering species does not act as a point scatterer, we define a form factor as the Fourier transform of the spatial scattering density $\rho(r)$:

$$f(\vec{\Delta k}) = \int_V \rho(r) e^{i\vec{\Delta k}\cdot\vec{r}} dV \tag{2.8}$$

Practically this is typically represented by an analytical approximation, as a series of weighted Gaussian decay functions [55]:

$$f(\Delta\vec{k}) = T(\vec{G}) \sum_i a_i e^{-b_i(|\Delta\vec{k}|^2)} + c \tag{2.9}$$

Where the parameters a_i, b_i and c are empirical constants of the scattering species. The term T($\vec{G}$) however is a sample and temperature dependant thermal factor that represents the broadening of the scattering distribution $\rho(r)$ due to the random displacement of the atoms from their idealized crystal positions ($\vec{r}_N$) either due to thermal vibration or quenched disorder. This thermal displacement term can be given as an anisotropic term if the atoms displace disproportionately in some direction or an isotropic term to simplify the expression [55].

$$T^{aniso}(\vec{G}) = e^{-(B_{11}h^2+B_{22}k^2+B_{33}l^2+2B_{12}hk+2B_{13}hl+2B_{23}kl)} \tag{2.10}$$

$$T^{iso}(\theta) = e^{-\frac{B^{iso}sin^2\theta}{\lambda^2}} \tag{2.11}$$

The terms B_{ij} for the anisotropic case or B^{iso} for the isotropic case are the thermal displacement parameters. Other notations use U, the mean-squared displacement instead of B with the relationship $U = B/8\pi^2$ [56].

There are multiple nomenclatures and units used to describe both $\Delta\vec{k}$ and $|\Delta\vec{k}|$ used here and in the literature. The relevant scattering terms used in this work are:

$$2\theta(^\circ)$$
$$|\vec{s}| = \frac{1}{d}\,(\text{Å}^{-1})$$
$$\vec{Q} = 2\pi\vec{s}\,(\text{Å}^{-1})$$
$$\vec{G} = (h,k,l) \text{ (reduced lattice units, r.l.u.)}$$

Briefly, 2θ is twice the scattering angle in Bragg's law, this value is typically collected directly in monochromatic wavelength experiments. The value 2θ is not normalized to different wavelengths so often s or 1/d are used. The variable Q, referred to as momentum transfer, is often used in inelastic related work and is equivalent to the magnitude of $\Delta\vec{k}$ in neutron scattering. The reduced lattice units $\vec{G}$ are often used in single crystal data to reduce Bragg peaks to their integer multiples.

2.2.2 X-ray Diffraction Experiments

X-ray diffraction experiments can be performed using powder and single crystals. The major difference between the two is that single crystal experiments give $\vec{G_{hkl}}$ by rotating through all of reciprocal space in ϕ, ω, θ (where ϕ and ω are the crystal's polar rotation coordinates), whereas powder only gives $|\vec{G_{hkl}}|$ over the diffraction angle (θ) dimension. This integration over two dimensions tends to convolute Bragg peaks, and often doesn't allow for a simple extraction of their intensities. It is however much easier to prepare a sample for powder diffraction. All x-ray data presented here will be powder measurements, from a laboratory setup.

A laboratory diffractometer typically uses a rotating anode tube with a particular metal anode (in this thesis a copper anode is used). Electrons accelerate from the cathode to the anode and displace electrons leading to characteristic relaxations, yielding sharp peaks of x-ray intensity over a roughly flat background of white x-rays. These intense peaks of characteristic radiation are used for monochromatic x-ray experiments. Monochromatic x-rays are achieved here through using a diffraction monochromator of the (311) face of a Ge crystal, tuned to the $K_{\alpha 1}$ emission of the copper anode (1.540560 Å) which for the experiments presented here also acts as a focusing aperture.

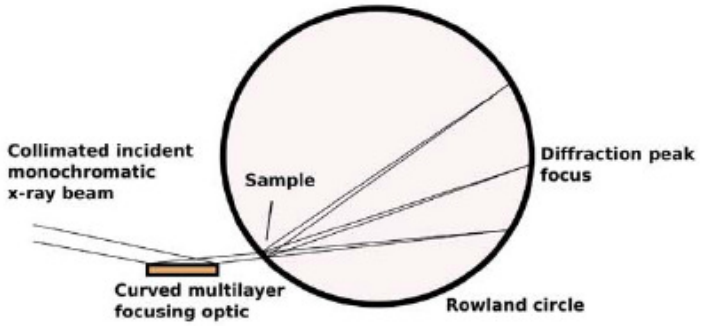

FIGURE 2.2: Depiction of an X-ray diffraction experiment in Guinier transmission geometry, the shaded circle represents the focusing circle where the detector imaging plate would be placed. This figure was reproduced from D. Siddons *et al.*, 2007 [57] with permission.

There are multiple geometries scattering experiments can use; in this thesis Guinier transmission geometry is used (Fig. 2.2) [57]. In this geometry, slits and collimators focus the x-ray beam to converge at the detector length without any

focusing slits after the sample. This geometry tends to provide very high resolution at low angles while allowing for a large detector bank as no slits are used after the beam interacts with the sample, improving experiment times [57]. This technique often results in highly asymmetric peaks compared to other geometries. The sample is mounted as thinly as possible on a flat film of amorphous mylar to reduce absorption. The detector used in this thesis is a Huber G670, with a fixed imaging film detector. A thermoluminescent film collects x-rays over an experimental run, and is read off by stimulation using a red laser resulting in blue luminescence (which is read off by a photomultiplier tube).

2.2.3 Rietveld Method

The Rietveld method of solving crystal structures is an optimization technique that takes a proposed unit cell and compares a calculated scattering pattern to the total experimental data pattern. The method of fitting raw experimental data will be discussed here. There are many programs used for pattern fitting, FullProf Suite [55] and GSASII [56] are used in this thesis. The general intensity of a powder pattern as calculated by FullProf for a proposed unit cell is given by [55]:

$$y_{calc,i} = \sum_{\phi} S_{\phi} \sum_{h} I_{\phi,h} \Omega(T_i - T_{\phi,h}) + b_i \tag{2.12}$$

The subscript i refers to a point in the diffraction pattern, often in 2θ, and $y_{calc,i}$ is determined for every point i in the data pattern that matches to experimental data. The subscript ϕ refers to a phase, as multiple distinct unit cells (phases) can be refined simultaneously in powder data consisting of multiple phases, and S is the scale of that phase. The subscript h refers to a Bragg peak. Only Bragg peaks near the point i (by some input margin) are used at any particular point. The Bragg intensity $I_{\phi,h}$ is the intensity of a Bragg peak given by the structure factor squared, and modified by several experimental factors; the Lorentz polarization factor (for X-rays), the absorption correction, and a preferred orientation function. The peak function Ω gives a real peak width to the point function $I_{\phi,h}$. There are multiple peak functions in use that are often specific to instrument configurations, which can include both instrumental peak resolutions as well as sample specific peak changes

due to factors like particle morphology or stress and strain peak broadening. For a detailed overview of the peak modeling in FullProf and GSASII see [55, 56].

These calculated values $y_{calc,i}$ are optimized against experimental points by a goodness of fit parameter:

$$\chi^2 = \sum_{i=1}^{n} w_i (y_{exp,i} - y_{calc,i})^2 \tag{2.13}$$

where χ^2 is the goodness of fit parameter, and w_i is a weighting parameter (that is $\frac{1}{\sigma_i^2}$ for a single pattern fit, where σ_i is the standard deviation error at point i). A set of variable parameters (α_k) are defined in order to minimize χ^2. Minimization of χ^2 is performed iteratively using the Gauss-Newton least squared refinement method in FullProf [55].

To compare the quality of fits between different refinements there are many different profile factors that can be used to define the fit quality, here the weighted profile factor R_{wp} is most commonly used [55]:

$$R_{wp} = 100\left(\frac{\sum_{i=1}^{n} w_i |y_{exp,i} - y_{calc,i}|^2}{\sum_{i=1}^{n} w_i y_{exp,i}^2}\right)^{\frac{1}{2}} \tag{2.14}$$

This weighted error function allows for comparison of the quality of different fits between different data sets, with the weight fraction is taken from the varience $w = \frac{1}{\sigma_i}$. As Rietveld refinement uses meaningful parameters related to the unit cell of the underlying crystal phases, we can use this least-squared regression to extract our crystal structures.

2.2.4 Neutron Diffraction Formalism

In addition to X-rays, neutrons are also used for diffraction. While X-rays are typically preferred for their higher flux and accessibility, trouble can arise in distinguishing between elements with similar electronic environments, or detecting small elements in the presence of large, electron dense elements. Neutrons provide a different contrast of atoms from X-rays based on their nuclear scattering intensity, instead of their electron count. Neutrons are also the go-to probe for magnetic structure determination, with well defined scattering amplitudes.

To achieve an appropriate wavelength near interatomic spacings, neutrons require kinetic energies on the order of meV, as opposed to photon energies in the range of keV. Due to the convenience of defining the neutron wavelength in different ways for different applications, multiple notations can be seen for the neutron energy [58].

$$E = \frac{81.81}{\lambda^2} = 2.072|\vec{k}|^2 = 5.227|\vec{v}|^2 = 0.08617T \tag{2.15}$$

This shows the relationship between the kinetic energy of the neutron (in meV) to the wavelength λ (in Å), the wavevector $\vec{k}$ (in $Å^{-1}$), the neutron velocity $\vec{v}$ (in km/s) and the neutron temperature scale (in Kelvin) given by $k_B T$. Neutrons from a reactor source are typically moderated to a specific temperature and produce a Maxwellian distribution of energies around that temperature. Conveniently, a neutron at 300 K will have an appropriate wavelength maximum for diffraction purposes at 1.78 Å, meaning that neutrons with a thermal distribution of energies are perfectly good to use for diffraction.

Whereas X-rays scatter off the electron density in solids, neutrons scatter off of the magnetic moments and nuclei of a sample. The nuclear scattering is defined by the scattering length b. However as b varies for different isotopes of an element and even for different nuclear spin states within a specific isotope, there are typically two components to the scattering, a coherent scattering cross section given by the mean value of b squared ($\langle b \rangle^2$) and incoherent scattering cross section, dictated by the variance of b. Elastic neutron nuclear scattering intensities for a point $\vec{r}$ are given by [58]:

$$\frac{d\sigma_{coh}}{d\Omega} = N \langle b \rangle^2 \sum_{\vec{r}} e^{i\vec{Q}\cdot\vec{r}} \tag{2.16}$$

$$\frac{d\sigma_{inc}}{d\Omega} = N(\langle b^2 \rangle - \langle b \rangle^2) \tag{2.17}$$

Where σ is the scattering cross section (coherent or incoherent) such that $\sigma_{coh} = 4\pi\langle b \rangle^2$, and Ω is the solid angle of scattering, which will be finite in real experiments, and N is the number of scattering species. This is generalized to include multiple species within a periodic unit cell such that the total diffraction equation gives [58]:

$$I_{hkl} = N\frac{(2\pi)^3}{V} T(\vec{G_{hkl}}) | \sum_N b_N e^{i\vec{G_{hkl}}\cdot\vec{r}_N} |^2 \tag{2.18}$$

for nuclear scattering where b in this case is defined as the coherent b, V is the volume of the unit cell. Conveniently there is no form factor in this expression, as the nuclei are point scatterers. However, the thermal displacement term T must still be considered. One result of this is that neutrons maintain a high peak intensity out to large values of (hkl) where X-rays fall off in intensity as a function of $|\vec{Q}|$.

The benefit of neutrons for nuclear crystallography is that they present a different contrast for each atom. Whereas an atom's X-ray scattering power scales with f_N which roughly scales with the number of electrons, an atom's neutron scattering power scales with b_N which does not increase monotonically with the element number, but varies wildly across the periodic table. This can in some cases allow for more accurate refinement of particular atomic positions and displacements compared to X-rays.

Neutrons also diffract off of the magnetic moments of unpaired electrons. The neutron-electron coupling constant is -0.27·10^{-27} cm. The complicating factor here is that unpolarized neutrons only diffract off of the component of the magnetization perpendicular to the scattering vector $\vec{Q}_\perp$. The structure factor of a reflection then is [59]:

$$F_M(G) = \sum_N e^{i\vec{G}_n \cdot \vec{r}_n} \vec{G}_n \times [\vec{M}_n(G) \times \vec{G}_n] T_n(G) \tag{2.19}$$

where $\vec{M}_n(G)$ is the vector form factor of the n^{th} ion in the unit cell, that includes both the magnetization vector and the magnetic form factor of the ion. As a magnetic structure is a collection of vectors, instead of a collection of point scatterers, it is useful to use symmetric representational analysis to interpret magnetic structures.

2.2.5 Magnetic Structure Refinement

First, we would like to relate the magnetic structure to its underlying crystal unit cell. A propagation vector **k** is defined as the periodicity of the magnetic structure to the unit cell. A propagation vector **k** = (0,0,0) maps directly on to the underlying unit cell and a propagation vector **k** = ($\frac{1}{2}$,0,0) would map onto two unit cells in the a_1 lattice and directly onto the unit cell in the other two directions. Programs such as SARAH [60] are able to generate a character representation or the permutation group of rank

3N of the unit cell with N magnetic ions, and decompose this representation into the irreducible representations of the space group [61].

$$\Gamma_{mag} = \sum_{v} n_v \Gamma_v \tag{2.20}$$

$$n_v = \frac{1}{n(G_k)} \sum_{g \in G_k} \chi\Gamma_{mag}(g) \times \chi\Gamma_v(g) \tag{2.21}$$

Where Γ_{mag} is the total representation, and Γ_v is a particular irreducible representation that is repeated n times in the total representation. Equation 2.21 shows the decomposition of the total representation into the irreducible representations that are invariant under the propagation vector $\mathbf{k}$, $\Gamma_v(g)$ where G_k is the group of operators that are invariant under the propagation vector $\mathbf{k}$, and χ is the character of the irreducible representation for that symmetry operator.

This decomposition yields a set of basis function ψ belonging to the symmetry permissible irreducible representations Γ. Magnetization on a particular site is defined by basis vectors, the symmetry translation, and the propagation vector translation by [61]:

$$\vec{m}_i = \sum_{v} C_v \vec{\psi_{i,v}} e^{-2\pi\vec{k}\cdot\vec{t}_i} \tag{2.22}$$

where $\vec{m}_i$ is the moment on the i^{th} atom in the unit cell, C_v is the fractional contribution of the v^{th} basis vector $\psi_{i,v}$ which is modulated by the propagation vector $\vec{k}$ and the translation of the i^{th} ion from the origin $\vec{t}_i$. Refinement software like FullProf Suite can use this symmetry representation to simplify the magnetic structure factor to [55]:

$$F_m(G_{hkl} + \mathbf{k}) = p \sum_{j} f_j(G_{hkl} + \mathbf{k}) S_{\mathbf{k},j} e^{2\pi i(G_{hkl}+\mathbf{k})r_j} \tag{2.23}$$

This is a summary of the structure factor used in FullProf Suite [55], where p is a normalization constant of 0.2695 μ_B, f_i is the form factor, and $S_{\mathbf{k},j}$ is the fourier component of the magnetization matrix, that is dependant on the irreducible representation components C_v and a refined phase ψ_k, that is only relevant for complex basis vectors.

2.2.6 Pair Distribution Functions

Pair distribution function (pdf) analysis is a method of analyzing total scattering data when Bragg scattering and crystal modeling is insufficient. In disordered crystalline materials that still contain Bragg peaks but also show short-range correlations or non-Gaussian distributions of local distortions that cannot be modeled by the thermal displacement factor T(G), the intensity between Bragg peaks can also be considered. To simplify this total scattering data a pair distribution function is defined by [62]:

$$G(r) = \frac{2}{\pi} \int_{Q_{min}}^{Q_{max}} Q(S(Q) - 1) sin(Qr) dQ \tag{2.24}$$

$$S(Q) = \frac{I^{coh}(Q) - \sum_i c_i \langle b \rangle_i^2}{\sum_i c_i \langle b \rangle_i^2} + 1 \tag{2.25}$$

where G(r) is the pair distribution function. G(r) is the Fourier transform of the reduced scattering intensity S(Q), which is normalized to the scattering intensity of the material. The cofactor c_i is the fractional atomic concentration of each species i in the material, and $\langle b \rangle^2$ is the coherent scattering power of that material.

The pair distribution function does not include any extra information from the total scattering I(Q), but it can allow for an easier visual interpretation of the data by viewing it as a real-space function in r (Å), and can allow for the fitting of data to be weighted more strongly towards short-range correlations, and the distribution of atoms over short-ranges. The intensity of the pair distribution is given by [63]:

$$G(r) = \sum_{m,n} c_m n_n b_m b_n \left(\frac{n_{mn}(r)}{4\pi r^2 \rho_m dr} - 1 \right) \tag{2.26}$$

where c_i are the the atomic fractions, n_{mn} is the number of atoms of type m at a distance [r,r+dr] from an atom n, which is normalized to the number of atoms m per unit volume ρ_m.

2.2.7 Polarized Neutron Diffraction

Polarized neutron analysis takes advantage of the differing cross section of interaction between neutrons in different polarizations and spin-states with different neutron interactions that can occur in order to deconvolute them. While it has a number of

applications, including the ability to distinguish between different ordered domains or chiralities that unpolarized scattering would see as identical, this work will focus on the isolation of magnetic scattering from nuclear scattering in order to simplify magnetic analysis.

A neutron that is initially polarized in an applied magnetic field in the z direction, will split into two states which will be referred to as + and -. A neutron interacting with a sample can undergo a spin flip, (+- or -+), or no spin flip (++ or - -). A review of the spin dependant scattering amplitudes are given in J.R. Stewart *et al.* [64], but the important results are:

$$\begin{aligned} \frac{d\sigma}{d\Omega} &= (\frac{m_n}{2\pi\hbar^2})^2 \langle U|U\rangle \\ U &= \langle k'S'|V(Q)|kS\rangle \\ U^{++} &= b_{coh} - pM_{\perp z} + b_{ii} + \frac{1}{3}b_{si} \\ U^{--} &= b_{coh} + pM_{\perp z} + b_{ii} + \frac{1}{3}b_{si} \\ U^{+-} &= -p(M_{\perp z} + iM_{\perp y}) + \frac{2}{3}b_{si} \\ U^{-+} &= -p(M_{\perp z} - iM_{\perp y}) + \frac{2}{3}b_{si} \end{aligned} \tag{2.27}$$

where U is the scattering amplitude, m_n is the mass of the neutron, $\hbar$ is Planck's constant, S is the spin state of the neutron (+ or -), k is the scattering vector, V(Q) is the interaction potential, b_{coh} is the coherent nuclear scattering length, b_{ii} is the incoherent scattering length due to the isotope distribution of the ions, b_{si} is the incoherent scattering length due to the nuclear spin distribution, p is the magnetic interaction length 0.2695 μ_B and $M_{\perp i}$ is the component of the magnetization perpendicular to Q in the i polarization direction. Of importance here is that none of the nuclear coherent scattering appears in the spin-flip measurements. In the single crystal experiments performed in this work a simple z-spin flip measurement is capable of isolating the $M_{\perp z} - iM_{\perp y}$ component of the magnetization (on top of a flat incoherent background).

One of the most powerful applications of polarized scattering is on powder samples with small, antiferromagnetic domains. The so called 'paramagnetic' approximation assumes no correlation between the x,y,z components of the magnetization, and

allows for xyz polarization decomposition. We define a two-dimensional scattering experiment with detector bank measuring Q over the range.

$$Q = [cos\alpha, sin\alpha, 0] \tag{2.28}$$

Where α is the in-plane scattering angle. Neutron polarization measurements are taken with incident polarizations along the x, y and z directions, yielding the polarization dependant scattering of a paramagnetic-like sample [64]:

$$\begin{aligned}
\frac{d\sigma}{d\Omega}^{nsf}_{x} &= \frac{1}{2}sin^2\alpha\frac{d\sigma}{d\Omega}_{mag} + \frac{1}{3}\frac{d\sigma}{d\Omega}_{si} + \frac{d\sigma}{d\Omega}_{nuc} \\
\frac{d\sigma}{d\Omega}^{sf}_{x} &= \frac{1}{2}(cos^2\alpha + 1)\frac{d\sigma}{d\Omega}_{mag} + \frac{2}{3}\frac{d\sigma}{d\Omega}_{si} \\
\frac{d\sigma}{d\Omega}^{nsf}_{y} &= \frac{1}{2}cos^2\alpha\frac{d\sigma}{d\Omega}_{mag} + \frac{1}{3}\frac{d\sigma}{d\Omega}_{si} + \frac{d\sigma}{d\Omega}_{nuc} \\
\frac{d\sigma}{d\Omega}^{sf}_{y} &= \frac{1}{2}(sin^2\alpha + 1)\frac{d\sigma}{d\Omega}_{mag} + \frac{2}{3}\frac{d\sigma}{d\Omega}_{si} \\
\frac{d\sigma}{d\Omega}^{nsf}_{z} &= \frac{1}{2}\frac{d\sigma}{d\Omega}_{mag} + \frac{1}{3}\frac{d\sigma}{d\Omega}_{si} + \frac{d\sigma}{d\Omega}_{nuc} \\
\frac{d\sigma}{d\Omega}^{sf}_{z} &= \frac{1}{2}\frac{d\sigma}{d\Omega}_{mag} + \frac{2}{3}\frac{d\sigma}{d\Omega}_{si}
\end{aligned} \tag{2.29}$$

where the superscript nsf refers to non-spin-flip, and sf, spin-flip. The subscripts refer to either the polarization direction, x, y, z or the scattering component, magnetic (mag), spin incoherent (si) or the nuclear coherent and isotope incoherent (nuc). It is important to know that if the sample is ferromagnetic with meaningfully sized domains, this approximation won't work due to depolarization of the beam, and even in long-range ordered antiferromagnets this can break down due to the isotropic magnetization assumption breaking down. If this does hold, a linear combination of these experimentally measured cross sections can be taken to yield [64]:

$$\begin{aligned}
\frac{d\sigma}{d\Omega}_{mag} &= 2\frac{d\sigma}{d\Omega}^{x}_{sf} + 2\frac{d\sigma}{d\Omega}^{y}_{sf} - 4\frac{d\sigma}{d\Omega}^{z}_{sf} \\
\frac{d\sigma}{d\Omega}_{mag} &= 4\frac{d\sigma}{d\Omega}^{z}_{nsf} - 2\frac{d\sigma}{d\Omega}^{z}_{nsf}\frac{d\sigma}{d\Omega}^{y}_{nsf} \\
\frac{d\sigma}{d\Omega}_{nuc} &= \frac{1}{6}(2\frac{d\sigma}{d\Omega}_{Tnsf} - \frac{d\sigma}{d\Omega}_{Tsf}) \\
\frac{d\sigma}{d\Omega}_{si} &= \frac{1}{2}\frac{d\sigma}{d\Omega}_{Tsf} - \frac{d\sigma}{d\Omega}_{mag}
\end{aligned} \tag{2.30}$$

where the subscripts Tsf, and Tnsf refer to the total spin-flip and non-spin-flip respectively. This decomposition of the experimental data to isolate the magnetic scattering can be incredibly useful, especially when trying to fit magnetic diffuse scattering in liquid-like magnetic systems, as diffuse scattering is difficult to fully isolate in traditional powder measurements.

2.2.8 Neutron Diffraction Experiments

Neutron diffraction experiments utilize neutrons from one of two sources. A fission reactor source which produces neutrons as a results of the fission of ^{235}U and the decay of its daughter products. Fission reactors used for neutron production in scattering are surrounded by a room temperature moderator (typically water), producing 'thermal' neutrons with a Maxwellian distribution [58]:

$$P(\lambda) \propto \frac{1}{\lambda^3} e^{-\frac{h}{2k_B T m \lambda^2}} \tag{2.31}$$

where P is the probability distribution, h is Planck's constant and m is the neutron mass. The thermal distribution gives a useable intensity of neutrons in a rough wavelength range of 0.5-4 Å. For some applications, additional moderators are used to modify this distribution with hot or cold moderators. Importantly, fission reactors are a continuous source of neutrons. Spallation sources of neutrons use linear proton accelerators to generate high energy protons, which are typically pulsed on a heavy nuclei target. This releases a short burst of neutrons, over roughly 1 μs. The distribution of neutrons from this source follows a near Maxwellian distribution at long wavelengths, but there is a much greater number of neutrons at short wavelength or

high energies. This distribution of 'hot' or 'epithermal' neutrons is often left unmoderated for certain applications. In diffraction these 'hot' neutrons provide better access to high Q data which are useful in total scattering experiments. The pulses of a spallation source are typically in the range of 10-100 Hz, which allows for time-of-flight measurements to be used instead of traditional diffraction measurements.

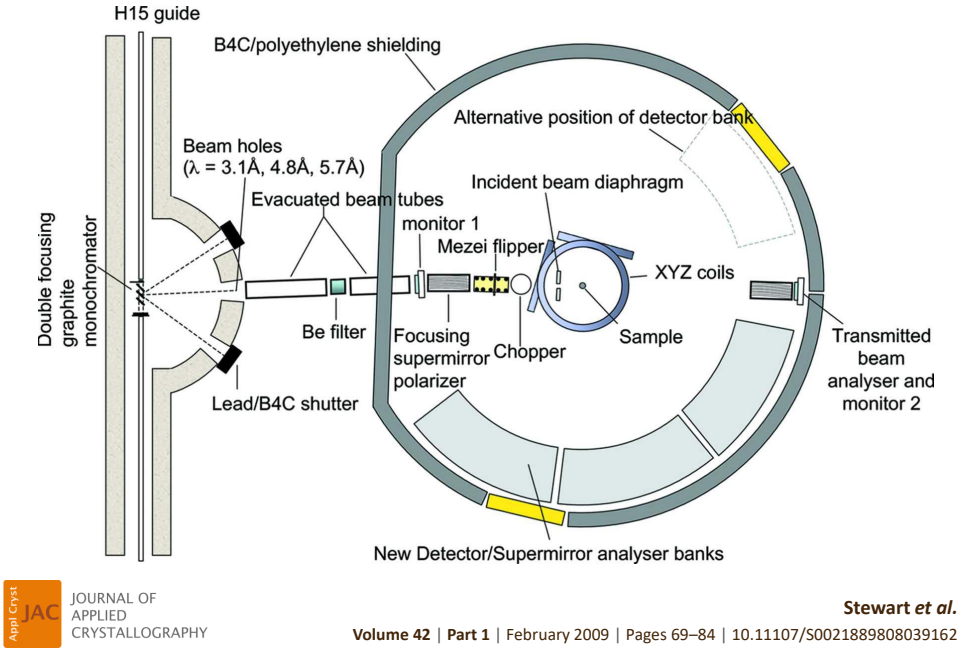

FIGURE 2.3: This is a figure of the D7 diffractometer at the ILL, reproduced from J.R. Stewart *et al.*, 2009 [64], in compliance with the relevant publication policy. This diffractometer is a diffuse scattering polarized diffractometer, but also acts as the rough layout for a generic constant wavelength diffractometer, with the exception of the chopper and polarization optics.

The typical neutron diffraction experiment looks something like Figure 2.3, a schematic of the D7 polarized diffractometer. Ignoring the chopper and polarization optics, the typical single wavelength diffractometer monochromates the beam with a crystal monochromator (often graphite), and the incident wavelength can be altered by rotating the monochromator and the sample position. An angle dependant detector array surrounds the sample, typically constructed of ^{3}He charge capture tubes, that capture neutrons and create ionized products, which can be observed electronically. The Figure 2.3 also shows the added complexity of neutron polarization analysis for

the xyz decomposition described in equation 2.30. A supermirror is a heterostructure of ferromagnetic and non-magnetic layers, that increases the critical scattering angle of correctly polarized neutrons, and allows incorrectly polarized neutrons to pass through, bending a beam of highly polarized neutrons with a polarization fraction > 99%. Mezi flippers and xyz coils are wire coils used to generate a magnetic field to cause a neutron to precess into the desired polarization direction.

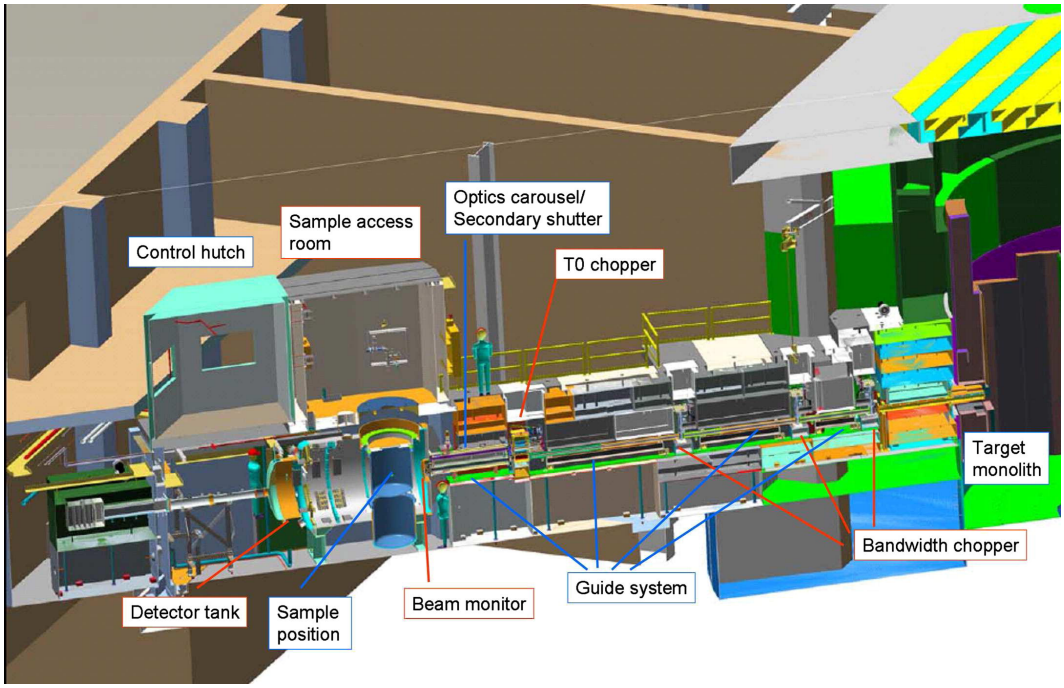

FIGURE 2.4: This is a figure of the NOMAD total scattering diffractometer at the ORNL, reproduced from J. Neuefeind *et al.*, 2012 [65], with relevant permissions. This instrument is a wide wavelength time-of-flight diffractometer, used for diffraction and total scattering measurements.

Although monochromation of the neutrons is required for continuous sources, pulsed sources are able to take advantage of a range of neutron wavelengths simultaneously, often increasing the neutron flux on sample dramatically. Figure 2.4 shows the setup of the Nanoscale Ordered MAterials Diffractometer instrument (NOMAD) at the Oak Ridge National Laboratory, a time of flight diffractometer, commonly used for total scattering studies.

As the wavelength of a neutron is related to its velocity (eq. 2.15) and the velocity is reasonable to measure on a macroscopic time scale ($\sim 10^1$ km/s), the wavelength of a neutron can be determined based on the time it takes to reach a detector as long as the start of a pulse is well defined. Figure 2.4 shows the series of choppers leading

up to the sample, used to define the incoming pulse (the T0 chopper) and define an lower and upper wavelength used for the experiment, in order to prevent frame overlap between multiple pulses. The detector bank here is in a series of roughly constant angle ring detectors around the sample whose angles are renormalized such that the final data can be seen as a function of each constant-angle detector ring. Due to the instrument design, data are often shown with intensity as a function of neutron arrival time at a fixed angle as opposed to the conventional intensity as a function of angle.

2.2.9 Reverse Monte Carlo Analysis

Reverse Monte Carlo (RMC) analysis is a 'big box' method of modeling disordered materials from total scattering data. A box of NxNxN unit cells of an idealized structure are used to model a scattering pattern from a pair correlation calculation of the scattering intensity. The species in this box are randomly perturbed to improve the fit to the experimental data, using the goodness of fit χ^2 as an indicator. Perturbations that improve the fit ($\Delta\chi^2 < 0$) are accepted and further improved upon, whereas fits that worsen ($\Delta\chi^2 > 0$) the fit are accepted with a probability, $\propto e^{(-\Delta\chi^2)}$, in order to allow the fit to escape from false minima in the fitting routine.

The intensity of nuclear neutron scattering from a 'big box' model for a powder sample can be calculated by [63]:

$$I(Q) = \frac{1}{N}\sum_{i,j} b_i b_j \frac{sin(Q|r_{ij}|)}{Q|r_{ij}|} \tag{2.32}$$

Where N is the number of atoms, i, j are indices for all of the atoms in the model, and r_{ij} is the distance between atoms i and j. This becomes more complicated in magnetic systems where the scattering is dependant on the spin vectors, J. Paddison *et al.* give a powder simplified version [66, 67]:

$$I(Q) \propto f(Q)^2 \left[\frac{2}{3} + \frac{1}{N}\sum_{i,j}\left(A_{ij}\frac{sin(Q|r_{ij}|)}{Q|r_{ij}|} + B_{ij}\left(\frac{sin(Q|r_{ij}|)}{(Q|r_{ij}|)^3} - \frac{sin(Q|r_{ij}|)}{(Q|r_{ij}|)^2}\right)\right)\right] \tag{2.33}$$

$$A_{ij} = S_i \cdot S_j - (S_i \cdot \hat{r}_{ij})(S_j \cdot \hat{r}_{ij})$$
$$B_{ij} = 3(S_i \cdot \hat{r}_{ij})(S_j \cdot \hat{r}_{ij}) - S_i \cdot S_j$$

While there are programs that are capable of performing RMC analysis, such as RMCProfile and spinvert [63, 66], one of the more difficult aspects is interpreting the results. Fundamentally the resulting fit from RMC is an overfit pattern to a model in a false minimum, due to the large number of parameters used to develop the fit. This is still reasonable as fitting a disordered structure inherently implies that the system is in a false minimum as well. To further verify that the fit is representative of the underlying system, the RMC fit is usually repeated multiple times with varying (or entirely random) starting configurations, to show a consistent result. To interpret the results, the large derived structures need to be reduced to a meaningful average. However, this is often system dependant as to what values are most important. Commonly in magnetic systems the correlation function $\langle S_i \cdot S_j \rangle$ is given as a function of r_{ij} in order to determine correlation lengths, although more details can often be extracted on a system dependant basis. Additionally, RMC systematically underestimates most correlation values, due the randomly accepted, 'bad moves' allowed within the fit. Despite the somewhat limited conclusions that can be drawn from RMC analysis, it is a powerful tool that is capable of fitting disordered systems without making initial assumptions about the system that might give biased results.

2.3 Neutron Spectroscopy

2.3.1 Time-of-Flight Spectroscopy

There are two common ways of performing neutron spectroscopy: the triple axis method and the time of flight method. These methods are effectively the same as the diffraction methods for constant wavelength and time of flight, with an additional energy selection process included. In triple axis experiments, a constant wavelength diffraction setup has a second monochromator added after the sample to select a final wavelength, giving E_f alongside E_i for energy resolution. This is a cumbersome method if a large range of (Q,E) space is to be investigated, making time of flight methods better. Time-of-flight methods use a series of choppers not just to define a

broad-band pulse like in diffraction time-of-flight, but to monochromate the beam as well. This allows E_f to be calculated based on the sample to detector travel time. This method allows for the simultaneous collection of E_f values for a single E_i.

2.3.2 Rare Earth Crystal Electric Fields

The common discussion of crystal fields is typically restricted to the strong field or intermediate field cases common in transition metals. In the strong field case the crystal electric field (CEF) energy is greater than the Pauli repulsion, causing spin pairing dictated by the crystal field. The intermediate field case has a CEF energy weaker than the Pauli repulsion, so the crystal field only changes the symmetry and multiplicity of the spins but still causes the quenching of spin-orbit coupling. In the weak field case, relevant here, the CEF energy is weaker than the spin-orbit coupling, such that the crystal field is a perturbation of the Hund's rule J: J = |L-S| for less than half filled shells and J = |L+S| for greater than half filled shells. In the weak field case the CEF splits the ground state J multiplet into m_j states, although small contributions from other J states can contribute, these multiplets are typically labeled as $^{2S+1}L_J$.

In the weak field and intermediate field case the crystal electric field splitting in rare earths can be treated by the Hamiltonian [68]:

$$H_{CEF} = \sum_{k=0}^{2L} \sum_{q=-k}^{k} B_q^k C_k^q(\theta, \phi) \tag{2.34}$$

$$C_q^k(\theta, \phi) = \sqrt{\frac{4\pi}{2k+1}} Y_{k,q}(\theta, \phi) \tag{2.35}$$

Where B_q^k are the variable crystal field parameters, called the Wybourne parameters and C_q^k are the Wybourne tensor operators which are a function of the spherical harmonics $Y_{k,q}(\theta, \phi)$. The quantization numbers k and q span from k = (0,2l) or (0,2J) whichever is smaller, and q = (-k,k) with l = 3 for rare earth systems. One of the reasons this method is used is due to the symmetry reduction of the crystal field parameters B_q^k that can be performed, with as few as 2 parameters for a cubic system [69]. Six crystal field parameters are required to describe a hexagonal symmetry

including D_{3d} and D_3 which are relevant to this work. This Wybourne formalism is related to the Stevens' formalism which is often used for determining the underlying eigenvectors, although the notation can become confusing. The Stevens' operators are given by [70]:

$$H_{CEF} = \sum_{k=0}^{2L} \sum_{q=-k}^{k} B_k^q O_q^k(J_x, J_y, J_z) \tag{2.36}$$

Note here that B_k^q and B_q^k are not equivalent but related by $B_k^q = \lambda_{kq}\theta_k B_q^k$. The Stevens' operators $O_q^k(J_x, J_y, J_z)$ are a function of the orbital operators allowing the eigenvectors $\langle m_J \rangle$ to be determined, more simply. The values for λ, θ as well as the Stevens' operators and the details of these calculations are found throughout several works [58, 68–71].

Once the eigenvectors $\Gamma = \{c_1 m_{-J} : c_n m_J\}$ have been determined the inelastic neutron cross section is given by [58]:

$$\frac{d^2\sigma}{d\Omega d\omega} \propto \frac{k'}{k} f^2(Q) |\langle \Gamma_m | \hat{J}_\perp | \Gamma_n \rangle|^2 \times \delta(\hbar\omega + \Delta E) \tag{2.37}$$

$$|\langle \Gamma_m | \hat{J}_\perp | \Gamma_n \rangle|^2 = \frac{2}{3} \sum_{xyz} |\langle \Gamma_m | \hat{J}_{xyz} | \Gamma_n \rangle|^2 \tag{2.38}$$

That is, there are dispersionless (Q,E independent) excitations at the eigenvalues given by $\delta(\hbar\omega + \Delta E)$ that have a Q dependant intensity given by the form factor squared, with a transition intensity given by the operator matrices of each state (these values are tabulated in [70]). Programs like SPECTRE [68] and McPhase [71] are able to perform rare earth crystal field calculations including least-squared regression fits to inelastic neutron scattering energies and intensities.

2.3.3 Magnetic Excitations

A discussion of measuring magnetic excitation with neutron will be limited here, as methods tend to be quite application dependant, and the work here largely relies on comparison to previously published work. In general, the neutron scattering relationship for magnetic excitations is given by the dynamic correlation function [72] :

$$S(k,\omega) = \frac{1}{2\pi N}\sum_{i,j} e^{ik(r_i - r_n)} \int_{-\infty}^{\infty} e^{i\omega t} \left\langle S_i S_J^T(\tau)\right\rangle d\tau \tag{2.39}$$

Where τ represents (x,y,z), and $\left\langle S_i S_j^T(\tau)\right\rangle$ is the expected product of the spin states i,j at an excitation energy ω. Semi-classical methods like linear spin wave theory [72] are able to model the magnetic excitations of an ordered system (magnons). For disordered systems on the other hand the excitation can be broad in nature and can't be easily explained by linear spin wave theory. In these cases the dynamic susceptibility, obtained from a model can be used with [58]:

$$S(Q,\omega) \propto (1 - e^{\frac{\hbar\omega}{k_B T}})^{-1}\chi''(Q,\omega) \tag{2.40}$$

In fact the dynamic susceptibility (χ'') is a commonly reported value for neutron intensity and is related to the cross section as $\frac{d^2\sigma}{d\Omega d\omega} = (1 - e^{-E/k_B T})^{-1}\frac{k}{k'}\chi''(Q,\omega)$.

Relevant to this work is a method of normalizing magnetic excitations to the incoherent background, by integrating energy over a constant Q-range, away from any Bragg scattering, that allows for a determination of the dynamic magnetization. [73]:

$$\begin{aligned} M(Q,\omega) &= \frac{13.77(b^{-1})\mu_B^2 I(Q,E)}{|f(Q)|^2 N k_f R_0} \\ N k_f R_0 &= 4\pi \frac{\int I(Q,E)dE}{\sum_i \sigma_i^{inc}} \end{aligned} \tag{2.41}$$

The magnetization per site over the integrated energy range M(Q,ω) can be normalized to the intensity of the excitation $\int I(Q,E)dE$ and the incoherent scattering of the sample $\sum_i \sigma_i^{inc}$. Although this is assumed to be for a constant k_f scan on a triple axis, it can be applied to a constant E_i scan such as on a time-of-flight instrument, correcting for k_f.

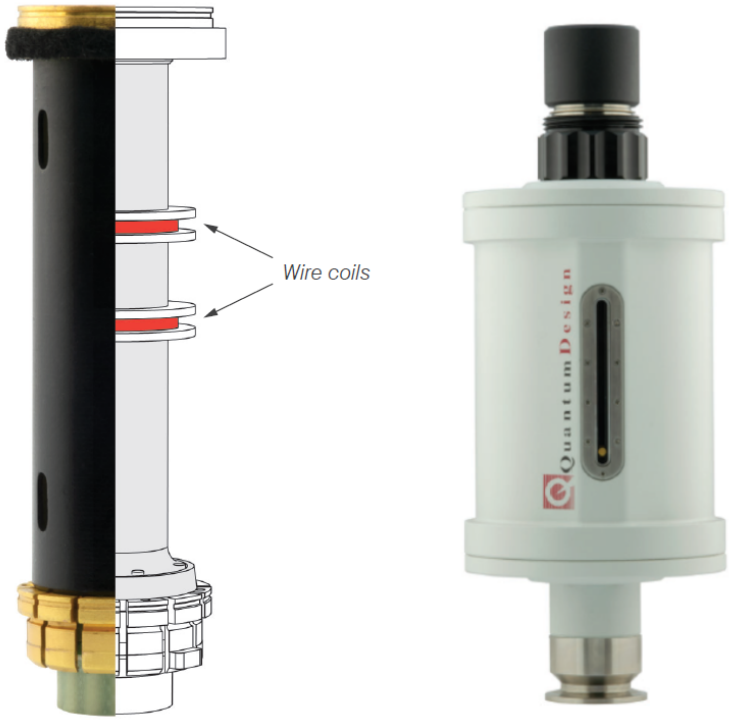

FIGURE 2.5: This figure shows a schematic for the Vibrating Sample Magnetometer (VSM) module for a Quantum Design Physical Property Measurement System. (left) The sample pickup coil, that detects the magnetization from the vibrating sample within. (right) The linear transport motor, that oscilates the sample in the pickup coil. This figure was modified from the Quantum Design Physical Property System, Vibrating Sample Magnetometer promotional material [74].

2.4 Magnetometry

2.4.1 VSM Experimental Setup

In this thesis a vibrating sample magnetometer (VSM) is commonly employed. The VSM (Fig. 2.5) places a sample in a DC magnetic field H, and the sample vibrates in the direction of the field $\hat{z}$ with an amplitude A, and a frequency f, typically 3 mm and 40 Hz respectively. The vibration takes place inside of a pickup wire coil generating an oscillating voltage given by:

$$\begin{aligned} V_{coil} &= \frac{d\Phi}{dt} = \frac{d\Phi}{dz}\frac{dz}{dt} \\ V_{coil}(t) &= 2\pi f C m A sin(2\pi f t) \end{aligned} \tag{2.42}$$

where Φ is the magnetic flux, z is the vertical position of the sample in the pickup

coil, C is a calibrated coupling constant, m is the sample magnetization, A is the vertical amplitude of oscillation, f is the frequency of oscillation. The Quantum Design VSM used here is capable of detecting magnetization of $\sim 10^{-6}$ (emu), with a measurement frequency of ~ 1 (s). Both the magnetization (m) and the susceptibility $\chi = \frac{m}{H}$ are used in this work.

2.4.2 Direct Current Magnetometry

DC magnetometry can be used to probe for magnetic phase transitions as a function of field and temperature. It can be used to determine the saturation moment of a system, by normalizing the magnetization per ion. Commonly the Curie-Weiss law is used to analyze the temperature dependant magnetization of a paramagnetic phase.

$$\chi = \frac{C}{T - \theta_{CW}} \tag{2.43}$$

$$C = \frac{\mu_0 N}{3k_B} g^2 J(J+1)\mu_B^2 \tag{2.44}$$

$$\mu(\mu_B) \approx 2.84\sqrt{C(\frac{emu \cdot K}{Oe \cdot mol})} \tag{2.45}$$

Fitting the susceptibility χ yields θ_{CW} the Curie-Weiss temperature, which is an indication of the net spin interactions in the paramagnetic phase, and in a non-frustrated system should be roughly the ordering temperature. The Curie constant C, is related to the paramagnetic moment $\mu = g\sqrt{J(J+1)}$ where g is the Landé coupling factor.

However, the Curie-Weiss law is only relevant for a paramagnet where the only relevant energy splitting over the temperature range is the Zeeman splitting. If excited crystal field states become populated at higher temperatures the Van Vleck susceptibility has to be used, which can be related to the previously mentioned crystal field scheme by [27, 68]:

$$\vec{\chi}_\tau = \frac{N_A g^2 \mu_B^2}{Z} \sum_\tau \left(\sum_{n,E_n=E_m} \frac{|\langle \Gamma_n|\mu_\tau|\Gamma_m\rangle|^2 e^{-\frac{E_m}{k_B T}}}{k_B T} + 2 \sum_{n,E_n \neq E_m} \frac{|\langle \Gamma_n|\mu_\tau|\Gamma_m\rangle|^2 (e^{-E_n/T} - e^{-E_m/T})}{E_n - E_m} \right)$$
$$Z = \sum_n e^{E_n/k_B T} \tag{2.46}$$

Where Z is the partition function and Γ_n is the n^{th} crystal field. This can be used to relate the susceptibility to the crystal field schemes fit by inelastic neutron scattering.

2.5 Specific Heat

The specific heat of a material is used here to identify phase transitions, and as a direct measure of the thermodynamic properties of a material. The constant-pressure heat capacity is given by:

$$C_p = \left(\frac{dq}{dT}\right)_p \tag{2.47}$$

where q is heat. Assuming $C_p = C_v$ gives $C(T) = \frac{dU(T)}{dT}$, which is a reasonable assumption for solid systems with minimal thermal expansion in a vacuum. If the measurement is of an equilibrium process the specific heat can be related to the change in entropy by:

$$\Delta S = \int_{T_1}^{T_2} \frac{C(T)}{T} dT \tag{2.48}$$

If a magnetic transition can be isolated, the entropy can be used to measure the extent of ordering. A fully ordered system with a spin state degeneracy ω will have an entropy of $k_B ln(\omega^N)$ where N is the number of magnetic ions.

2.5.1 Quasi-Adiabatic Method

Specific heat measurements in this work have been performed by the quasi-adiabatic method. This method measures the specific heat by applying a small heat pulse with a resistive heater, heating the sample in the range of 0.1-2% of the initial temperature T_i (for low temperature measurements). The sample sits on a small platform that is

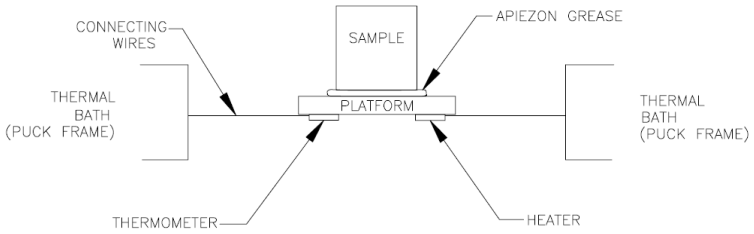

FIGURE 2.6: This figure shows a schematic for an adiabatic heat capactiy measurement. For scale, the sample platform used in this thesis is roughly 5 mm across. The thermal bath here is regulated by the Quantum Design Physical Property measurement system (PPMS) cryostat, or Helium-3 cryostat. This figure was modefied from the Quantum Design Physical Property System heat capacity option user manual [75].

largely thermally isolated in a vacuum, and connected to a thermal bath by thin wires (Fig. 2.6). There is still some heat loss during this process, so the relaxation back to T_i after the thermal excitation is measured giving [75]:

$$\begin{aligned} C\frac{dT}{dt} &= -K_w(T - T_i) + P(t) \\ P(t) = 0: \qquad T(t) &= (T_{max} - T_i)e^{\frac{-Ct}{K_w}} + T_i \end{aligned} \tag{2.49}$$

where K_w is the thermal conductivity of the wire, and P(t) is the power application which is constant during the heat pulse and zero during the relaxation period. If K_w is accurately calibrated, the specific heat can be extracted from the relaxation. This model assumes good thermal contact between the sample platform and the sample, which are usually connected by thermally conductive grease. If there is poor thermal contact, a two exponential function is used that treats the sample and sample platform independently. This method contains a minimal setup with just a resistive heater and thermocouple connected to a thermal bath that is convenient for low temperature measurements. The quasi-adiabatic method can also provide good temperature resolution if the thermal excitation is reduced.

Chapter 3

Structure of the Ln_2ScNbO_7 Charge Disordered Pyrochlores

3.1 Introduction

Synthesis of the Ln_2ScNbO_7 pyrochlores was first reported by Zouari *et al.* in 2008 [46], for the lanthanides Ln = Pr, Nd, Eu, Gd, Dy. In 2010 the same group also reported another set of charge disordered rare earth pyrochlores, the Ln_2BSbO_7 (B = Sc, Ga, In) pyrochlores [47]. These pyrochlores contain a lanthanide (III) on the A-site and a disordered mix of III, V valence ions on the B-site, averaging out to the typical IV valence found in the conventional $Ln_2^{+3}B_2^{+4}O_7$ pyrochlores. Similarly there are multiple series of A-site charge disordered fluoride pyrochlores that allow for B^{+2} transition metals to lie on the B-site such as the $NaSrB_2F_7$ (B = Mn, Fe) pyrochlores [44].

Here, additional members of the Ln_2ScNbO_7 family are presented (Ln = La, Sm, Tb) and reported, and the growth of large single crystals is discussed. The crystal structures are refined and the short-range correlations that form due to charge disorder are investigated through the pair distribution function (PDF) technique.

All of the work in this chapter was performed by the author with the exception of; data collection and reduction of NOMAD data, which was done through a mail-in program with the aid of Jue Liu (ORNL), and some crystal growths which were performed as an exercise for undergraduate students Nathan Hiebert, Megan Rutherford, and Kelsey Duncan, supervised by the author. Some of the data in this section have been reproduced from C. Mauws *et al.*, 2021 [76].

3.2 Preparation

Powder samples of the Ln_2ScNbO_7 pyrochlores, Ln = La, Pr, Nd, Sm, Gd, Tb, Dy were prepared by conventional solid state synthesis. Powder reagents (Alfa Aesar Ln_2O_3 = 99.99%, Sc_2O_3 = 99.9%, and Nb_2O_5 = 99.999% purity, metals basis) were mixed and ground in mortar and pestle in stoichiometric ratios following;

$$Ln_2O_3 + \frac{1}{2}Sc_2O_3 + \frac{1}{2}Nb_2O_5 \rightarrow Ln_2ScNbO_7 \ (Ln = La, Nd, Sm, Gd, Dy) \tag{3.1}$$

$$\frac{1}{3}Pr_6O_{11} + \frac{1}{2}Sc_2O_3 + \frac{1}{2}Nb_2O_5 \rightarrow Pr_2ScNbO_7 + \frac{1}{3}O_2 \tag{3.2}$$

$$\frac{1}{2}Tb_4O_7 + \frac{1}{2}Sc_2O_3 + \frac{1}{2}Nb_2O_5 \rightarrow Tb_2ScNbO_7 + \frac{1}{4}O_2 \tag{3.3}$$

Samples were pressed into ampoules under 30 MPa of pressure and fired in alumina crucibles at 1400 °C in 16 hour intervals under air with intermediate regrindings until phase pure (except for La_2ScNbO_7 which was heated at 1450 °C). The smaller lanthanide cation species were typically phase pure after one firing interval (Ln = Gd, Tb, Dy). The larger cations required additional firings increasing with cation size up to La_2ScNbO_7 for which phase purity was never achieved, and an impurity that indexed to $LaNbO_4$ remained at roughly 5% ($\frac{wt.}{wt.}$), varying by sample. As the sample itself refined consistently to the pyrochlore structure and was consistent with the unit cell trend for other members of the series, this impurity was likely $LaNb_{1-x}Sc_xO_{4-x}$ where x remains undetermined.

Single crystal samples were prepared by the optical floating zone method using a Quantum Design 2-Mirror IR Image Furnace. The samples (Ln = Nd, Sm, Gd, Dy) were grown under flowing air, and the samples (Ln = Pr, Tb) were grown under flowing Ar. All samples were grown at a rate of 1 $\frac{cm}{hour}$ with the feed and seed rods counter rotating at 15 rpm each. Despite being grown under Ar, the Ln = Pr, Tb samples showed slight black discoloration from their expected green and light brown respectively, likely due to the presence of a small amount of Ln^{+4} instead of the desired Ln^{+3}. Annealing the crystals under flowing 2% H_2 in Ar at 600 °C for 6 h was sufficient to achieve the desired colours indicating a pure Ln^{+3} valence. No change in unit cell size was observed through this reduction suggesting that the discolored crystals have a negligible concentration of Ln^{+4}. While most crystals could

be grown to an arbitrarily long length, the small cation Ln = Tb, Dy samples shattered while the crystals were < 1 cm in length possibly due to a high temperature phase transition. While this limited the size of available crystals (< 500 mg), they remained phase pure. The only species that couldn't be grown phase pure in any amount was La_2ScNbO_7. As a white powder it is likely that the light absorption was very low, evidenced by an instrumentally limited applied voltage (95 V) to the lamps during growth. Near maximum intensity the image furnace struggled to melt La_2ScNbO_7 leaving an unstable melt. It is likely that a higher power floating zone furnace could be used to grow this sample.

3.3 Crystallography of the Ln_2ScNbO_7 pyrochlores

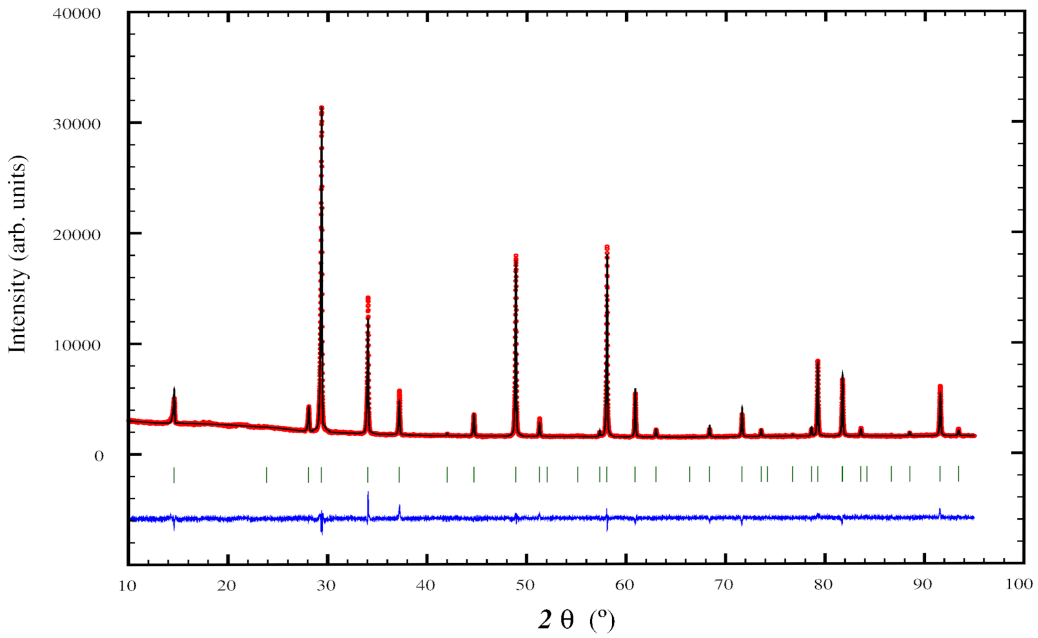

FIGURE 3.1: Refined X-ray diffraction pattern for Nd_2ScNbO_7, shown as a representation for the Ln_2ScNbO_7 systems. Red points represent the observed data, the black line is the calculated pattern from the refined structure, the blue line is the difference between the calculated and observed patterns, and the green dashes represent calculated Bragg peak positions.

X-ray powder diffraction (PXRD) was used to establish the phase purity of powder and ground single crystal samples. A Huber laboratory powder x-ray diffractometer was utalized in Guinier geometry with a Cu X-ray source, monochromated to Cu $\mathbf{K}_{\alpha 1}$ using a Ge (311) monochromator. Samples were ground and mounted on Mylar film.

The FullProf Rietveld refinement suite [55] was used to refine the PXRD structures, with results reported in table 3.1. Figure 3.1 shows a sample PXRD refinement of Nd_2ScNbO_7, which is consistent with the results of most samples. Figure 3.2 shows the exception of La_2ScNbO_7 where an impurity that indexes to the $I4_1/a$ $LaNbO_4$ phase [77] which is also refined, along with another smaller impurity that could not be indexed. This $LaNbO_4$ like impurity is observed in the initial heating stages of the other large cation members of the Ln_2ScNbO_7 series, but normally disappears after sufficient heatings, or after crystal growth in the image furnace. This allowed for phase pure preparation of all other phases. Refinement of this impurity yields a mass fraction of 3.01(1) % in the given diffraction patterns. However, the size of the impurity changed between samples. As previously stated, this impurity appears to be $La_2Nb_{1-x}Sc_xO_{4-x}$ as the unit cell volume of 353 $Å^3$ is larger than the reported value of 341 $Å^3$, and refinement of x yielded a value of 0.2(1). However, both the unit cell lengths and the value of x should be considered unreliable due to difficulty of refining such a small component. If the x-value is taken meaningfully, the remaining unindexed impurity likely contains some of the excess scandium, but it does not index to Sc_2O_3.

TABLE 3.1: X-ray diffraction results. The high symmetry position of O_{8b} does not allow for off diagonal anisotropic terms. Reports of O_{48f} were simplified with the largest in diagonal and off diagonal components shown, as the lower symmetry site allows many anisotropic terms.

Ln	a (Å)	Ln B_{iso} ($Å^2$)	Sc/Nb B_{iso} ($Å^2$)	R_{wp}
La	10.6486(2)	1.79(3)	1.24(4)	15.0
Pr	10.5585(2)	0.84(2)	1.25(3)	11.2
Nd	10.5298(2)	1.18(2)	1.38(4)	11.9
Sm	10.4618(3)	1.78(4)	1.20(5)	15.4
Gd	10.4270(4)	1.84(5)	0.73(6)	17.0
Tb	10.3763(4)	2.52(4)	1.14(5)	16.0
Dy	10.3439(3)	3.02(4)	1.16(4)	12.1

Neutron Powder diffraction (NPD) was also obtained in tandem with neutron pair distribution function (NPDF) measurements from the NOMAD time of flight (TOF) diffractometer at the Oak Ridge National Laboratory (ORNL) [65]. Powder samples of Ln = La, Pr, Nd, Tb, Dy were mounted in amorphous quartz capillaries in measured quantities of roughly 150 mg. Data were taken at 290 K using the typical

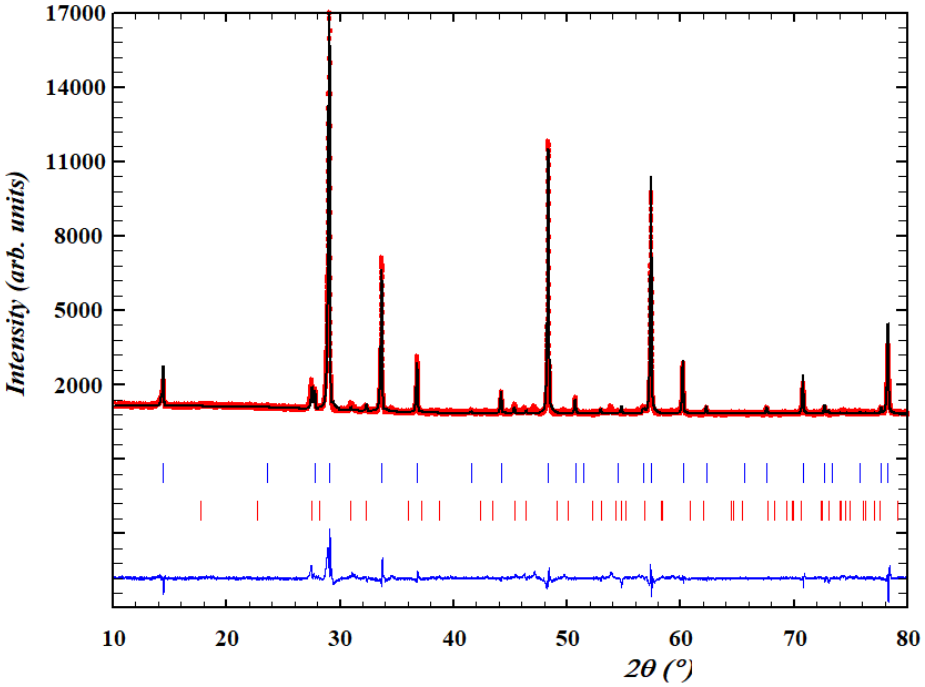

FIGURE 3.2: The X-ray diffraction refinement for La_2ScNbO_7, with the refined impurity of $LaNb_{1-x}Sc_xO_{4-x}$. Red points represent the observed data, the black line is the calculated pattern from the refined structure, the blue line is the difference between the calculated and observed patterns, and the green dashes represent calculated Bragg peak positions for La_2ScNbO_7 (upper ticks) and $LaNb_{1-x}Sc_xO_{4-x}$ (lower ticks).

wavelength range for NOMAD, 0.1-3 Å. Data were reduced using in-house software. The La_2ScNbO_7 was the same sample presented in figure 3.2 with a small impurity (not refined in the neutron data). Samples of Ln = Sm, Gd were excluded due to their high neutron absorption cross sections. Additionally, the NPD data obtained for Dy were too poor to use due to the high absorption cross section of Dy. NPD diffractograms were analyzed using the software suite GSASII [56]. For diffraction three of the six detector banks of NOMAD were utilized, with angles of 2Θ = 65.000, 120.400, 150.100°. The remaining detectors were not optimal for diffraction but were utilized for NPDF. Figure 3.3 shows the calculated refinement for the 120.400 ° 2θ detector bank, although all three were used in the refinements. Table 3.2 shows the results of these refinements. Figure 3.4 shows the unit cells obtained from both neutron and X-ray data. As expected, neutron and X-ray data show good agreement, and there is a monotonic increase in unit cell size with cation radius.

The high quality neutron diffraction data obtained from NOMAD allows for more

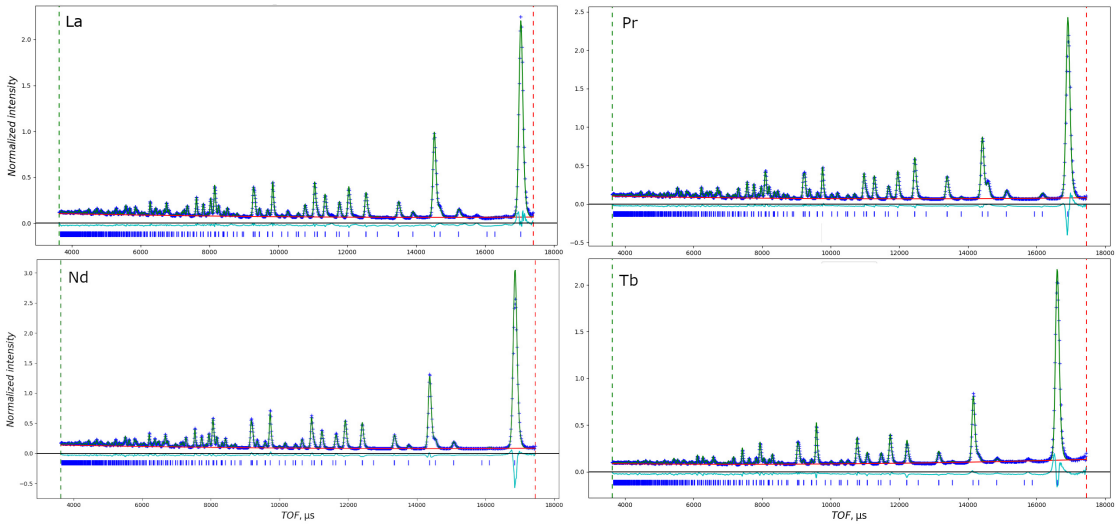

FIGURE 3.3: Time of flight neutron diffraction of viable Ln_2ScNbO_7 pyrochlores (Ln = La, Pr, Nd, Tb). Data were obtained on the NOMAD diffractometer, displayed data are from a single detector bank of the 3 refined detector banks (bank index 3, 4, and 5, bank 4 is displayed). Blue points are the observed data, the green line is the calculated pattern, the red line is the calculated background, the light blue line is the difference between the observed data and calculated pattern. The blue dashes are calculated Bragg peak positions.

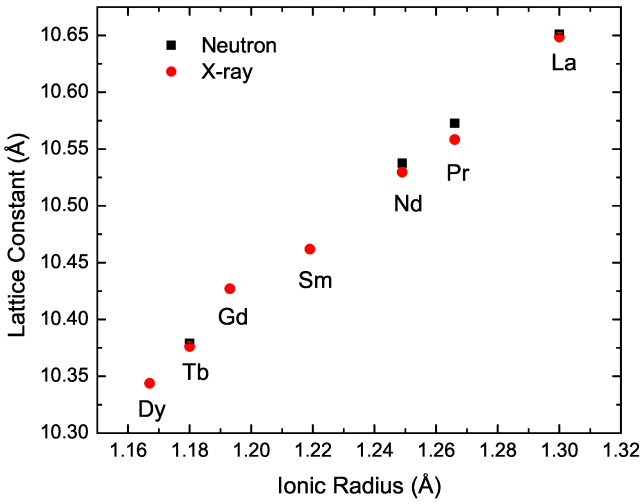

FIGURE 3.4: Unit cell trend with respect to ionic radius amalgamating the neutron and x-ray data. Error bars are included, but are mostly smaller than the data points.

TABLE 3.2: Neutron diffraction results refined from banks 3, 4 and 5 from the NOMAD data. The high symmetry position of O_{8b} has no allows off diagonal anisotropic terms. Reports of O_{48f} were simplified with the largest in diagonal and off diagonal components shown, as the lower symmetry site allows many anisotropic terms.

Ln	a (Å)	O_{48f} x (r.l.u)	Ln U_{11} (Å^2)	Ln U_{12} (Å^2)	B U_{11} (Å^2)	B U_{12} (Å^2)	O_{48f} U_{11} (Å^2)	O_{48f} U_{12} (Å^2)	O_{8b} U_{11} (Å^2)	R_{wp}
La	10.65122(8)	0.3270(1)	0.0131(3)	-0.0047(4)	0.035(2)	0.029(2)	0.0190(6)	0.0046(3)	0.0098(7)	0.05936
Pr	10.57265(6)	0.3290(1)	0.0119(3)	-0.0067(4)	0.015(2)	0.010(2)	0.0172(4)	0.0037(2)	0.0056(4)	0.04873
Nd	10.53779(8)	0.3298(1)	0.0138(4)	-0.0061(5)	0.005(4)	0.001(2)	0.0164(4)	0.0038(3)	0.0039(4)	0.05046
Tb	10.3790(1)	0.3372(2)	0.0152(6)	-0.100(6)	0.031(4)	0.020(4)	0.030(1)	0.0048(6)	0.009(2)	0.08521

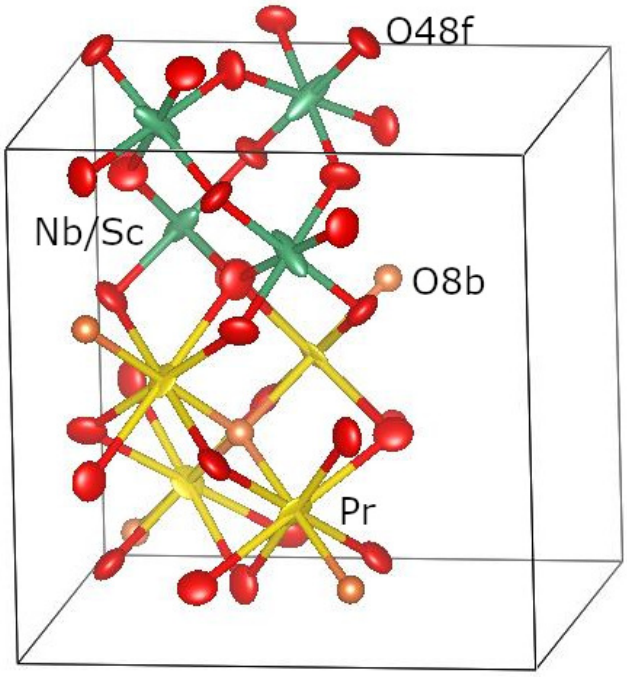

FIGURE 3.5: Visualization of the structure refined from neutron diffraction, portions of the unit cell are hidden for readability. Anisotropic thermal parameters are displayed at 95% probability and roughly model the prominent disorder. Pr_2ScNbO_7 is shown as a model, similar results exist for the other lanthanides.

information to be extracted from Rietveld refinement. Laboratory X-ray diffraction data is insufficient to refine the x position of O_{48f}, which is the only refinable structural parameter in the pyrochlore unit cell, due to the small relative x-ray scattering power of oxygen compared to the lanthanide and transition metals. Additionally the neutron data were used to analyze the anisotropic thermal parameters of all ions, which offer a crude insight into the nature of the disorder present in these systems (Fig. 3.5). The Ln site is heavily distorted normal to the local (111) axis, in the direction of the O_{48f} oxygens which are bonded to the B-site where the disorder originates from. The O_{48f} oxygens are distorted normal to the B-O-B bonds. Finally the B-site shows a very

large anisotropic disorder due to the site mixing that occurs between Nd^{+5} and Sc^{+3}. While this is all consistent with a structure that has large amounts of local disorder due to a disordered B-site with various ion charges, diffraction results are insufficient to understand any local ordering that may occur as diffraction only provides an average structure. One of the primary reasons for investigating this local disorder is to understand the impact that the O_{48f} distortions have on the crystal electric field and thereby the underlying magnetic ground states of the lanthanide ions. To obtain a somewhat better understanding of the local order NPDF is employed.

3.4 Pair Distribution Functions

The collection of neutron diffraction data described in 3.3 was primarily obtained for neutron pair distribution function analysis (NPDF). The Nanoscale-Ordered MAterials Diffractometer (NOMAD) is optimized for the collection of total scattering data out to high Q, allowing for NPDF analysis. Data from all detector banks was combined and transformed into a PDF by ORNL in-house software (Q_{max} = 35 Å), and normalized by sample mass and composition. Data were analyzed using the PDFGui software [78].

Here Nd_2ScNbO_7 is used as an example for the PDF refinements performed on Ln = La, Pr, Nd, Tb. Initial fits to the data were performed using the symmetric $Fd\bar{3}m$ unit cell refined from the neutron data for initial parameterization. The scale, O_{48f} x position, anisotropic thermal parameters, unit cell, and δ_1 (a r-dependant peak sharpening) were fit (Fig. 3.6) over a range of 1-40 Å. This fit yields, scale = 0.856(15), O_{48f} x = 0.324(11), Nd U_{11} = 0.0096(7), Nd U_{12} = 0.00007(72), B U_{11} = 0.0072(5), B U_{12} = 0.0005(37), O_{48f} U_{11} = 0.0076(6), O_{48f} U_{12} = 0.00052606, O_{8b} U_{11} = 0.0064(5) δ_1 = 0.84(18), R_{wp} = 0.109. This fit represents the long-range data very well, however figure 3.6 demonstrates that over the first coordination shell (1-4 Å) some of the correlations are poorly represented, namely O-O correlations.

In preparation to fit the short-range correlations, a better structural fit was desired. This was achieved by transforming the $Fd\bar{3}m$ pyrochlore structure into the primitive cell, and fitting each oxygen position independently to approximate the disorder present in the system. A similar fit was performed from 1-40 Å yielding; scale =

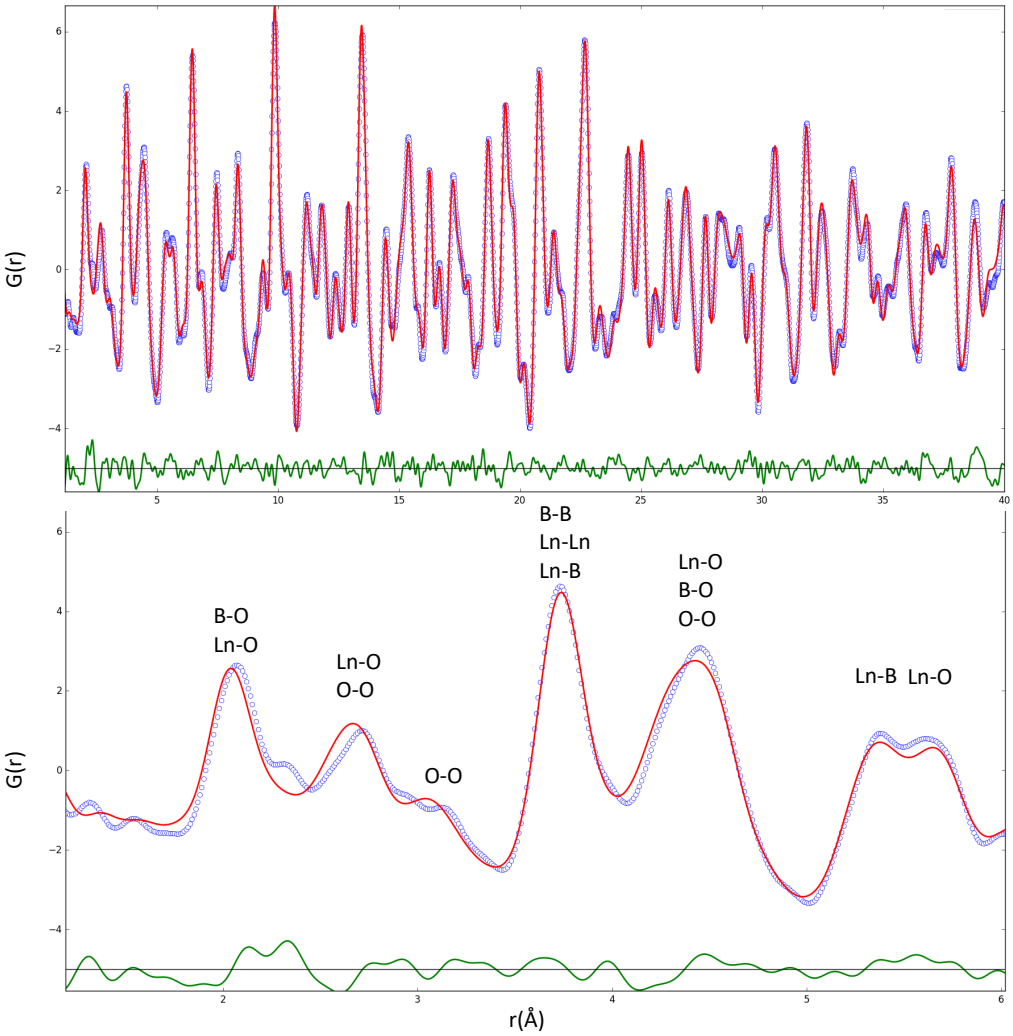

FIGURE 3.6: NPDF fit using the symmetrized Fd$\bar{3}$m unit cell over 1-40Å. Blue points are reduced data, the red line is the calculated fit, and the green line is the residual difference. The bottom figure is an expansion of the low r data, with peaks labeled for the correlations that contribute to their intensity.

0.956(16), Nd U_{11} = 0.0079(43), Nd U_{12} = -0.0001(0.0052), B U_{11} = 0.0063(29), B U_{12} = -0.0004(34), O_{48f} U_{11} = 0.007(4), O_{48f} U_{12} = -0.001(10), O_{8b} U_{11} = 0.0057(85) δ_1 = 1.34(19), R_{wp} = 0.114. While this fit is slightly worse over the range 1-40 Å, based on the R_{wp} values, it does fit the short-range correlations slightly better (Fig. 3.7). As the occupancies are not altered, the overall scattering intensities will remain the same meaning this fit will not interfere with fitting the short-range correlations. Additionally figure 3.8 compares the symmetrized cell (a) and the primitive cell (b). Visually they look identical, demonstrating that the primitive cell accurately replicates the symmetrized cell. The only significant difference is how the correlation distribution changes, with the primitive cell showing a larger distribution in bond

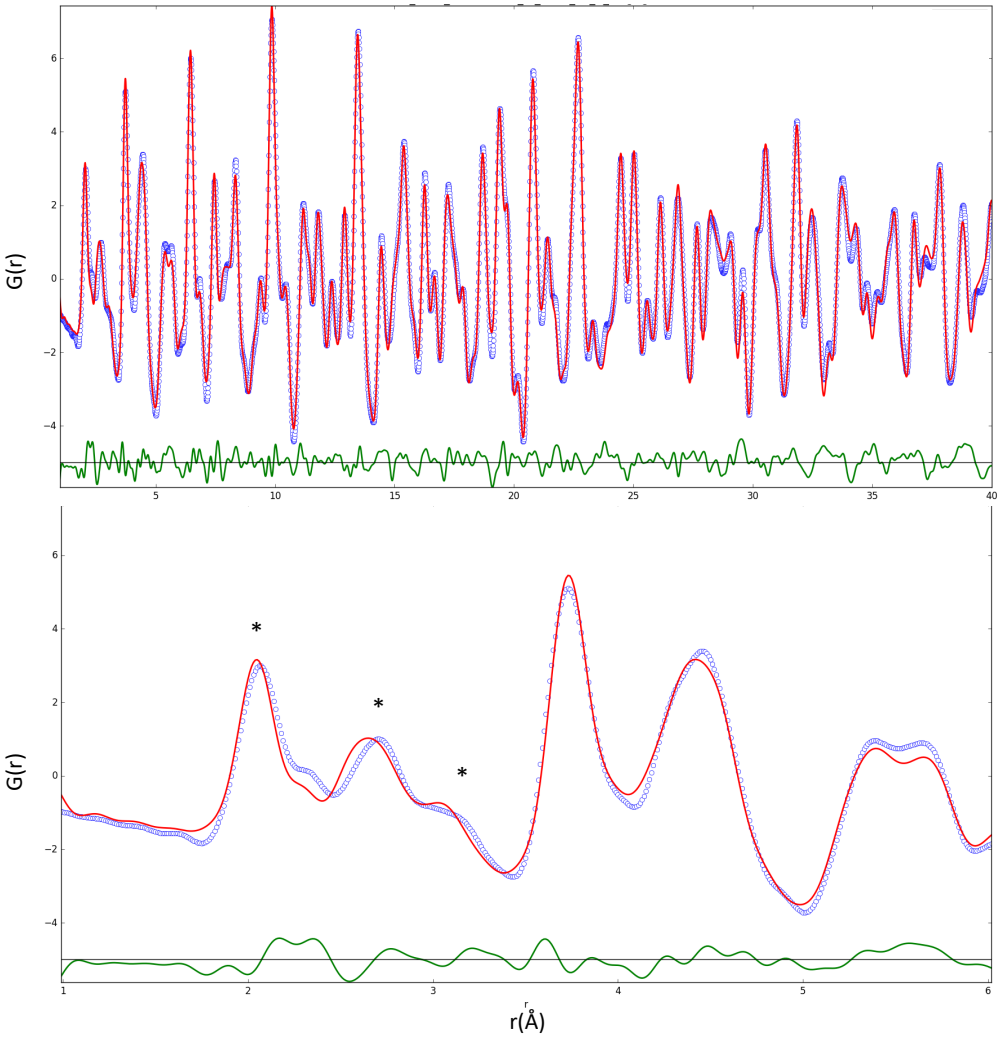

FIGURE 3.7: NPDF fit using the primitive unit cell over 1-40 Å. Blue points are reduced data, the red line is the calculated fit, and the green line is the residual difference. The bottom figure is an expansion of the low r data, with peaks labeled (*) showing the most significant difference from the symmetrized fit (Fig. 3.6).

lengths, suggesting that the anisotropic thermal factors alone were insufficient to describe the distribution of atoms over small r for the symmetric cell refinement. This is likely a result of the distribution of ions due to the chemical disorder following a non-normal distribution, unlike actual thermal vibrations which these thermal parameters are designed to be modelling.

To properly understand the disorder present in the Ln_2ScNbO_7 the local ordering of the nominally disordered Sc and Nb must be considered. Within the crystallographic description, the 16c B-site has a mixed occupation of 0.5 Sc and 0.5 Nb with their positions being nominally random. While there is no long-range ordering of the Sc and Nb on this site, which would lead to a crystallographic symmetry breaking

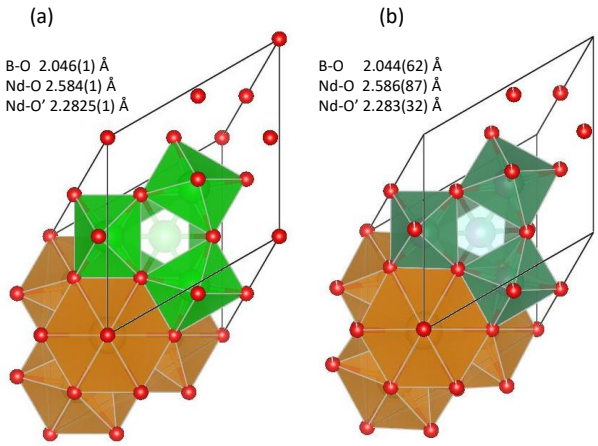

FIGURE 3.8: (a) Refined crystallographic Fd$\bar{3}$m unit cell from neutron diffraction, shown in the primitive lattice. Bond length errors are extracted from refinement errors. (b) Refined primitive unit cell from neutron PDF for Nd_2ScNbO_7. Orange polyhedra contain Nd, green polyhedra contain Sc/Nb. Bond length errors are extracted as a standard deviation from the distribution of oxygen bond lengths.

that is not observed, Sc and Nb ions are likely to show some short-range ordering. As there are large differences in charge and size between Sc^{+3} (0.885 Å) and Nb^{+5} (0.78 Å) [18], any clustering of fully Sc and Nb would lead to a charge buildup and a large deal of crystallographic strain. It is more likely that at the nearest-neighbour level the Sc and Nb ions alternate in some fashion to prevent clustering. The fact that the 16c B-site is comprised of a tetrahedral corner shared lattice precludes perfect alternation of Sc and Nb ions, which likely contributes to the lack of long-range order. One possible way for the B-site to minimize Sc-Sc and Nb-Nb correlations is to form a charge ice state observed in other comparable systems such as the spinel $CsNiCrF_6$ [79] where Ni and Cr form a charge ice structure or the ice structured $Cd(CN)_2$ [80]. This 'ice' ordering is comprised of corner-shared tetrahedra of disordered ions or dipoles with binary ordering options (C≡N or N≡C), which order on the local tetrahedron levels. In $Cd(CN)_2$ the Cd ions mimic oxygen in conventional water ice sitting at the centre of tetrahedra of C≡N dipoles that orders with nitrogens pointing towards the centre of the tetrahedron on two corners of the tetrahedron and two carbons pointing into the centre on the remaining two corners (a 'dipole-ice' similar to water ice). More directly comparable to Ln_2ScNbO_7, in $CsNiCrF_6$, the Ni^{+2} and Cr^{+3} ions form a disordered tetrahedral network in the spinel structure. These (II)

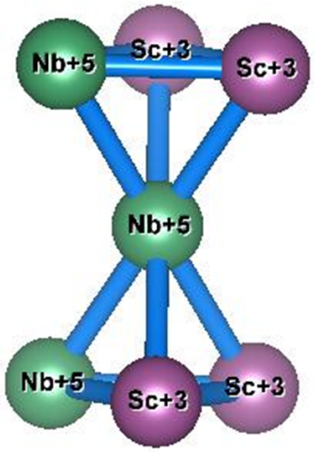

FIGURE 3.9: An example of two tetrahedra satisfying the 'charge ice' condition in a Ln_2ScNbO_7 pyrochlore, with two Sc^{+3} and two Nb^{+5} per tetrahedron. Note that there are many equivalent configurations satisfying this condition.

and (III) ions order on the single tetrahedron level such that each tetrahedron contains two Ni^{+2} and two Cr^{+3}. If nearest neighbour correlations strongly favour Sc-Nb neighbours then this 'charge ice' is what might be expected to occur in Ln_2ScNbO_7 (Fig. 3.9).

The PDF data can be used to determine whether Sc and Nb are ordered or form a short-range correlated structure as PDF is sensitive to the magnitude of nearest neighbour Sc-Nb, Nb-Nb, and Sc-Sc correlations which all appear as intensity on the peak near 3.8 Å. As Sc and Nb have good neutron contrast with scattering lengths of 12.3 fm and 7.05 fm respectively [81], the relative concentration of these correlations can be refined with a starting parameterization of 0.5 Sc-Nb : 0.25 Nb-Nb : 0.25 Sc-Sc as would be expected of a random distribution. A single parameter x was used, that yields correlations of (0.5+x) Sc-Nb : (0.25-$\frac{x}{2}$) Nb-Nb : (0.25-$\frac{x}{2}$) Sc-Sc which effectively fixes the atomic occupancies to the stoichiometric values while refining the relative scattering from each correlation. Here a perfect charge ice ordering would yield 0.66 Sc-Nb : 0.167 Nb-Nb : 0.167 Sc-Sc. This fit was performed over a range of 1-6 Å so as not to include long-range B-site correlations, fixing the structural values refined from the long-range fit and only fitting the scale factor and the correlation parameter x (Fig. 3.10). Using Nd_2ScNbO_7 as an example, this fit yields a relative fraction of 0.655(96) Sc-Nb : 0.172(48) Sc-Sc : 0.172(48) Nb-Nb, with an R_{wp} of 0.110 over the

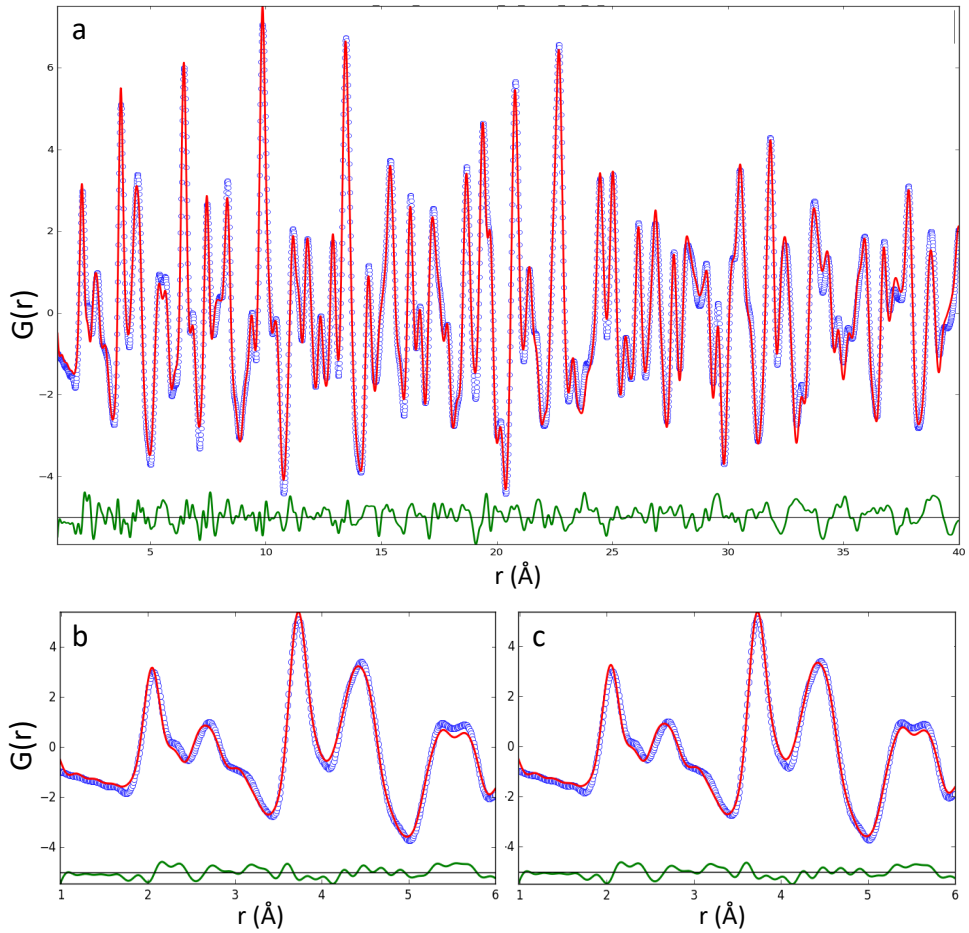

FIGURE 3.10: (a) NPDF fit using the two parameter correlation method described in text, expanded beyond the fit range to show the full PDF. (b) NPDF fitting only the scale factor, with parameterization taken from the primitive fit. (c) NPDF fit using the two parameter correlation method over the fitted region. Blue points are reduced data, the red line is the calculated fit, and the green line is the residual difference.

1-6 Å fit compared to a R_{wp} of 0.112 without fitting the correlation parameter over the same range.

The results of the short range fit for Ln = La, Pr, Nd, Tb can be seen in figure 3.11. The error bars are very large in this measurement, primarily due to the fact that the B-B correlations coincide with the Ln-B and Ln-Ln correlations which reduces the contrast. Despite this it can be seen that the large cation Ln_2ScNbO_7 (Ln = La, Pr, Nd) pyrochlores do show a frequency of Sc-Nb correlation higher than what could be expected of a random distribution. There is no notable change within these large cation members but there appears to be a drop in the correlation frequency by Tb_2ScNbO_7 suggesting that there might be a sudden drop between intermediate members of the series. However, the limited number of neutron viable samples

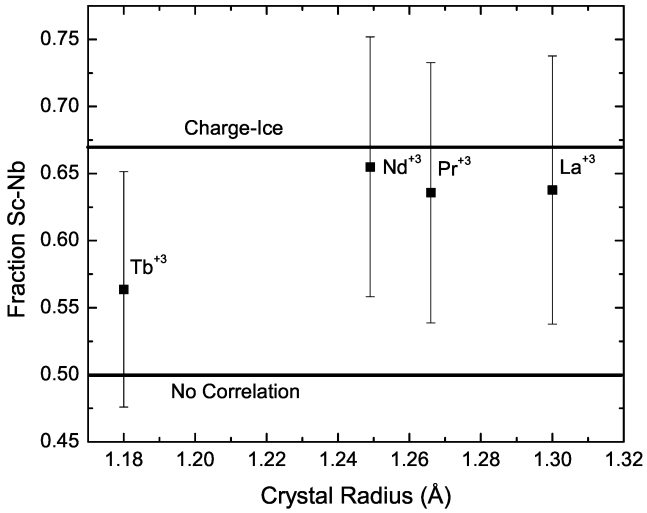

FIGURE 3.11: Relative frequency of Sc-Nb correlation out of all B-B correlations shown for each lanthanide with NPDF data. Lines mark the extreme expected values from no correlations, to perfect nearest-neighbour correlations (Charge Ice).

restricts any conclusive analysis. The large cation pyrochlores seem to consistently approach charge ice values of correlations, suggesting that these systems are charge ices, potentially with a relatively large concentration of defects.

These fits in and of themselves are deserving of some skepticism. For example site mixing between the A and B site might also lead to differing peak intensities. But that should cause consistent shifts in peak intensities which should be true over any observable range. In order to establish that the observed values are in fact due to short-range correlations in some form, the same 2 parameter correlation fit is performed over longer ranges. As the fitting range in r becomes large we should expect the refined values to regress back to the 'no correlation' value of 0.5 (Fig. 3.12). These fits tend towards random occupancy for each sample, confirming that these fits are the result of short-range correlations. Most short-range correlations should lead to peak broadening or splitting, but a change in intensity should only be achievable by a non-random distribution of B-B correlations as this is the only mixed occupancy site. Additionally, this correlation fit was performed on the symmetric cell in the same manner as the primitive cell for Nd_2ScNbO_7, with very similar results but a slightly larger error margin, confirming that the primitive cell is reasonable for fitting these systems.

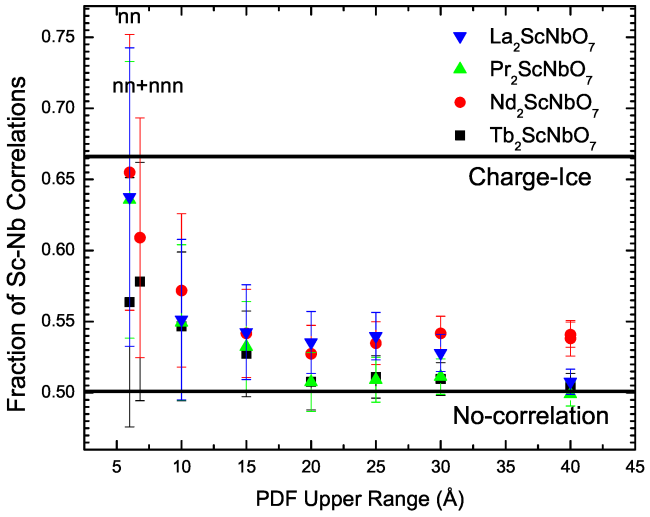

FIGURE 3.12: The fraction of Sc-Nb correlations, with the rest being Sc-Sc and Nb-Nb in equal proportion as a function of the fitting range maximum. The line at 2/3 represents the theoretical result of charge ice, the line at 1/2 is the expected result of a system with random occupancy, which the fit should trend to at long upper range. The abbreviation nn represents the fit with only nearest neighbour B-B correlations, and nn+nnn represents the first two correlation spheres, with later fits including longer range correlation spheres.

3.5 Conclusions

Three additional members of the Ln_2ScNbO_7 are presented (Ln = La, Sm, Tb) in addition to those presented by Zouari *et al.* [46]. Large single crystals of Ln = Pr, Nd, Sm, Gd, Tb, and Dy have been prepared for neutron scattering experiments. Anisotropic thermal parameters extracted from neutron diffraction data demonstrate that there are large anisotropic distortions present in the structure due to the disorder induced by the B-site sharing of Sc^{+3} and Nb^{+5}, with this disorder being mostly constant throughout the various members of the series. To establish the nature of the short range correlations between Sc^{+3} and Nb^{+5}, NPDF was employed. The large cation members of this series (Ln = La, Pr, Nd) show a preference for Sc-Nb correlations over statistical values with frequencies ranging from 0.636(97)-0.655(96), while the smaller Tb appears to show a significantly smaller correlation preference at 0.564(87). While this trend appears consistent it is somewhat counterintuitive, with the larger cation systems appearing to have less impact on the overall structure in favour of Sc and Nb. Ideally, the sample Dy_2ScNbO_7 could also be analyzed to give another small cation example. This could be done in the future when activated

samples of isotopically enriched, less absorbing ^{160}Dy become available. Although it is hard to establish trends, correlations of Sc^{+3} and Nb^{+5} do exist in some of these systems above statistical levels, and the systems appear to approach charge ice ordering (although it is difficult to establish the level of defects given the high error associated with these measurements).

Chapter 4

Magnetic and Structural Symmetry Breaking in Nd_2ScNbO_7

4.1 Introduction

Two of the parent compounds of Nd_2ScNbO_7, $Nd_2Zr_2O_7$ and $Nd_2Hf_2O_7$ have become topical systems due to the experimental observation of signatures of 'moment fragmentation' [82, 83]. Generically, moment fragmentation consists of the simultaneous observation of long-range symmetry breaking order (Bragg peaks) and liquid scattering (diffuse scattering) [24, 84]. The neodymium pyrochlores exhibit a particular case of moment fragmentation that derives from the dipole-octupole symmetry that arises due to their crystal field ground state [24, 82]. The result is a fragmented moment in which roughly half of the moment contributes to antiferromagnetic Bragg peaks in the elastic scattering. This represents of a 'divergence-full' component that is functionally equivalent to the 'All-in All-out', Γ_3 Ising antiferromagnetic ground state on the pyrochlore lattice. Associated magnons are also observed. The remainder of the moment remains inelastic giving a 'divergence-free' spin ice scattering pattern gapped away from the ground state [82, 84]. The divergence terminology is taken from classical spin ice literature as moment fragmentation has been seen as a realization of magnetic monopole crystallization, where spin ice excited quasiparticles crystallize into an antiferromagnetic lattice [82, 85, 86]. 'Divergence-full' refers to a system with a net magnetic divergence (in the spin ice interpretation, there is no actual magnetic divergence, *ie.* $\nabla \cdot \vec{B} \neq 0$ does not occur). This would include 'All-in' and 'All-out' tetrahedra. On the other hand 'two-in', 'two-out' tetrahedra would

have no net magnetic divergence and are considered 'divergence-free'. It is worth noting that O. Benton [24] has provided a more robust theoretical analysis of the dipole-octupole moment fragmentation phenomenon that is not reliant on monopole crystallization. Benton's interpretation along with previous theoretical work [23, 82] establish that a dipole-octupole ground state, which include $m_j = \frac{3}{2}, \frac{9}{2}$ & $\frac{15}{2}$ single ion states for pyrochlores with $\overline{D_{3d}}$ double group symmetry is required for this case of moment fragmentation.

Here the charge disordered variant of these fragmented dipole-octupole systems is investigated, and it can be seen that the structural disorder plays a large part in destroying the local symmetry required for the dipole-octupole case of moment fragmentation. As a result, the signatures of moment fragmentation are largely supressed.

All of the work in this chapter was performed by the author with the exception of the data collection for the powder crystal electric field measurements on SEQUOIA, which were performed remotely with the help of Adam Aczel and Matt Stone (ORNL). The majority of the data from this section is reproduced from C. Mauws *et al.*, 2021 [76].

4.2 Methods

Inelastic neutron scattering measurements of the crystal electric field (CEF) were taken on the SEQUOIA spectrometer at the Oak Ridge National Laboratory (ORNL) [87]. Measurements were taken powder samples of Nd_2ScNbO_7 and the non-magnetic analogue La_2ScNbO_7 to act as a phonon standard. Data were collected at 5, 100, and 250 K using incident energies (E_i) of 10.5, 60 and 140 meV using the low resolution configuration with a resolution of roughly 3% E_i, at the elastic line. The phonon subtraction allows an approximate means of removing the inelastic contribution of the phonon scattering which was necessary due to the broad scattering observed. The phonon standard was normalized using Bragg peak intensities calculated from the refined crystal unit cells using FullProf Suite [55], yielding an intensity correction of 0.82 for the La_2ScNbO_7 standard prior to direct subtraction. The resulting spectrum was fit using a series of Gaussians to extract excitation intensities and centre of

mass energies. The errors reported are the associated fitting errors with data error integrated into the fitting process.

Direct current (DC) magnetization measurements were taken on a Quantum Design PPMS using a VSM magnetometer. A powder sample of 6.1(1) mg of Nd_2ScNbO_7 was mounted in a polypropylene sample holder. Reported susceptibilities were empirically corrected for the diamagnetism of the sample holder and corrected for the sample's diamagnetism using values amalgamated in Bain and Berry (2008) [88]. Alternating current (AC) measurements were performed on a powder sample at the National High Field Magnet Lab using an in-house SQUID mounted in a dilution refrigerator cryostat. Temperature sweeps were performed at 153 and 1310 Hz. Some errors occurred in the measurements, including an issue in the AC phase. To improve readability the 1310 Hz data in figure 4.6 has been shifted vertically by 0.32 x 10^{-7} (arb.). Due to these issues only the temperatures remain accurate while the intensities are qualitative.

Polarized neutron diffraction was performed at the Diffuse Neutron Scattering (DNS) spectrometer at FRM II [89]. A single crystal of Nd_2ScNbO_7 was aligned in the [HHL] plane. Measurements were taken from 100 mK to 1300 mK as well as 5 K and 10 K, using a wavelength of 4.1916 Å. Inelastic neutron scattering measurements of the magnetic excitation were taken at the Disk Chopper Spectrometer (DCS) at the NIST CHRNS [90]. The same single crystal was used with data taken in the [HHL] plane at temperatures of 60 mK and an empty 20 K cryostat was used for background subtraction. Wavelengths of 8 Å and 6.5 Å were used, where the 8 Å data yields an energy resolution of roughly 30 μeV. The depicted data uses no frame overlap chopping.

4.3 Crystal Electric Field and Magnetization

Neodymium pyrochlores typically show a ground state consisting of $m_j = < \frac{3}{2} >, < \frac{9}{2} >$, which follows a dipole-octupole symmetry. To confirm that this holds true for Nd_2ScNbO_7, CEF spectroscopy was performed. Figure 4.1 shows the results of this spectroscopy for the 60 meV E_i scan. Based on previous work on other neodymium pyrochlores [91] three of the four excited doublets were expected to be found in

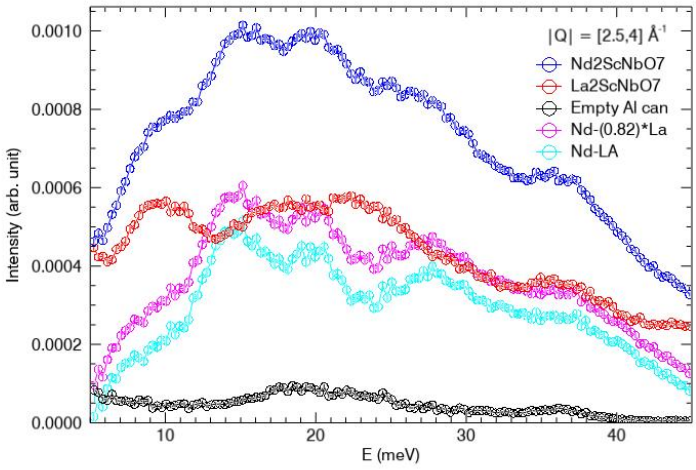

FIGURE 4.1: Cuts along energy from the 60 meV incident energy data from the SEQUOIA spectrometer, showing the raw data of La_2ScNbO_7, the direct subtraction and the 0.82 self-shielding factor corrected subtraction.

this range. Instead of a series of sharp, resolution limited peaks corresponding to CEF and phonon excitations, a broad anomaly is observed. The broad anomaly is overlayed by a series of sharper, but not resolution limited peaks. As this broad feature has contributions from CEF excitations, as well as phonons the phonon standard La_2ScNbO_7 is employed to approximately remove the phonon contribution (Fig. 4.1). The resulting spectrum in figure 4.2 can be seen as a better approximation of the total CEF scattering. The phonon at 8 meV is well removed by the standard, and the broad feature better approaches zero intensity at either extreme in energy. The phonon at 36 meV is not perfectly removed but is assigned as a phonon anyways as it is clearly observable in La_2ScNbO_7 despite being shifted slightly both in energy and intensity. To confirm the remaining intensity is due to crystal field excitations the observed Q-dependence of the peaks is compared to the form factor of neodymium (Fig. 4.3).

Fitting is performed as a series of 5 Gaussian peaks (Fig. 4.2); the peak labeled e_0 is the broad background of CEF excitations, the e_i peaks represent the fitted crystal electric fields and p_1 is the improperly subtracted phonon. It should be noted that a fit using a linear background with 4 sharp Gaussians could not replicate the data reasonably. The extracted CEF peaks along with an additional peak fit from the 140 meV E_i data, fit for energy position only are used to calculate a crystal field

description. However this is clearly not representative of most of the Nd ions as these sharp peaks only comprise 14(2) % of the total CEF intensities. This mixture of sharp and broad scattering features is clearly a result of the intrinsic chemical disorder in these systems distorting the local anion environment, but it is not immediately clear what separates the sharp and broad excitations.

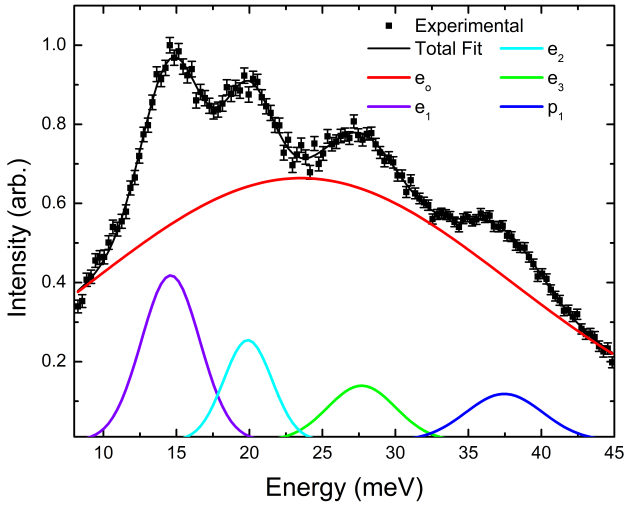

FIGURE 4.2: Electronic excitation spectrum at 5 K of Nd_2ScNbO_7 taken on SEQUOIA using La_2ScNbO_7 at 5 K as a phonon correction, and integrated over Q from 2.5-4 $Å^{-1}$. Discrete crystal electric fields are labeled e_i with the broad anomaly labeled e_0, and p_1 is an imperfectly subtracted phonon.

The extracted CEF peaks are fit to a Wybourne description of the crystal field using the Spectre software package [68], under an assumed hexagonal local symmetry (D_3 or D_{3d}). This is described by the six parameter crystal field Hamiltonian:

$$H_{CEF} = B_2^0 C_2^0 + B_4^0 C_4^0 + B_6^0 C_6^0 + B_4^3 C_4^3 + B_6^3 C_6^3 + B_6^6 C_6^6 \tag{4.1}$$

Initial parameterization for the refinement was taken from $Nd_2Zr_2O_7$ [91]. The refinement yielded parameters of $B_2^0 = -36.36$ meV, $B_4^0 = 442.4$ meV, $B_6^0 = 186.2$ meV, $B_4^3 = 173.7$ meV, $B_6^3 = -66.75$ meV, and $B_6^6 = 118.8$ meV. The results of the crystal field refinement are reported in table 4.1.

The refined parameterization is dramatically different from those reported for other neodymium pyrochlores, likely due to a dramatic displacement of the local oxygen environment. The resulting crystal field ground state, $\psi_{1,2} = 0.85 < \frac{9}{2} > + 0.51 < \frac{3}{2} >, -0.85 < \frac{9}{2} > - 0.51 < \frac{3}{2} >$ does contain the correct $< \frac{9}{2}, \frac{3}{2} >$

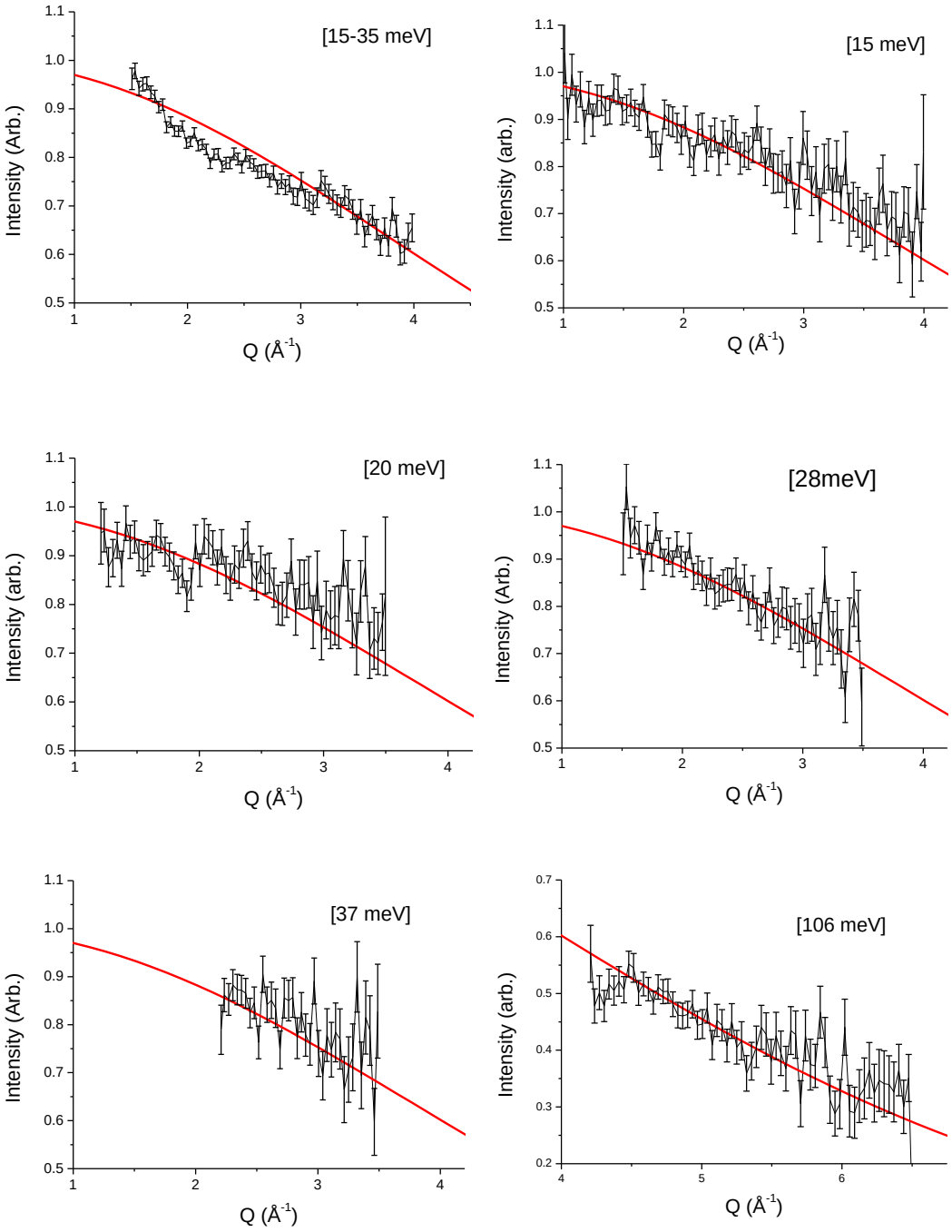

FIGURE 4.3: Q-dependent cuts of the various inelastic features (black data) from SEQUOIA, with the squared magnetic form factor of Nd^{+3} overlayed. Unless otherwise mentioned, energy integration ranges are ± 1 meV.

TABLE 4.1: Crystal electric field results for Nd_2ScNbO_7 within the ground state J-manifold (all levels are doublets). Unlabelled intensities are due to being unable to extract relative intensities while using a higher E_i. Basis with contributions less than 0.01 are excluded, including higher multiplet contributions.

E_{obs}(meV)	I_{obs}	E_{fit}(meV)	I_{fit}	$\pm\frac{1}{2}$	$\pm\frac{3}{2}$	$\pm\frac{5}{2}$	$\pm\frac{7}{2}$	$\pm\frac{9}{2}$
0.0		0		0	0.51	0	0	0.85
14.6(1)	1	13.52	1	0.77	0	0.63	0.01	0
19.9(1)	0.5(1)	20.92	0.46	0	0.85	0	0	0.50
27.7(1)	0.4(2)	28.23	0.5	0.55	0	0.66	0.47	0
106.5(1)	-	104.86	-	0.30	0	0.38	0.86	0

Ising dipole-octupole symmetry, with a similar total moment of 2.0 μ_B to other neodymium compounds. The inverse magnetic susceptibility calculated from this crystal field scheme is compared to experimental data in figure 4.4, and clearly the crystal field scheme is not representative of the bulk system. Comparison of the bulk system to calculations performed on the results for $Nd_2Zr_2O_7$ reported by Zu *et al.* [91] are also not representative of the bulk. As this crystal field is only representative of 14(2) % of neodymium ions in the system the refined moment cannot be considered representative of the entire system, and clearly many of the neodymium ions are not accurately represented by this crystal field description. To resolve this ambiguity, magnetization measurements are performed (Fig. 4.4) to determine a saturation magnetic moment. The saturated magnetic moment for an Ising system is $\frac{1}{2}\ \mu_{total}$ which yields a total moment of 2.5(1) μ_B. This interpretation is likely a better representation of the total moment of the system, but is also problematic as it assumes the system is perfectly Ising, which may not be the case as CEF mixing may alter the anisotropy in some neodymium ions.

The final issue to resolve with the CEF is the suspicious combination of both broad and sharper but not resolution limited excitations in the 60 meV E_i data set. While the broadened crystal fields are a consequence of the disordered B-site inducing distortions on the A-site's oxygen environment, the clear distinction between broad and sharp features is not so easily explained. Instead it suggests that one particular case of distortions has a significantly higher probability of occurring, where others form the broad background. As each neodymium ion is surrounded by a hexagon of B-site ions, a particular configuration of this hexagon having a higher probability of occurring than others could give rise to the observed crystal field spectrum.

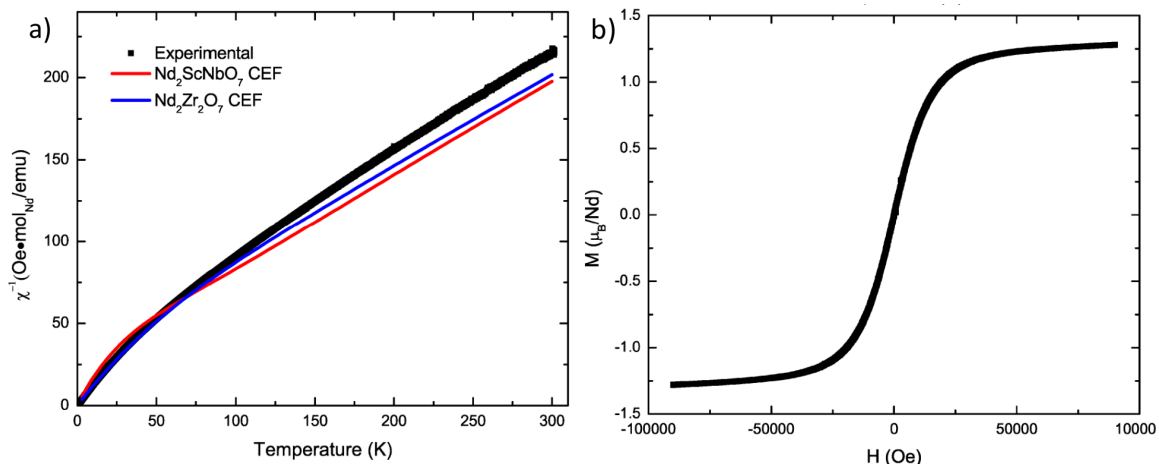

FIGURE 4.4: (a) Inverse DC magnetic susceptibility in a 1000 Oe applied field on a powder sample of Nd_2ScNbO_7 (Black), with calculated susceptibilities for the experimentally determined crystal field (Blue) and calculated values for $Nd_2Zr_2O_7$ (Red), taken from the crystal field parameters presented in X. Zu *et. al.* [91]. (b) Magnetization measurements on powder Nd_2ScNbO_7 at 1.8 K with a maximum applied field of 90000 Oe.

As discussed in chapter 3, the probability of Sc-Nb neighbors are higher than what would be expected of a random distribution and may approach charge ice patterns. If a charge ice model is assumed then a local environment of Sc-Nb alternating tetrahedra (Fig. 4.5) would have the highest probability of occurring compared to any other local environment, even when considering equivalent multiplets. The probability of having a hexagon of alternating Sc and Nb ions (labeled D_3 in Fig 4.5) in a charge ice case is 17.6 %, by statistical calculation and by Monte Carlo simulation. This is higher than the observed 'preferred' configuration from spectroscopic data at 14(2) % but is consistent with a case where the system has a charge ice configuration with significant, non-charge ice defect concentrations. A Monte Carlo simulation of the local A-site environment which allows for defects was performed. Repeated generations (10^7) of the 6 local tetrahedra about the A-site were randomly populated with Sc or Nb ions. Under the ideal charge-ice case only cases meeting the charge ice were accepted, and then the D_3 ordering case was checked for, yielding 17.6 % under the charge ice condition. A variable probability of allowing defect tetrahedra through with an exponentially decreasing probability based upon the number of defects in the local coordination sphere was introduced, and the probability was varied until the desired 14 % was reached. The simulation yields an average defect concentration of 0.15 defects per tetrahedron, for a D_3 local configuration probability of 14 %. This

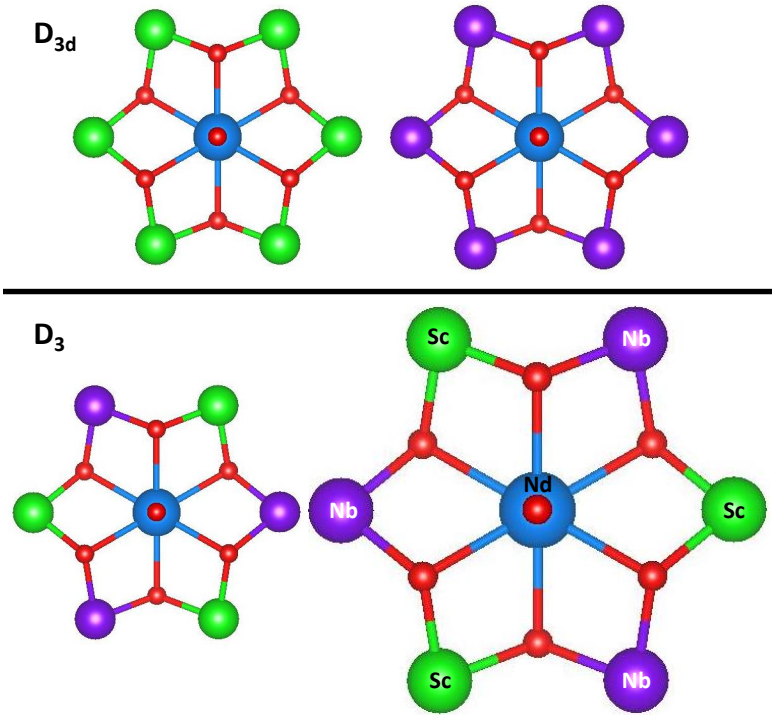

FIGURE 4.5: Possible local environments of Sc^{+3} and Nb^{+5} that retain a C_3 rotation centre, of the possible 2^6 configurations. The D_{3d} configurations maintain the crystallographic site symmetry, whereas the D_3 configurations have lost inversion. The configuration in the bottom right is enlarged to accommodate labelling that applies to all configurations.

appears consistent with PDF results and further supports that Nd_2ScNbO_7 shows charge ice behavior with a significant defect concentration.

4.4 Magnetic Neutron Diffraction and Spectroscopy

Low temperature AC magnetic susceptibility measurements show a frequency independent magnetic transition at 0.37 K, consistent with a Néel transition (Fig. 4.6). Polarized neutron diffraction is used to investigate the magnetic structure (Fig. 4.7). The spin flip scattering with a high temperature background subtraction shows clear intensity on the (220), (311), and (331) peaks indicative of Γ_3 ordering. The Γ_3 irreducible representation only contains a single basis, that is the so called 'all-in, all-out' (Fig. 4.6) Ising antiferromagnetic structure found in other neodymium pyrochlores. Also visible is a spin ice like scattering pattern with scattering intensity along the [00L] and [HHH] directions but lacking the clear pinch point signature at (111) and (002) observed in classical spin ice, where the diffuse scattering converges to those

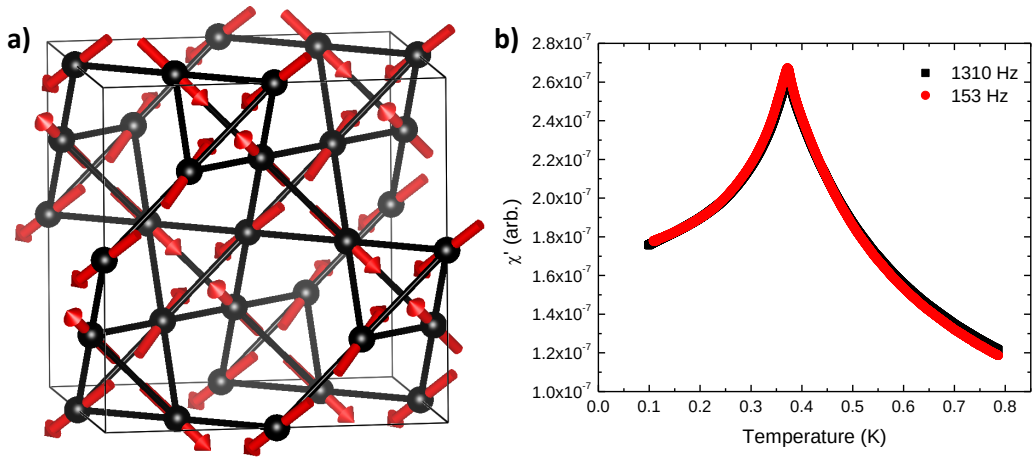

FIGURE 4.6: (a) The pyrochlore lattice with antiferromagnetic all-in, all-out (AIAO) order along a local <111> Ising axis. (b) AC susceptibility of powder Nd_2ScNbO_7 noting a peak near T_N = 0.37 K. No frequency dependent shift is observed.

TABLE 4.2: Comparison of the ordered all-in, all-out (AIAO) moment in the known Neodymium pyrochlores

Pyrochlore	AIAO moment (μ_B)	Reference
Nd_2ScNbO_7	2.2(4)	This work
$Nd_2Zr_2O_7$	1.26(2)	J. Xu *et al, 2015*
$Nd_2Zr_2O_7$	0.8(1)	S. Petit *et al, 2016*
$Nd_2Sn_2O_7$	1.708(3)	A. Bertin *et al, 2015*
$Nd_2Hf_2O_7$	0.62(1)	V. K. Anand *et al, 2015*
CEF limit	2.0-2.5	This work

Bragg points. Figure 4.7 tracks the intensity of the diffuse scattering at $(\frac{3}{2}, \frac{3}{2}, \frac{3}{2})$ and the Bragg scattering at (220). The Bragg scattering appears at the Néel temperature, whereas the diffuse scattering appears at higher temperature reaching a maximum at 0.60 K before reducing in intensity and seemingly plateauing below the Néel temperature.

The magnetic scattering is refined to the Γ_3 structure as determined by the SARAh representational analysis software [60] and refined using the Fullprof Suite [55], to an ordered moment of 2.2(4) μ_B using 5 structural peaks and 2 magnetic peaks. The magnitude of the ordered moment is near the total moment, somewhere in the range of 2.0-2.5 μ_B. While some ambiguity remains and some of the scattering moment must remain in the diffuse scattering, this moment is much higher than what is observed in the neodymium moment fragmentation systems $Nd_2Zr_2O_7$ and $Nd_2Hf_2O_7$ (Tab. 4.2).

The diffuse scattering in the moment fragmentation neodymium pyrochlores is an inelastic feature gapped away from the elastic line, which could explain the

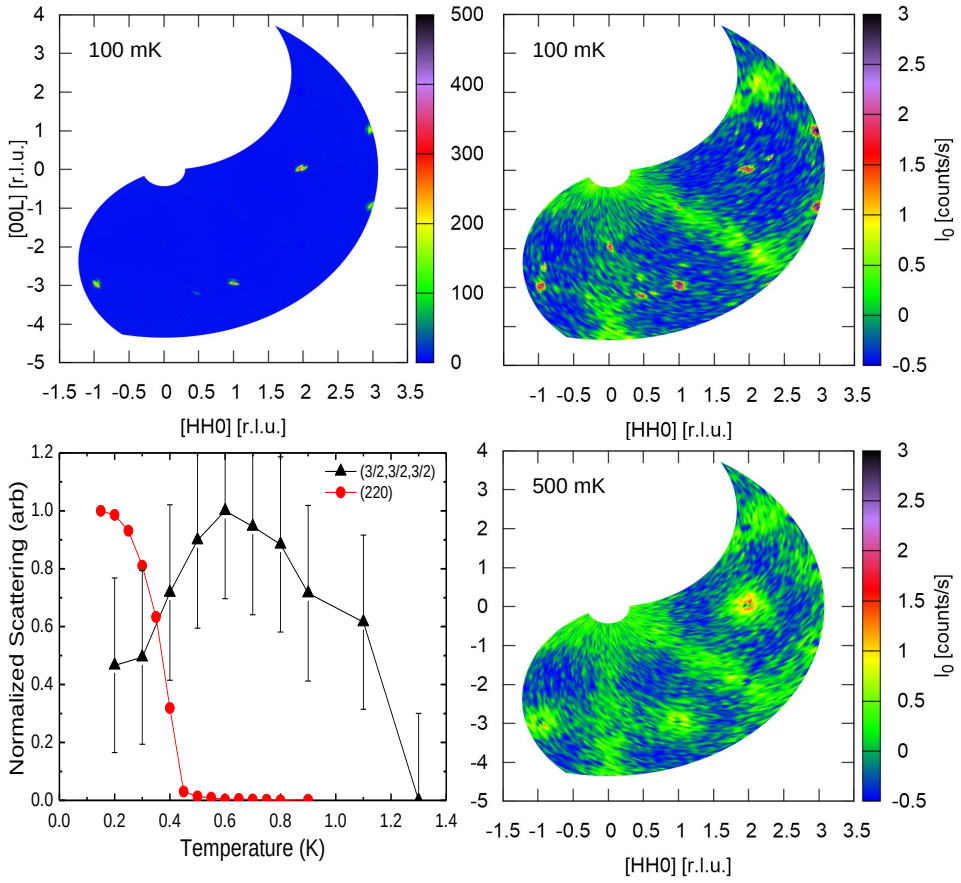

FIGURE 4.7: Spin Flip difference scattering with polarization in the [H,-H,0] plane shown on two intensity scales (left and right) obtained on DNS at FRMII. The temperature dependence of an antiferromagnetic Bragg peak (220) and the spin ice like diffuse scattering (3/2,3/2,3/2) (bottom left). Spin Flip difference scattering with polarization in the [H,-H,0] plane above the Néel order (bottom right).

lack of clear pinch points in this diffuse scattering data. Inelastic magnetic neutron scattering is performed on the DCS in order to resolve this (Fig. 4.8). A weak inelastic signal is observed centred at 67(1) μeV, which shows no dispersion. The signal is too weak to observe in the full [HHL] plane so the |Q| integrated data is shown. There is no evidence of magnons normally associated with the 'all-in', 'all-out' structure, which is possibly due to the chemical disorder preventing the long-range propagation of magnons. While this dispersionless gapped excitation is consistent with the excitations seen in fragmented neodymium pyrochlores, the spin ice structure factor cannot be observed in the DCS data in either the inelastic data or the elastic, suggesting that the diffuse scattering seen in the DNS data forms the dispersionless gap in the DCS data.

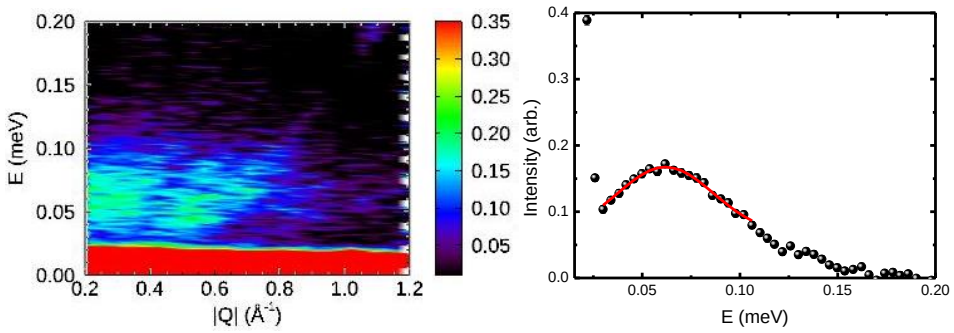

FIGURE 4.8: Inelastic spectroscopy using the DCS at NIST at 100 mK with an incident wavelength of 8 Å, obtained along [H,H,H] integrating over ± 0.25 r.l.u along [-2H,H,H] (left), shown also as a cut along energy using $|Q|$ [0.2,1] (right). The red line is a Gaussian fit to the peak over the region shown.

In order to solve some of the ambiguity of the total moment in the system, the magnitude of the inelastic moment was determined by normalizing to the incoherent scattering of Nd_2ScNbO_7 using the method presented by G. Xu *et al.* [73]. The integration was performed over |Q| 0.4-0.8 $Å^{-1}$ to avoid Bragg contributions, yielding an inelastic moment of 0.26(2) μ_B. A similar result could be obtained by normalizing to a Bragg peak.

4.5 Discussion

Nd_2ScNbO_7 appears to show the fundamental experimental signatures of moment fragmentation, the coexistence of long-range magnetic order and liquid-like scattering. However it is clearly a significant perturbation on the parent compounds $Nd_2Zr_2O_7$ and $Nd_2Hf_2O_7$, as the magnitude of the ordered moment is significantly larger. In O. Benton's description [24] the ordered moment is dependant on a parameter rotation θ such that

$$m_i = g_z \mu_B cos(\theta) m_i^{(\tilde{z})} + g_z \mu_B sin(\theta) m_i^{(\tilde{x})} \tag{4.2}$$

where $m_i^{(\tilde{z})}$ is the ordered Bragg moment and $m_i^{(\tilde{x})}$ comes from the dynamic correlation and m_i is the magnetization on a single site, g_z is the z-component of the Landau g-factor. While this value can be altered by a change in the relative energy of the exchange constants,

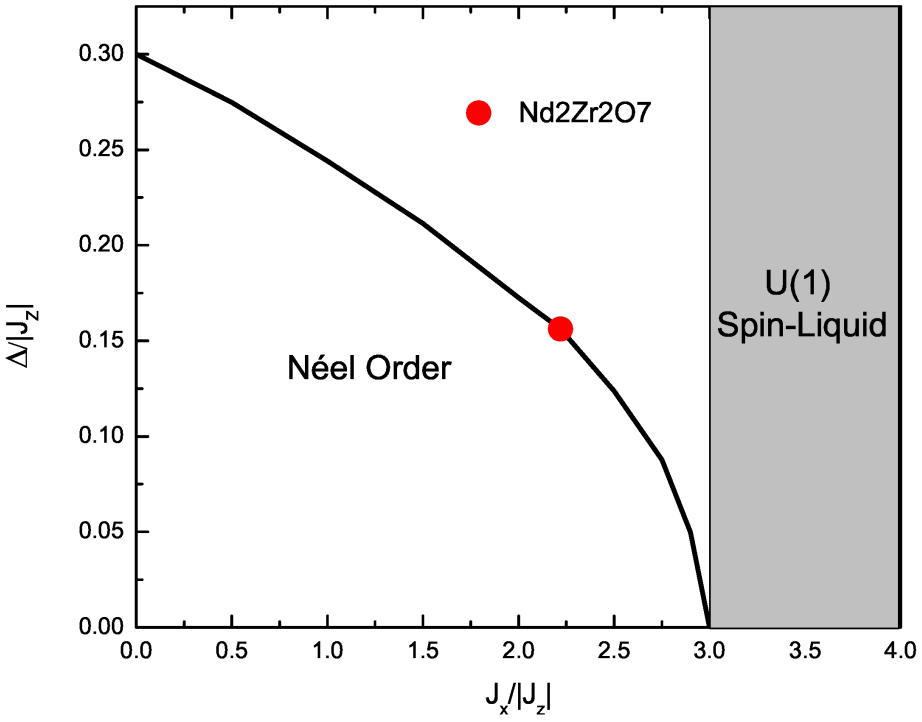

FIGURE 4.9: Phase diagram for dipole-octupole systems on the pyrochlore lattice. J_x and J_z are the exchange constants after a pseudo-spin rotation, and Δ is the band gap. The line indicates the expected gap energy predicted by O. Benton [24]. This phase diagram has been reproduced and modified from O. Benton, 2016 [24].

$$T_{CW} = \frac{1}{2k_B}(\tilde{J}_z cos^2(\theta) + \tilde{J}_x sin^2(\theta)) \tag{4.3}$$

where $\tilde{J}_z$ and $\tilde{J}_x$ are the relevant rotated exchange constants [24], the change would be such that $\tilde{J}_x$ approaches zero. The relationship to the band gap can be described by,

$$\Delta_{flat} = \sqrt{(3|\tilde{J}_z| - \tilde{J}_x)(3|\tilde{J}_z|)} \tag{4.4}$$

where Δ_{flat} is the band gap (Fig. 4.9). As a result the band gap in Nd_2ScNbO_7 would be roughly twice as large as in $Nd_2Zr_2O_7$, when in fact it is slightly smaller then the band gap of $Nd_2Zr_2O_7$ [24]. This implies that the large static moment cannot be described within the typical dipole-octupole simple exchange manifold.

As the conventional description fails to explain the results in Nd_2ScNbO_7, it may better to consider the disorder within the crystal fields. This implies that there is

significant overlap with the ground state allowing symmetries other than dipole-octupole to exist on certain sights, where different neodymium ions can have different symmetries. This would allow for a greater contribution of the magnetic moment towards the static magnetization, although it is difficult to quantify.

If the crystal field analysis is correct and 14(2) % of neodymium ions retain D_3 symmetry while most or all others break the symmetry, only those neodymium ions would retain the dipole-octupole character. Y.P. Huang *et al.* [92] lay out the requirements for dipole-octupole symmetry in the pyrochlore lattice, namely a D_{3d} local environment, an $m_j = \frac{15}{2}, \frac{9}{2}, \frac{3}{2}$ spin system and a crystal field $B_2^0 < 0$. The removal of inversion symmetry does not remove the dipole-octupole constraint where

$$C_3 : \tau^{x,y,z} \Rightarrow \tau^{x,y,z} \tag{4.5}$$

$$\sigma_d : \tau^{x,z} \Rightarrow -\tau^{x,z} \quad \tau^{y} \Rightarrow \tau^{y} \tag{4.6}$$

$$I : \tau^{x,y,z} \Rightarrow \tau^{x,y,z} \tag{4.7}$$

from Chen [92], and consequently

$$C_2 : \tau^{x,z} \Rightarrow -\tau^{x,z} \quad \tau^{y} \Rightarrow \tau^{y} \tag{4.8}$$

as

$$C_2 = I \otimes {}_{\perp}\sigma_d \tag{4.9}$$

causing the symmetry reduction $\Gamma_5^+ \oplus \Gamma_6^+ \Rightarrow \Gamma_5 \oplus \Gamma_6$ under D_3 symmetry. Due to the destruction of dipole-octupole symmetry under other symmetry conditions only the minority of ions retaining D_3 symmetry would still undergo moment fragmentation-like behaviour, while other ions would condense into a conventional Néel state. This is roughly consistent with the magnitude of the inelastic moment where roughly $\frac{1}{2}$ or more of the moment should remain dynamic on the neutron time scale. In this system 10(2) % of the moment remains dynamic, slightly higher than expected of the theoretical result by Benton but consistent with the experimental results of $Nd_2Zr_2O_7$ where roughly $\frac{2}{3}$ of the moment remains dynamic [24], which would yield $\frac{2}{3} \cdot 14(2)$ %, or 9(1) % of the moment remaining dynamic. This symmetry

destruction for most, but not all neodymium ions appears internally consistent with experimental results and provides some explanation for the significantly decreased dynamic moment magnitude in Nd_2ScNbO_7.

4.6 Conclusions

Nd_2ScNbO_7 presents an interesting opportunity to study the effects of chemical disorder on unconventional magnetic states like the moment fragmentation case found in $Nd_2Zr_2O_7$ and $Nd_2Hf_2O_7$. Nd_2ScNbO_7 is directly comparable to its parent compounds, presenting the same underlying ground state, but with significant perturbations. The minority of Nd^{+3} ions (for which a crystal field scheme can be solved) appear to show Ising anisotropy and a dipole-octupole symmetry, similar to the parent compound. However a large portion of Nd^{+3} ions appear to show overlap of the excited states with the ground state crystal field, possibly allowing other anisotropies and symmetries. Despite this Nd_2ScNbO_7 shows the Ising antiferromagnetic Néel state common to other neodymium pyrochlores.

The notable difference between Nd_2ScNbO_7 and its parent compounds is found in the magnitude of the static moment and the absence of dispersing magnons. While the lack of dispersing magnons has not been fully understood, it is likely either due to a vanishingly small intensity, or a very limited lifetime due to the chemical disorder. These magnons are a part of the 'divergence-full' component of fragmentation, and as the Bragg peaks are still present, the 'divergence-full' component still exists within the system. The significant reduction in the dynamic, spin ice-like 'divergence-free' component can be well explained as a result of symmetry breaking evidenced by the crystal field scheme and the charge ice partial order observed in chapter 3. Nd_2ScNbO_7 acts as a good test case for how disorder and symmetry breaking can impact magnetic ground states that are highly reliant on symmetry, destroying fragmentation where symmetry conditions are not met but maintaining fragmentation when the symmetry conditions are retained.

Chapter 5

Palmer Chalker Glass Correlations in Gd_2ScNbO_7

5.1 Introduction

As Gd^{+3} has a half-filled S = $\frac{7}{2}$ shell it has no orbital components to its single ion magnetism, causing it to behave unlike other rare earth systems. This guaranteed Heisenberg anisotropy has resulted in a significant amount of interest in gadolinium pyrochlores. One of the original interests for frustrated magnetism theorists on the pyrochlore lattice was the Heisenberg antiferromagnet on the pyrochlore lattice. The Heisenberg antiferromagnetic pyrochlore was originally thought to have a spin liquid ground state [19, 93]. The original studies only included nearest neighbor interactions, and later work by Palmer and Chalker established that next-nearest neighbor interactions would induce an xy ordered state [20] of the irreducible representation Γ_7 ($\mathbf{k}$ = (000)). Due to the difficulty of performing neutron studies on gadolinium, limited by the high absorption cross section of natural abundance gadolinium isotopes, most of the structural analysis of the magnetic ordering is relatively recent. Experimentally, gadolinium pyrochlores show the formation of liquid like correlations, followed by a Néel order at a lower temperature [94, 95]. While this Néel order sometimes manifests as a Palmer-Chalker Γ_7 ground state, such as in $Gd_2Sn_2O_7$ [96], other ordered states have also been observed. In $Gd_2Ti_2O_7$ a partial order occurs within kagome planes with a non-zero propagation vector [97, 98]. In general all investigated gadolinium pyrochlores with well defined A/B site order, $Gd_2Ti_2O_7$, $Gd_2Sn_2O_7$, $Gd_2Ge_2O_7$, $Gd_2Pt_2O_7$ exhibit some form of Néel order [96, 99, 100] ($Gd_2Pb_2O_7$ is omitted here in

the comparison due to extreme A/B chemical site disorder [101]). The ground state of these pyrochlores is highly sensitive due to the ordering being dictated by next nearest-neighbor interactions which are inherently weak. This sensitive phase space along with the spin liquid behavior that exists over a finite temperature range has driven research into gadolinium pyrochlores.

Here the charge disordered variant of the gadolinium pyrochlore Gd_2ScNbO_7 is investigated. In contrast to the other charge disordered systems, it is not expected that disorder in the crystal field will have a driving impact on the underlying magnetism as this is a spin only system. Deviation from the parent compounds should be driven by a change in the nearest-neighbor exchange induced by the chemical disorder, as longer-range interactions are classical dipole-dipole interactions in large moment systems which are not particularly sensitive to local structural distortions.

In this chapter, polarized neutron diffraction, specific heat, and magnetization experiments and analysis were performed by the author. AC magnetic susceptibility and muon spin relaxation measurements were performed and analyzed by Graeme Luke and James Bear (McMaster). Most of the data presented in this chapter has been reproduced from C. Mauws *et al.*, 2021 [102].

5.2 Methods

DC Magnetometry was obtained on a Quantum Design PPMS VSM, with a base temperature of 1.8 K and applied field of 1000 Oe. Data were collected on a 8.6(1) mg sample of natural abundance Gd_2ScNbO_7 in a polypropylene sample holder. Specific heat measurements were performed on a Quantum Design PPMS with an ^{3}He cryostat, over a temperature range of 0.35 - 40 K using the quasiadiabatic method. La_2ScNbO_7 was used as a phonon standard to isolate the magnetic contribution to the specific heat at low temperatures.

Due to the high neutron absorption cross section of naturally abundant gadolinium (49700 barn at 1.8 Å), neutron scattering experiments on naturally abundant gadolinium are not very feasible. Instead a 1.4564 g sample of $^{160}Gd_2ScNbO_7$ was prepared by the same method described in chapter 3, using Cambridge Isotopes $^{160}Gd_2O_3$ (98.7 % enrichment, 99.9 % purity). This sample can be used for neutron

measurements as ^{160}Gd has a neutron absorption cross section of 0.77 barn at 1.8 Å [81]. Polarized neutron scattering measurements were taken at the DNS spectrometer at FRM II [89] with a wavelength of 4.74 Å over 6 polarization channels, x, y, z with spin-flip and non-spin-flip analysis for each. This allows for full decomposition of the coherent nuclear, incoherent nuclear and magnetic scattering. Issues with the dilution refrigerator limited the base temperature to 300 mK. Measurements were taken at 0.3, 0.5, 0.8, 3.5, and 50 K. Data reduction and polarization decomposition were performed using in house software. Magnetic diffuse scattering was analyzed by using the Reverse Monte Carlo (RMC) method in the SPINVERT software suite [66]. A large box model of 6^3 crystalline Fd$\bar{3}$m unit cells of 10.389 Å was used totaling 3456 spins. Fits were replicated 16 times each with random initial spin orientations. Despite Gd^{+3} being a Heisenberg ion, fits were performed under Heisenberg, xy and Ising anisotropy constraints with a local (111) easy axis to reduce parameterization in the non-Heisenberg cases. A strong nuclear peak near 2.2 Å contaminated the data, so data within this region was excluded from the fit.

5.3 Bulk Properties

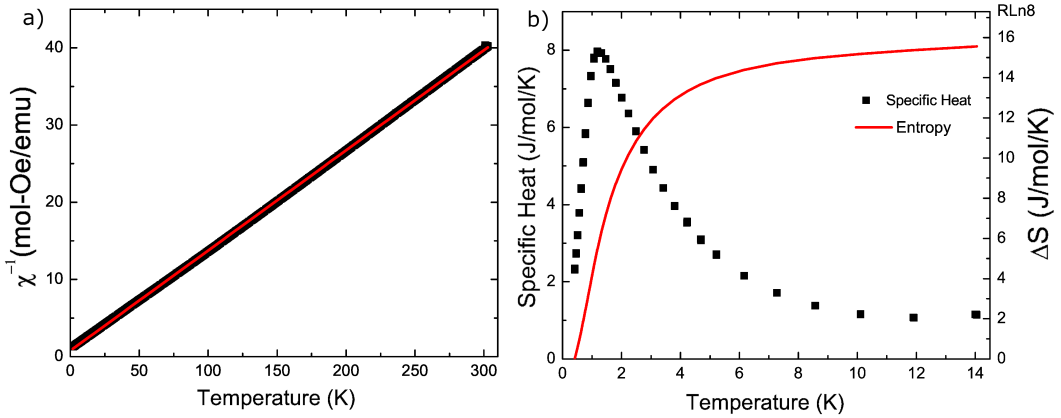

FIGURE 5.1: (a) DC magnetometry from 1.8 to 300 K shown as the inverse susceptibility. The linear fit (red line) is the Curie-Weiss law. (b) Specific heat (square points) data after the phonon subtraction, and corresponds to the entropy release (red line) with the total possible entropy labeled as RLn8 for J = 7/2.

A Curie-Weiss fit to the inverse DC susceptibility (Fig. 5.1) shows a linear trend

over a wide temperature range as is expected of S = $\frac{7}{2}$ Gd^{+3} ion. A Weiss temperature of -3.93(3) K indicates net antiferromagnetic interactions and a free moment of 7.89(1) μ_B is extracted from the Curie constant, similar to the expected value of 7.94 μ_B. Magnetic specific heat measurements (Fig. 5.1) show a broad peak near 1.2 K suggesting the build up of magnetic correlations. The entropy released from this transition over the temperature window 0.35-14 K is 15.56 $J \cdot K^{-1} \cdot mol^{-1}$. The entropy release expected of the full ordering of a S = $\frac{7}{2}$ is R·ln(8) or 17.23 $J \cdot K^{-1} \cdot mol^{-1}$ meaning roughly 90 % of the magnetic entropy is recovered through this transition down to T = 0.35 K. Extrapolating the specific heat to zero linearly does not recover a significant proportion of the remaining entropy, and integrating to higher temperatures becomes dominated by phonons as La_2ScNbO_7 is an imperfect subtraction. While La_2ScNbO_7 behaves as a good phonon standard for the larger cation Ln_2ScNbO_7, this approximation begins to deviate at high temperatures for the smaller cation systems (Gd,Tb, and Dy), as the phonon energies likely change with the shortening bond lengths and unit cell dimensions. Attempts to find a better phonon standard for the small cation systems, such as preparing a Y_2ScNbO_7 pyrochlore have failed so far, so La_2ScNbO_7 is still used as a rough approximation at low temperature where phonon contributions to the heat capacity are mostly insignificant anyways.

5.4 Polarized Neutron Diffraction

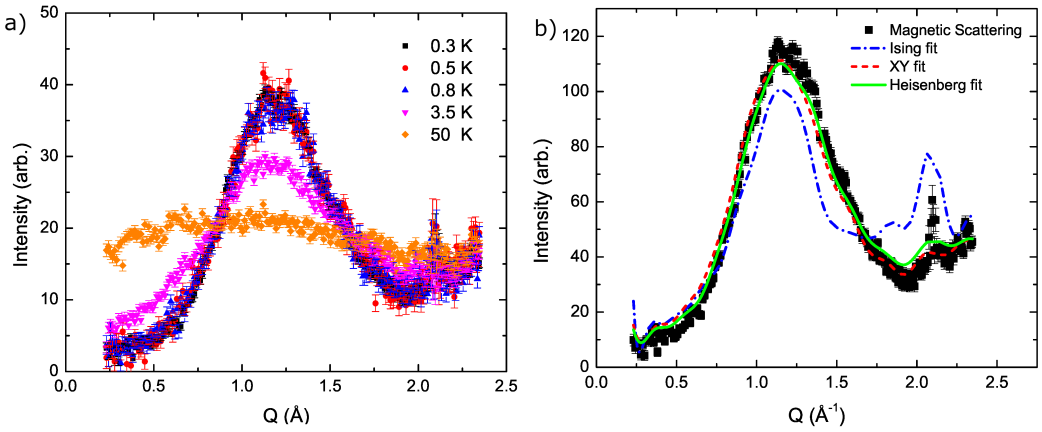

FIGURE 5.2: (a) Polarized magnetic scattering data from the DNS at multiple temperatures. (b) The RMC fits to the 0.3 K data set with fits of varying anisotropy constraints displayed.

Figure 5.2 shows the isolated magnetic scattering by polarization analysis. Correlations in this system can be seen building up by 3.5 K and below and are not observable at 50 K. These correlations saturate by 0.8 K and don't change any further upon cooling. No magnetic Bragg peaks are observed, and the scattering observed is due to short-range correlations. The fact that the scattering is near zero at certain points suggest that the correlations are quite strong which also agrees well with the large entropy extracted. Additionally, the scattering appears to approach zero at |Q| = 0, suggesting that the correlations are antiferromagnetic in nature. RMC analysis is employed to investigate the correlations of the diffuse system. As Gd^{+3} is a Heisenberg ion the Heisenberg fit (Fig. 5.2) should be considered the most meaningful fit to the data. However, the xy and Ising fits can still provide useful information as to whether the more restrictive fits are capable of fitting the data at all. Clearly the Ising data is insufficient to fit the data, showing a large peak near 2.2 Å whether or not that spurious data near 2.2 Å were removed from the RMC fit. The xy data on the other hand, do an excellent job of fitting the data, similar to the Heisenberg fit which has an additional parameter dimension. This suggests that the spins either entirely or predominately lie in the xy plane which is similar to the Palmer-Chalker ground state.

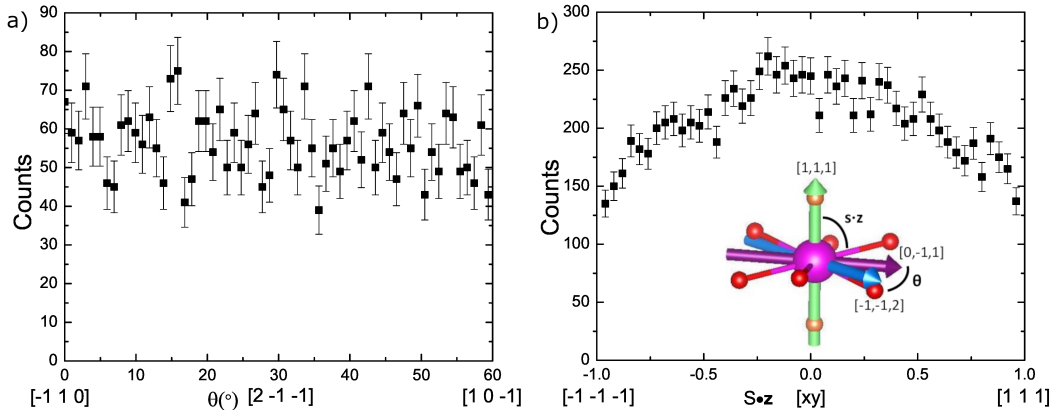

FIGURE 5.3: (a) Histogram of the angular configuration of the spins projected onto the xy plane with 6-fold folding from the Heisenberg RMC fit. (b) Histogram of the spin angular deviation from the xy plane in the Heisenberg RMC fit. Important directions are labeled for clarity. The insert shows vectors along important directions from the Gd^{+3} site, orange oxygens are O_{8b}, red oxygens are O_{48f}. The relevant quantities, $\mathbf{s}\cdot\mathbf{z}$ and θ, are labeled.

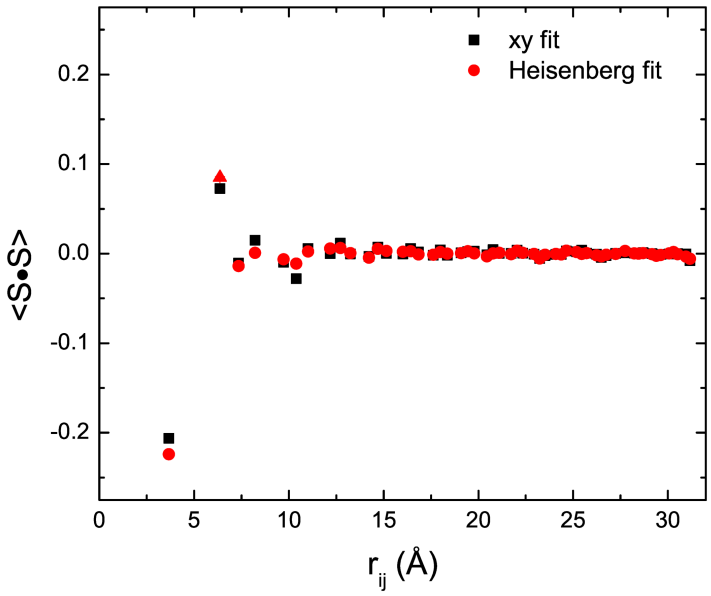

FIGURE 5.4: Average spin-spin correlations extracted from RMC fits as a function of spin distance, for the Heisenberg and xy planar symmetries. Negative values represent antiferromagnetic correlations.

The Heisenberg fit was further analyzed to extract the distribution of spin orientations and the correlations between spins. Figure 5.3 shows the distribution of spins when projected onto the xy plane (θ) and when projected onto the z axis (s·z). The spins have no apparent orientational preference within the xy plane, they do however have a strong preference towards aligning within the xy plane. The data can be well described constraining the moments entirely to the xy plane (Fig. 5.2). Spins orientating within the xy plane is consistent with other gadolinium pyrochlores. However, under the Γ_7 Palmer-Chalker state the spins should align along the (-HH0) directions within the xy plane.

Additionally the correlation magnitudes may be extracted from the RMC results for both the xy and Heisenberg fits (Fig. 5.4). The value $< \vec{S} \cdot \vec{S} >$ represents the average dot product of spins i,j with distance r_{ij} between spins, where a positive value indicates net ferromagnetic orientations and negative, antiferromagnetic. For a fully $\mathbf{k}$ = (000) ordered system on the pyrochlore lattice the maximum value of $< \vec{S} \cdot \vec{S} >$ should be 0.33, and correlations should persist out to high r. In Gd_2ScNbO_7 the nearest neighbor correlations (3.6 Å) are strongly antiferromagnetic, with correlations strongly falling off in magnitude. A correlation length can be fit to $| < \vec{S} \cdot \vec{S} > |$ with an exponential decay, giving an estimated correlation length of 2.1(1) Å for the

Heisenberg fit, less than the nearest neighbor length, suggesting that these should be considered nearest-neighbor correlations.

A caveat is required in interpreting RMC results. In order not to settle into a false minimum a random term is introduced allowing 'bad' spin movements to occur with a variable probability. As a result, RMC results will systematically overestimate the level of disorder [66] both in terms of the local distribution of spins in the case of preferred order and in the correlation values. The correlation length of 2.1(1) Å and maximal correlation value of -0.22(2) should be considered lower bound estimates.

5.5 AC Magnetic Susceptibility and Muon Spin Relaxation

While the structural data is enough to establish that the system is in a disordered state, it does not give any information on the dynamics present. The dynamics probes of AC magnetic susceptibility and muon spin relaxation (μSR) are presented in Mauws *et al.*, 2021 [102]. The data presented here were obtained by the group of Graeme Luke (McMaster), as such only a brief description will be given.

AC magnetic susceptibility shows a frequency dependant peak near 0.8 K (Fig. 5.5, (a)). A peak in χ'' shows spin processes with a relaxation time corresponding to frequency^{-1}, although it does not necessarily imply a thermodynamic transition [103, 104]. A Mydosh parameter, $\phi = \frac{\Delta T_{SG}}{T_{SG} log\omega}$ [105] is a parameter that describes the magnitude of the frequency dependence and is commonly used as a qualitative method of identifying spin glasses (Fig 5.5, (c)) [103]. The Mydosh parameter for Gd_2ScNbO_7 is 0.020(1), near the upper limit but consistent with values expected for spin glasses [106]. Additionally, this Mydosh parameter is significantly too high for most ferromagnets and too low for superparamagnets.

Muon spin relaxation is a dynamics probe that implants polarized muons into a sample and measures the asymmetry of the beta decay products [107]. The asymmetry is defined as,

$$A(t) = \frac{P_f - P_b}{P_f + P_b} \tag{5.1}$$

where P_f is the signal of the forward detector, which the muons are initially polarized towards and P_b is the signal of the back detector, which the muons are initially polarized away from. Once muons are imbedded into the sample they will precess around

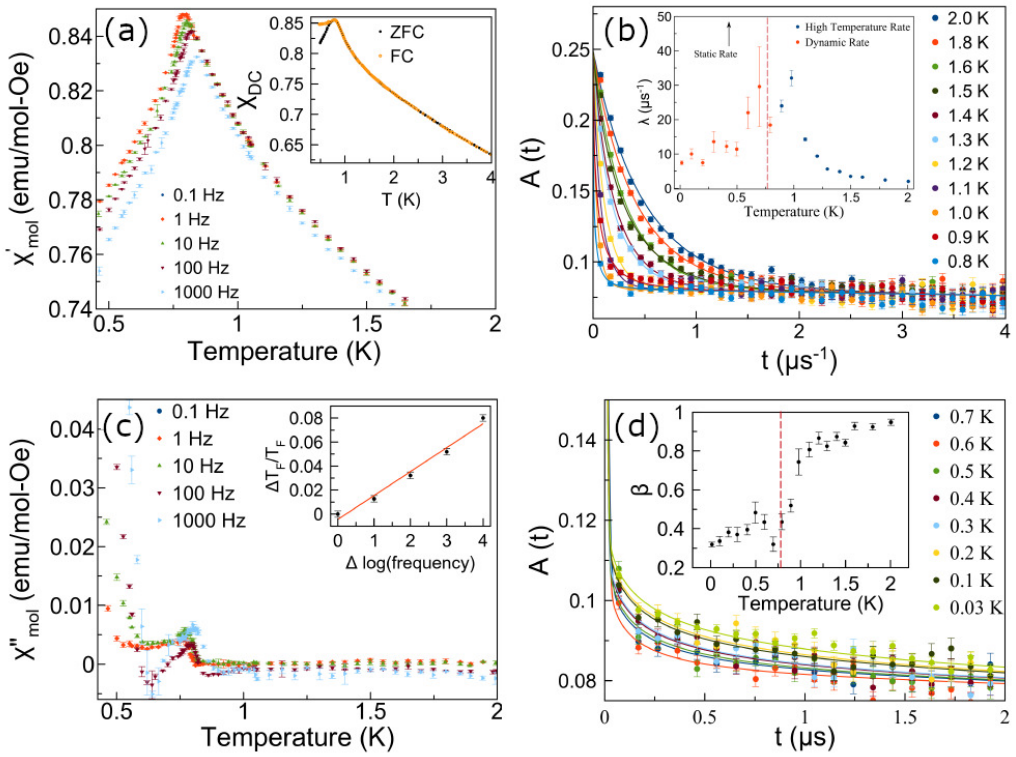

FIGURE 5.5: Dynamics measurements of Gd_2ScNbO_7. (a) The real component of the magnetic susceptibility. (insert) DC magnetometry of the freezing transition, cooled in zero field (ZFC) and cooled in a 100 Oe field (FC) with measurements taken in a 100 Oe applied field. (b) The asymmetry function of the muon spin relaxation data fit to streched exponentials above the freezing temperature. (insert) The relaxation rate extracted from the fits in the paramagnetic regime (blue) and the frozen regime (orange). The frozen regime is split into static and dynamic components, with the static rate out of frame. (c) The imaginary component of the magnetic susceptibility. (insert) A plot of the temperature-frequency shift, from which a Mydosh parameter is extracted. (d) The asymmetry function of the muon spin relaxation data below the freezing temperature, fit to streched exponentials. (insert) A plot of the stretching parameter β through the spin freezing.

their local internal field. In a well-ordered system, this can lead to an oscillation of the asymmetry. In a poorly ordered system, this will lead to a dephasing of the muon precession, the rate of which can be tracked.

Here the relaxation of the muon asymmetry is fit to a stretched exponential decay (Fig. 5.5, (b,d)),

$$A(t) = A_0[\frac{1}{3}e^{-(\lambda_D t)^\beta} + \frac{2}{3}e^{-(\lambda_S t)^\beta}] + A_{bkg}e^{-\lambda_{bkg}t} \tag{5.2}$$

where λ is the relaxation of the dynamics component (D), static component (S) or

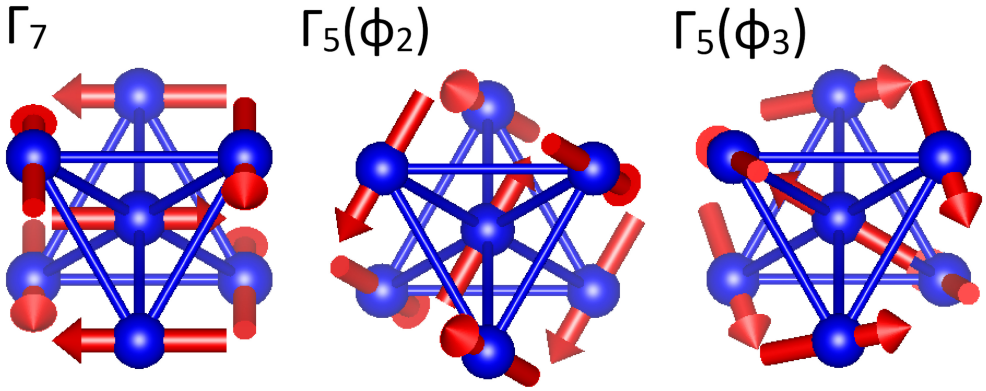

FIGURE 5.6: Local spin orientations for the Γ_7, Γ_5 (Φ_2) and Γ_5 (Φ_3) magnetic structures, which represent the possible **k** =(000) antiferromagnetic states with xy ordering. For reference, the (111) axis is into the page, the central vector of ϕ_2 is pointing in a (-211) equivalent direction and the central vector of ϕ_3 is pointing in an (0-11) equivalent direction. The Γ_7 structure is known as the Palmer-Chalker structure.

background (bkg), β is the stretching exponent, t is time and A is the muon asymmetry. Above the freezing temperature λ_D and λ_S are equivalent, and is just given as λ (Fig. 5.5, (b,d).

Above the transition temperature the zero-field asymmetry shows an increasing relaxation rate. Upon cooling through the transition near 0.8 K the relaxation splits into a fast (Dynamic, D) and slow (Static, S) component with relaxation rates λ_D and λ_S with a ratio of $\frac{1}{3}$ of the moment participating in λ_D which is typical of a frozen state (Fig. 5.5, (b)). This fraction is due to the portion of the muon that lies parallel to the local field. From here the dynamic rate monotonically decreases and the static rate plateaus, which is typical of μSR experiments on rare earth systems [108]. This decoupling of spins into a static and dynamic component suggests that the spins have become static on the μSR time scale. Additionally, when a magnetic field is applied up to 2 T, no phase transition is observed with the freezing temperature shifting up to 0.9 K.

The μSR results are consistent with spin glass behaviour and importantly do not indicate the existence of any long range order phase transition down to 20 mK or up to 2 T. These results are consistent with results on other spin-glass pyrochlores such as $Y_2Mo_2O_7$ [109, 110].

5.6 Discussion

In the parent gadolinium compounds $Gd_2B_2O_7$ (B = Ti, Sn, Pb, Ge, Pt) there is a broad specific heat anomaly similar to what is observed in Gd_2ScNbO_7 followed by a first order phase transition at lower temperatures, which is not observed in Gd_2ScNbO_7. Instead Gd_2ScNbO_7 shows a missing entropy of roughly 10 % of the fully ordered entropy down to 0.35 K. Additionally dilution fridge μSR measurements show no additional ordering transitions down to 20 mK. The long range ordering does change between the $Gd_2B_2O_7$ gadolinium systems, the **k** = (000) Palmer-Chalker state (Fig. 5.6) shows this ordered state for $Gd_2Sn_2O_7$. However, there is also $Gd_2Ti_2O_7$ which shows a **k** = $(\frac{1}{2}\frac{1}{2}\frac{1}{2})$ propagation vector ordering for $\frac{3}{4}$ of the gadolinium ions where the remaining moment remains disordered [25]. In this case the moments do order into an xy framework as well.

It is best to compare Gd_2ScNbO_7 to the intermediate liquid regime that exists in $Gd_2Sn_2O_7$ [111] which has also been analyzed by RMC and direct Monte Carlo methods. In the disordered regime at 1.1 K the $Gd_2Sn_2O_7$ moments also show a strong preference to align within the xy plane, and the RMC gives a similar although underestimated values compared to the Monte Carlo results. The only significant distinction that can be seen is in the correlation function $< \vec{S} \cdot \vec{S} >$. The nearest neighbor correlations in Gd_2ScNbO_7 are -0.22(2) and -0.25 in $Gd_2Sn_2O_7$, which are reasonably similar. There are qualitative differences at further neighbor correlations, where the second (6.6 Å) and third (7.4 Å) nearest neighbor correlations are 0.085(1) and -0.014(1) in Gd_2ScNbO_7 and 0.04 and 0.0125 in $Gd_2Sn_2O_7$ respectively, with Gd_2ScNbO_7 showing antiferromagnetic correlations at the third nearest neighbor instead of ferromagnetic.

The reported correlation length of Gd_2ScNbO_7 is 2.1(1) Å, smaller than a single bond length. However, this fit yields an isotropic correlation length while the correlations are anisotropic, effectively giving an average. In $Gd_2Sn_2O_7$, the correlations along the bonding directions are the strongest with alternating antiferromagnetic, and ferromagnetic correlations similar to a 1-dimensional chain of antiferromagnetically correlated spins. Here however, the correlations along the chains for the first two neighbors are both antiferromagnetic, and so a description using antiferromagnetic

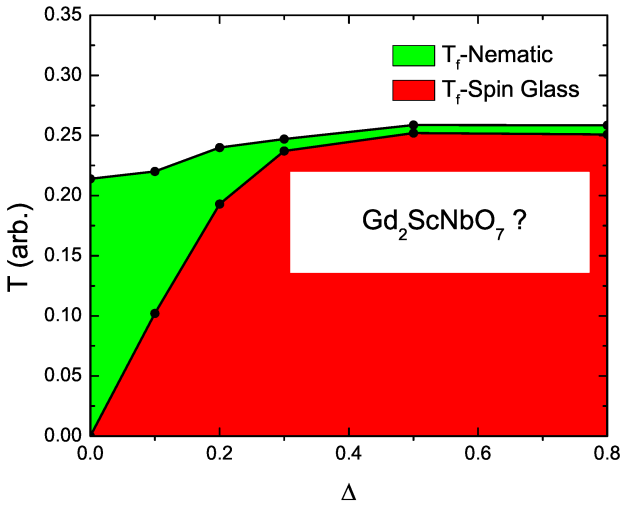

FIGURE 5.7: Phase diagram of the bond-disordered pyrochlore Heisenberg antiferromagnet. This diagram only considers nearest-neighbor coupling (J_1) with $J_2 = 0$. Δ is the magnitude of random bond disorder. This phase diagram has been modified from the work presented by H. Shinaoda *et al.* [112].

spin chains is insufficient to describe Gd_2ScNbO_7, whereas the second nearest neighbor correlations about the kagome hexagons formed by the A-site are much stronger. It may be that Gd_2ScNbO_7 shows correlated hexagonal rings with little correlation between them.

What Gd_2ScNbO_7 provides is a clear example of quenched magnetic disorder as a result of bond disorder. Unlike the other Ln_2ScNbO_7 pyrochlores discussed in this thesis, there is no crystal field disorder here to complicate the causal factors in any observed disorder. The disorder that is frozen into Gd_2ScNbO_7 is likely caused by local distortions of bond lengths that give a distribution of exchange interactions for various Gd^{+3} ions. This has been explored theoretically for bond-disordered Heisenberg antiferromagnets [112, 113]. It has also been realized in some systems like $Y_2Mo_2O_7$ and the doped spinel $Zn_{1-x}Cd_xCr_2O_4$ [114–116]. Work presented by H. Shinaoda *et al.* [112] discusses the pyrochlore system and provides a phase diagram showing the onset of spin glass behaviour with an increasing disorder parameter Δ, where delta provides a range of possible exchange values (J) such that $J \in [< J > -\Delta, < J > +\Delta]$ where $< J >$ is the average exchange value (Fig. 5.7). In the case with only nearest-neighbor exchange any finite value of Δ introduces a spin glass phase at low temperature, with a spin nematic phase existing at higher temperatures for $\Delta < 0.3$. It is difficult to know where Gd_2ScNbO_7 resides on this

phase diagram, but the theory is consistent with our results. Although it should be noted that calculations were performed with antiferromagnetic next-nearest-neighbor interactions (J_2) which introduces a long-range ordered phase at finite amounts of disorder. Based on the results here the next-nearest-neighbor correlations are ferromagnetic, which may imply a ferromagnetic J_2, which does not appear to have been studied theoretically. It would be interesting to compare to the results of those calculations.

5.7 Conclusions

From the magnetic structural data, Gd_2ScNbO_7 shows short-range structural correlation, with an emergent xy spin orientation. Although this seems to approach the predictions of a Heisenberg antiferromagnet on the pyrochlore lattice, long-range order with the spins aligned in the xy plane is precluded by the presence of chemical disorder. This disorder is not due to the overlap of excited crystal electric field causing mixed anisotropies due to the half-filled shell present in Gd^{+3}. It is likely due to a variance in the local exchange interactions experienced by the Gd^{+3} ions. The dipolar interaction is dominant at longer ranges as expected of the long-range interaction, evidenced by the ferromagnetic longer range correlations observed in contrast to $Gd_2Sn_2O_7$. These xy antiferromagnetic nearest neighbor interactions appear to form Palmer-Chalker like clusters (Fig. 5.6, Γ_7).

The system does not achieve long-range order down to 20 mK as evidenced by μSR measurements, which alongside AC susceptibility measurements show Gd_2ScNbO_7 as a glass with quenched disorder. An absence of change in correlations between 0.8 K and 0.3 K supports this. At short range, Gd_2ScNbO_7 shows Palmer-Chalker correlations with long-range paramagnetic correlations facilitated by a glass quenching.

Gd_2ScNbO_7 provides an interesting case among the Ln_2ScNbO_7 pyrochlores, as the crystal field disorder that is prevalent among the others is not a concern here as Gd^{+3} is a spin-only system. As such the exchange disorder, $J \in [< J > -\Delta, < J > +\Delta]$ is isolated from the crystal field disorder. This exchange disorder is sufficient to prevent the long-range order that appears in other $Gd_2B_2O_7$ (B = Sn, Ti) systems, instead freezing into a ground state similar to the liquid-like regimes present in the

parent $Gd_2B_2O_7$ compounds. This does support the idea that bond-disorder is not a significant contribution to the deviations of Nd_2ScNbO_7 from its parent compounds (Chapter 4), as the system appears well ordered, as opposed to Gd_2ScNbO_7 which quenches into a glassy ground state.

Chapter 6

Absence of Spin Ice Behaviour in Dy_2ScNbO_7

6.1 Introduction

Dysprosium pyrochlores have been extensively studied in frustrated magnetism. For example, $Dy_2Ti_2O_7$ is the prototypical classical spin ice, presenting a Kramers doublet Ising crystal field, and an exceptionally large moment of 10 μ_B that causes the spin interactions to be dominated by ferromagnetic dipole-dipole interactions [117, 118]. The consistency of this behaviour results in the dysprosium pyrochlores ($Dy_2Ti_2O_7$ [119], $Dy_2Sn_2O_7$ [48, 120], $Dy_2Ge_2O_7$ [120], $Dy_2Pt_2O_7$ [121]) all showing a similar classical spin ice ground state, where only the freezing temperature changes slightly due to shifts in lattice constants altering the dipole-dipole interaction and the small antiferromagnetic exchange interaction [122].

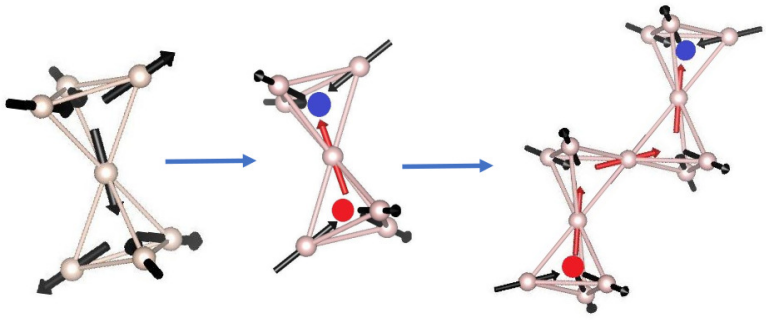

FIGURE 6.1: This graphic shows the spin ice configuration (left), alongside the formation of fractionalized defects (middle) and how these defects propagate freely (right). Red spins indicate flipped spins. Red and Blue dots indicate the fractionalized defect tetrahedra of opposite 'magnetic charge'.

The classical spin-ice ground state contains Ising spins on each tetrahedron with an Ising axis that points towards the centres of the two corner-sharing tetrahedra. A net ferromagnetic dipole-dipole interaction causes ferromagnetic coupling of the classical spins yielding a 'two-in', 'two-out' configuration on each tetrahedron, which is the largest ferromagnetic correlation available to the spins in the nearest-neighbor sphere that holds to the local Ising spin anisotropies (Fig. 6.1). These ordered tetrahedra remain frustrated and quench into a disordered state unless cooled exceptionally slowly [123]. This classical spin ice ground state has fractional excitations that act as magnetic monopole quasiparticles. This occurs by a single spin flip which creates two defect tetrahedra of 'three-out', 'one-in' and 'three-in', 'one-out' monopoles and anti-monopoles which can propagate apart and can only be destroyed by annihilating with their respective anti-quasiparticle [124–126] (Fig. 6.1). In Dy_2ScNbO_7 we investigate a surprising departure from spin ice behaviour. Previous bulk property measurements on Dy_2ScNbO_7 have been reported by X. Ke *et al.* [48], which tentatively report spin ice-like behaviour in Dy_2ScNbO_7 based on a residual entropy that is near but above the spin ice entropy. Here we show that Dy_2ScNbO_7 shows no spin ice behaviour due to a destruction of the single ion anisotropy necessary for classical spin ice.

The work in this chapter has been performed by the author with the exception of; the synthesis of the $^{160}Dy_2ScNbO_7$ sample which was performed by Megan Rutherford, the collection of the CEF data which was performed remotely with the help of Adam Aczel, the collection of the He-3 component of the specific heat data which was performed remotely by Quantum Design. It should be noted that some in-field magnetic work and dynamics will be discussed that results from collaborative work with Megan Rutherford and are reported in the thesis [127].

6.2 Methods

DC magnetic susceptibility was performed on a Quantum Design PPMS with a vibrating sample magnetometer using 6.6(1) mg of powder Dy_2ScNbO_7, the magnetization curve was obtained on a 23.75(1) mg sample at 1.9 K. Specific heat measurements were performed on a Quantum Design PPMS in a He-3 and He cryostat with data

overlapped. Measurements were performed by the quasiadiabatic method, using 11.1(1) mg of powder sample.

Inelastic neutron scattering measurements were performed on the ARCS spectrometer (ORNL) [128]. All neutron measurements were performed on 1.2485 g of powder $^{160}Dy_2ScNbO_7$ (the sample was prepared by conventional methods reported in chapter 3). ^{160}Dy ($^{160}Dy_2O_3$, cambridge isotopes 94.40 % enrichment, 98.0 % purity, metals basis) was used due to its absorption cross section of 56 barn compared to 994 barn at 1.8 Å for natural abundance dysprosium [81] as well as avoiding the resonant line that becomes relevant above 25.3 meV for ^{162}Dy. Measurements at ARCS were performed on the sample mounted in an aluminum can at temperatures of 5 K and 200 K and incident energies of 25, 50 and 150 meV with a resolution of roughly 5 % E_i at the elastic line.

Polarized neutron powder diffraction was performed on the DNS spectrometer [89] at FRM II. The sample was mounted in an annular copper can with sample thickness 0.7 mm (radial) and attached to a dillution refigerator with a base temperature of 120 mK. Measurements were taken at 0.12, 0.3, 0.6, 0.8, 50, 100 K with a wavelength of 4.74 Å, using 6 polarization channels x, y, z for spin-flip and non-spin-flip allowing full polarization decomposition by in house software. The vanadium normalization showed unexplained inconsistencies so an internal normalization by the incoherent scattering was performed instead, with an associated error increase of roughly $\sqrt{2}$. Reverse Monte Carlo (RMC) analysis was performed on the low temperature data using the spinvert software [66], using Ising, xy, and Heisenberg anisotropy constraints. Fits were performed on a 6^3 box of 10.3614 Å unit cells, with anisotropies defined by the local (111) direction for each of the 16 spins in each unit cell, totaling 3456 spins per refinement. Refinements took randomly generated initial spin configurations and each refinement was repeated 8 times with different initial configurations.

6.3 Specific Heat and Magnetization

The inverse magnetic susceptibility data (Fig. 6.2) shows an uncommon feature for rare earth ions, an almost perfect linear Curie-Weiss behaviour between 1.8 and 100 K. Although, despite the spin-orbit interactions the susceptibility is roughly linear in

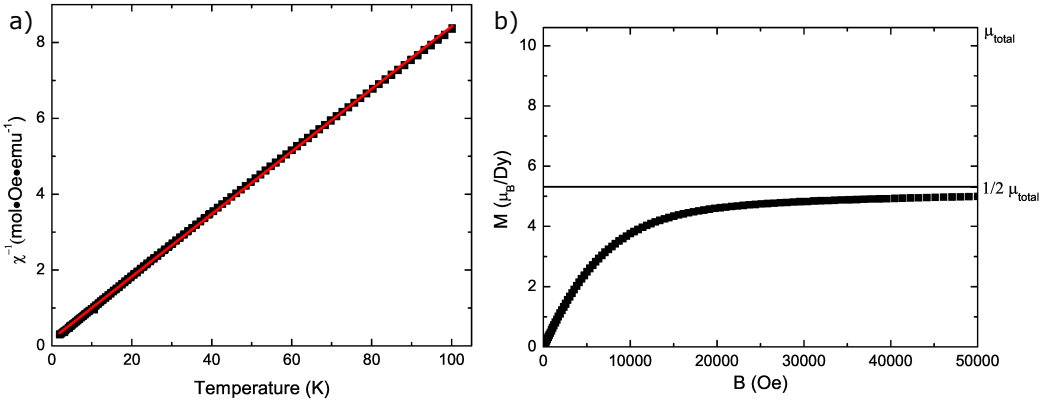

FIGURE 6.2: (a) Inverse magnetic susceptibility in an applied field of 1000 Oe, of powder Dy_2ScNbO_7, including field-cooled and zero-field-cooled data. Red line is a linear Cuire-Weiss fit. (b) Magnetization as a function of applied field at 1.9 K. The expected total moment of Dy^{+3} is labeled as well as the half moment value.

other dysprosium pyrochlores as well [129, 130]. This Curie-Weiss fit yields a moment of 9.89(1) μ_B compared to the 10 μ_B expected of Dy^{+3} at the high temperature limit and a Weiss temperature of -2.16(5) K suggesting antiferromagnetic interactions. The ferromagnetic spin ices also show net antiferromagnetic interaction in their Weiss temperature due to the antiferromagnetic exchange [130]. There is no observable field-cooled, zero-field cooled splitting down to 1.8 K suggesting that the spins remain dynamic on the DC time scale. Magnetization data show magnetic field saturation just below $\frac{1}{2}$ of the total expected moment for Dy^{+3}. A saturation of $\frac{1}{2}\mu_B$ typically indicates a strong anisotropy of either Ising or xy, however if that was the case we would expect the saturation to be closer to $\frac{1}{2}\mu_B$ than is observed, and is more consistent with mixed anisotropy systems, and not consistent with a Heisenberg system [131, 132].

Specific heat measurements are a tell tale sign of spin ice due to the characteristic Pauling entropy that exists [119]. The Pauling entropy, $\frac{R}{2}ln\frac{3}{2}$ (1.69 J·K^{-1}) is a missing entropy from the full $Rln2$ (5.76 J·K^{-1}) entropy due to the macroscopic degeneracy of the spin ice configuration. Figure 6.3 shows the magnetic entropy release after the phonon contributions, approximated by La_2ScNbO_7 are removed, along with the associated entropy. As a lattice subtraction, La_2ScNbO_7 is less applicable to the small cation Dy^{+3} when compared to the larger cation systems, and fails at higher temperature. The upper integration range is limited to 10 K. The entropy released

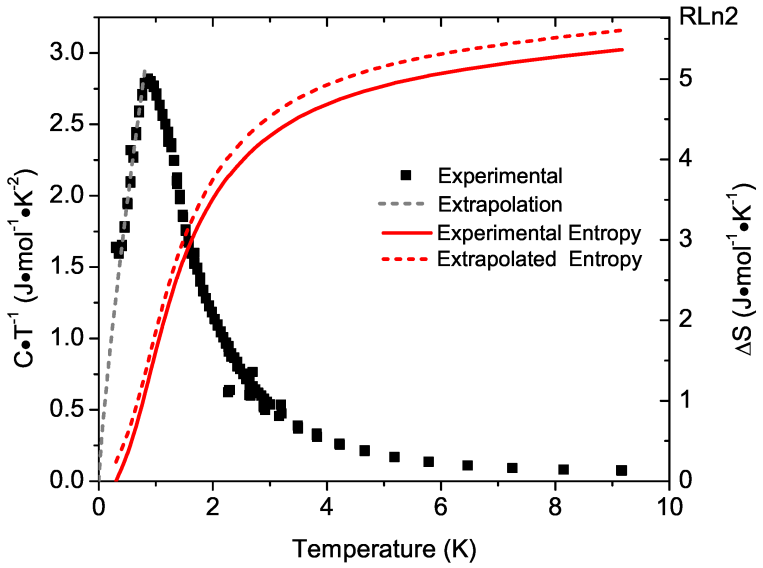

FIGURE 6.3: Magnetic specific heat (black points) of powder Dy_2ScNbO_7 after a phonon correction using La_2ScNbO_7, reported as $\frac{C}{T}$. The grey dashed line is a power-law extrapolation to zero temperature. The red line is the direct integration of the experimental data, and the red dashed line includes the integration of the grey dashed line below the temperature limit.

by Dy_2ScNbO_7 is unambiguously higher than the expected spin ice entropy of 4.07 $J{\cdot}K^{-1}$, which was also observed in previous measurements [48] although we observe an even greater deviation. Extrapolation of the low temperature specific heat is performed by fitting to a scaling law $C = \alpha T^{\gamma}$ which yields $\alpha = 3.42(5)$ and $\gamma = 1.81(3)$, which allow for an analysis of the scaling exponent γ as well as calculation of an extrapolated entropy (Fig. 6.3). The extrapolated entropy does not fully saturate to Rln2, although it comes close enough that systematic error such as the imperfect phonon subtraction could hide saturation. This suggests that the Pauling entropy is not present in Dy_2ScNbO_7. The scaling of $\gamma = 1.81(3)$ seems to exclude both spin glass ($\gamma = 1$) or a gapless three-dimensional antiferromagnet ($\gamma = 3$) [103], suggesting more interesting physics is at play. It may also simply be that this scaling fit is not performed over an appropriate range, or the scaling equation may not have an exponential form.

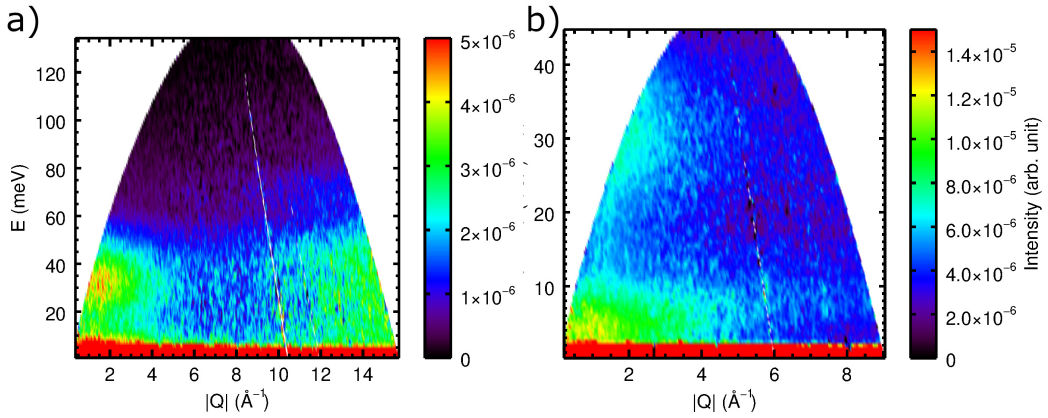

FIGURE 6.4: Inelastic neutron spectroscopy measurements of the crystal electric field from ARCS on Dy_2ScNbO_7 at 5 K using incident energies of (a) 150 meV and (b) 50 meV.

6.4 Crystal Electric Field Spectroscopy

The crystal electic fields of Dy^{+3} ions on the pyrochlore lattice are typically well separated from the ground state crystal field by approximately 21 meV [133]. Figure 6.4 shows the neutron accessible crystal field distibution within Dy_2ScNbO_7, the crystal field excitations are broad in energy due to the chemical disorder, and no discrete peaks associated with high probablility configurations are observed as in Nd_2ScNbO_7 (chapter 4). Of the 7 excited crystal field doublets in the probed range, 3 to 6 of which should be visible to neutrons, only 2 broad excitations are visible. The visible crystal fields are not similar in energy to the parent $Dy_2Ti_2O_7$ [133]. Of particular note is the broad excitation centred near 6 meV, which is not well separated from the ground state, unlike the parent compounds. This has the potential to introduce new crystal field symmetries, although it is interesting that this does not cause the inverse magnetic susceptibility to deviate from a linear behaviour.

To ensure that this low energy excitation is a crystal electric field and not a magnetic excitation figure 6.5 compares the $|Q|$-dependence of the feature to the magnetic form factor of Dy^{+3} showing it is consistent with a crystal field. Additionally both broad excitations are visible at 200 K (not shown), but are heavily smeared due to the population of excited crystal fields, indicating that the low energy feature is in fact a crystal field. There is not sufficient data to approximate the crystal field scheme here.

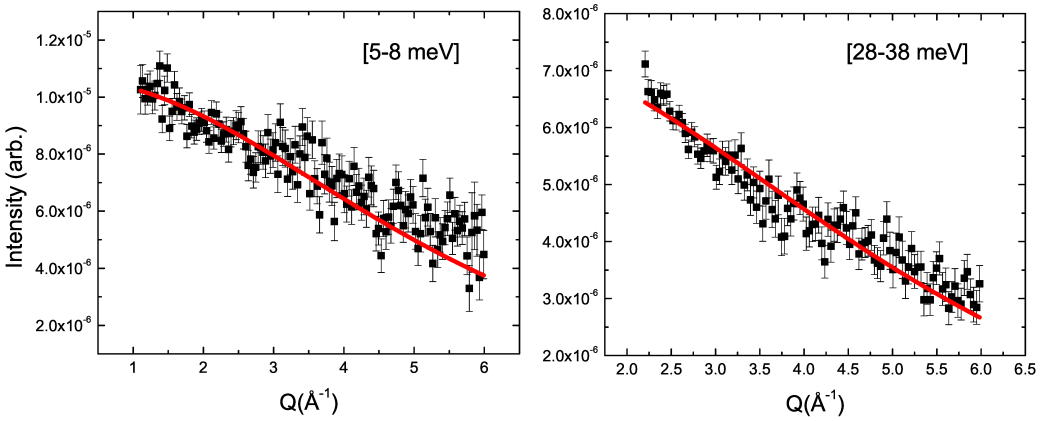

FIGURE 6.5: The Q-dependence of select features in the ARCS inelastic neutron spectroscopy data. Energy integrations are performed over the specified ranges. Red lines are the squared magnetic form factor of Dy^{+3} with an arbitrary multiplicative scaling.

6.5 Magnetic Neutron Diffraction

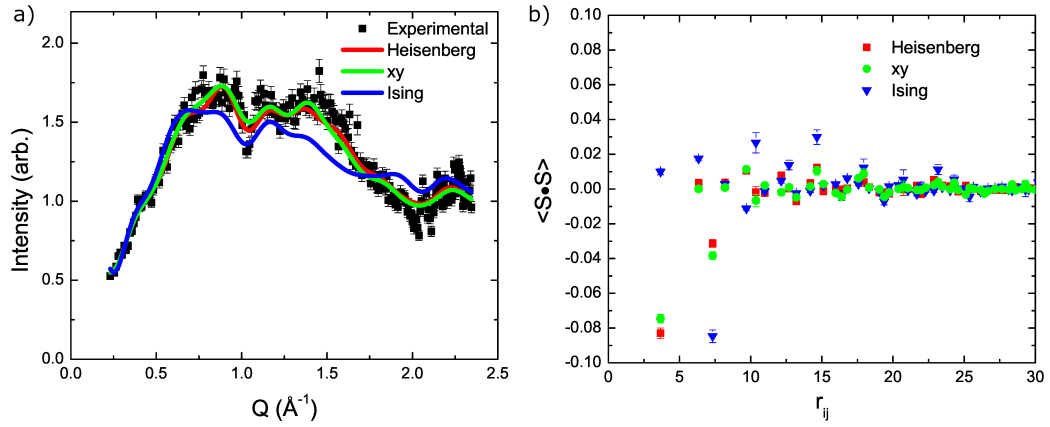

FIGURE 6.6: (a) Magnetic neutron scattering data obtained by polarization decomposition of polarized powder diffraction data from the DNS spectrometer at 120 mK. Lines represent RMC fits with labeled anisotropy constraints. (b) The spin-spin correlation functions of the various RMC fits, r_{ij} indicates the distance between the magnetic ions.

Polarized magnetic neutron powder diffraction is used to isolate the magnetic scattering from Dy^{+3} (Fig. 6.6 (a)). Weak correlations develop by 800 mK and persist down to 120 mK without apparent change. A dead window in temperature in the cryostat set up prevents measurements between 800 mK and 4 K, and high temperature measurements were limited by time. Most of the measurement time was used to increase the statistics of the 120 mK data for RMC refinement. One can immediately observe that the correlations in Dy_2ScNbO_7 are qualitatively different from spin ice

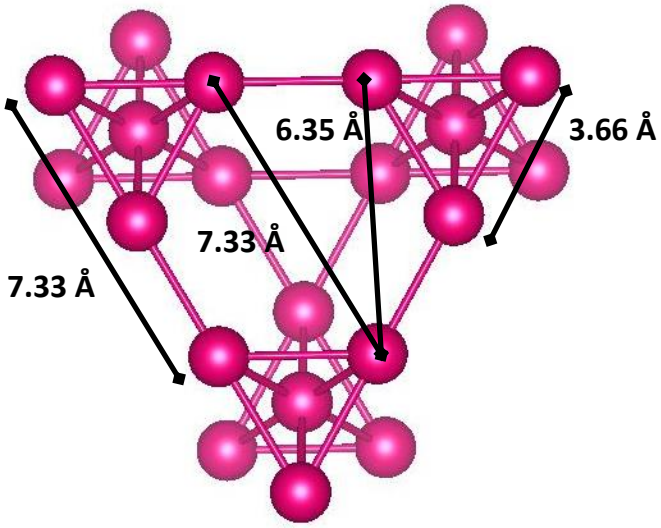

FIGURE 6.7: Graphical representation of the three nearest neighbor coordination spheres of Dy^{+3} ions on the pyrochlore lattice.

powder patterns [134], including a decreasing intensity as |Q| approaches zero, suggesting antiferromagnetic correlations. In general though, the correlation magnitudes are very small with peaks and valleys in the scattering intensity only slighly deviating from the mean, suggesting that most of the spins remain uncorrelated.

Reverse Monte Carlo fitting using multiple constraints shows that the Ising spin constraint is insufficient to describe the data, which would not be the case for spin ice. The xy constraint sufficiently describes the data, although there is no evidence that the spins in this system should have an xy orientation. The Heisenberg case therefore is used to generically describe the system. Figure 6.6 (b) shows the $< \vec{S}_i \cdot \vec{S}_j >$ correlation function, where the Heisenberg correlations should be taken as the most realistic. The nearest neighbor correlations (-0.08) are weakly antiferromagnetic, and remain well below the ordered correlation value of 0.33 for pyrochlores. Next nearest neighbor interaction (around the kagome hexagons, Fig. 6.7) is near zero, however the next next nearest correlations (along bonding directions, and across hexagons, Fig. 6.7) also appear antiferromagnetic. This interaction is comprised of two distinct correlations, and the correlation being antiferromagnetic is unlikely to be consistent with antiferromagnetic correlations along the bonding direction. Instead this likely indicates that there are antiferromagnetic correlations across the hexagons. Fitting $|< \vec{S} \cdot \vec{S} >|$ to an exponential decay yields an average correlation length of 2.3(3) Å,

although similar to the case of Gd_2ScNbO_7 the correlations are highly anisotropic.

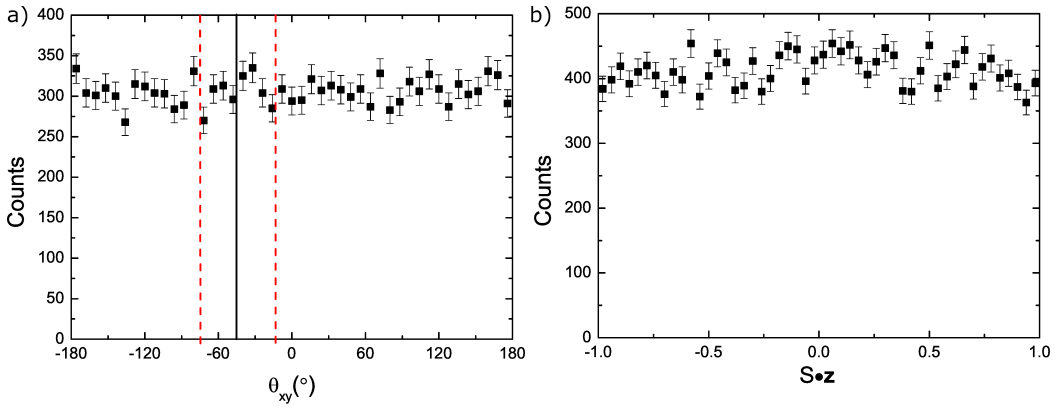

FIGURE 6.8: Histograms of the single ion spin configurations from the Heisenberg RMC fit. (a) For spins projected onto the xy plane, red dashed lines indicate (-110) equivalent directions, and the solid black line indicates one (11-2) equivalent direction, where 6 periodic equivalents of each vector lie within the plane. (b) Component of the moment along the local z, (111) equivalent axis. For a graphic of the dimensions depicted in this histogram refer to figure 5.3.

Although the xy fit appears to fit the data well, this may be just due to a sufficiently large parameter space. To investigate the local spin anisotropy the results of the Heisenberg RMC fit, a histogram of the local spin configurations is shown in Figure 6.8. It is apparent that no statistically significant spin orientational preferences are present within Dy_2ScNbO_7, which is unusual for an ion that typically retains a strong Ising anisotropy on the pyrochlore lattice.

6.6 Dynamics

Dynamics measurements on Dy_2ScNbO_7 have primarily been performed by Megan Rutherford [127] so this section will be limited to a discussion of the results.

AC magnetic susceptibility and muon spin relaxation have been performed to probe the dynamics of Dy_2ScNbO_7. The muon spin relaxation shows very quick relaxation of the muon polarization at all temperatures, likely due to the dynamics induced by the low lying crystal fields in Dy_2ScNbO_7 such that there are no unique local environments for the muons to experience. The AC susceptibility is more useful, as a strong frequency dependant shift in the real component of the susceptibility is observed. Although the frequency range currently observed is limited between 1-500 Hz, the response appears to be linear for $\frac{\Delta T_{SG}}{T_{SG}} \propto log(\omega)$, with a proportionality

constant of roughly $\phi = 0.08$. This linear response is typical of spin glasses, with a typical proportionality constant, called a Mydosh parameter, in the range of 0.06-0.08 for insulating spin glasses [106]. It is worth noting that these values are also not uncommon for spin ice systems, as they are effectively spin glasses as well (over the appropriate temperature ranges). This Mydosh parameter does deviate from other pyrochlore spin glasses like $Mn_2Sb_2O_7$ [105] and Gd_2ScNbO_7, which have Mydosh parameters closer to conducting spin glasses like Ni-doped Mn [106]. Dy_2ScNbO_7 actually appears to be a more canonical insulating spin glass like $(FeMg)Cl_2$ [106]. One might speculate that this is related to the isotropic behaviour of the dysprosium spins unlike the emergent anisotropic xy gadolinium spins.

6.7 Discussion

It is apparent that Dy_2ScNbO_7 is not a spin ice. This is the primary surprising result of this work, as all Dy and Ho pyrochlores up until this work have been classical spin ices due to the dominant interactions being classical dipole-dipole interactions, which are not as sensitive to small perturbations in bonding lengths as exchange interactions are. This lack of spin ice behaviour is evidenced by the lack of the characteristic Pauling entropy [119], as well as the magnetic neutron scattering data, which is qualitatively different from spin ice [134]. Fits to the magnetic diffuse scattering show spins with no preferred orientation, whereas the conventional spin ice systems are purely Ising, and attempts to fit the system to an Ising model cannot represent the data, and yield meaningless results.

To explain these results, magnetization and crystal electric field data are needed. Although the crystal fields are too diffuse to be easily fit, it can be seen that there are low lying crystal fields below 10 meV that is not observed in other dysprosium systems where the excitations are typically well separated from the ground state. In Dy_2ScNbO_7 there is no apparent gap between the ground state crystal fields and the excited states. This could introduce alternative anisotropies onto dysprosium ions creating a heterogeneous local environment of dysprosium ions. This heterogeneous environment of anisotropies and underlying J values for exchange, alongside local displacements altering the exchange values can feasibly lead to the spin-glass system

that is observed. Although the bulk indications do not suggest that the system is particularly frustrated, a Weiss temperature of -2.16(5) K is not dramatically different from the spin-freezing temperature of roughly 1 K. The released entropy also appears to approach the expected ordering entropy, although this is tough to quantify as the population of crystal fields above the ground state doublet could also be a significant contribution. the magnetic entropy never properly reaches zero, and increases at higher temperatures, either due to phonon standard mismatch or the population of excited crystal fields.

It is unlikely that the Dy^{+3} system is truly anisotropic as the RMC analysis would nominally suggest. Instead there is likely a distribution of anisotropies among the Dy^{+3} ions, that average out to an apparently anisotropic system. A distribution of anisotropies, and weak, short-range correlation lengths is reminiscent of an anisotropy driven spin glass. While spin glasses are typically driven by a distribution of exchange interactions, they can also be driven by a distribution of anisotropies [135–137]. This has been studied for ferromagnets with random anisotropies in a crystalline system [135, 136]. Given that Gd_2ScNbO_7 is also shows glass like correlation, due to a distribution of exchange interaction, a similar distribution of exchange interactions should exist in Dy_2ScNbO_7. A combination of exchange disorder and anisotropy disorder is likely present in Dy_2ScNbO_7. This additional frustrating affect, compared to Gd_2ScNbO_7 may explain why the nearest-neighbor correlation value for Dy_2ScNbO_7 (0.08) is significantly lower than Gd_2ScNO_7 (0.2).

6.8 Conclusions

The charge disordered pyrochlore Dy_2ScNbO_7 has been investigated by magnetization, and specific heat measurements, as well as polarized neutron diffraction and neutron crystal field spectroscopy. The built in disorder discussed in chapter 3 dramatically changes the crystal field environment of the dysprosium ions compared to the parent pyrochlores and gives rise to a heterogeneous environment of magnetic anisotropies, moments and exchange interactions. The low lying crystal field excitations appear to overlap with typically isolated ground state doublet leading to the heterogeneous environment. This magnetic system becomes more akin to a system of

disordered magnetic ions, that result in a glassy magnetic ground state. The liquid or glass like structure is observed by reverse Monte Carlo analysis of the diffuse scattering data, and shows that the net exchange profile of the system is not that of simple nearest-neighbor interactions, but likely shows strong antiferromagnetic correlations across the hexagons of magnetic ions (Fig. 6.7). The spin-glass ordering is consistent with dynamics work that has been performed by collaborators. Additionally the combination of an average isotropic spin distribution and lower correlation magnitude suggest that both anisotropy disorder and exchange disorder are underlying causes of the magnetic frustration. To elaborate on one of the important goals of this works, determining the impact of disorder on magnetically frustrated ground states, Dy_2ScNbO_7 provides evidence that ion disorder is very capable of altering underyling electronic ground states, at least in the weakly coupled electronic states of rare earths. In this case the chemical disorder directly leads to a glassy ground state. This is especially relevant as this glassy disorder can easily be mistaken for liquid-like scattering originating from more exotic interactions. These mistaken experimental results is an example of so-called mimicry, a term also used to explain the behaviour of $YbMgGaO_4$ [11]. $YbMgGaO_4$ is another charge disordered system, which attracted attention as a potential spin liquid. Although in that case, orientational disorder of the local charge environment, not overlaping crystal field ground states causes the mimicry.

Chapter 7

Ising Antiferromagnetism in $Sm_2Ti_2O_7$

7.1 Introduction

Among the most chemically well behaved rare earth pyrochlores are the $Ln_2Ti_2O_7$ titanates. The highly ordered structure, along with relatively simple crystal growths of these systems compared to other non-magnetic B-sites, have caused them to be the best studied series of rare earth pyrochlores. Stable on the A-site, are the lanthanides rare earths ranging from Sm^{+3} to Lu^{+3} [15]. They show a robust set of interesting ground states as described in chapter 1. $Sm_2Ti_2O_2$ was the last member of this series to receive detailed experimental analysis. Some bulk property measurements had been performed prior to the work presented here, although they did not probe beneath the Néel temperature due to temperature limitations within the measurements [138].

$Sm_2Ti_2O_7$ was a desirable system to study due to the small moment of 0.43 μ_B for Sm^{+3}. While many of the rare earths in the titanate series such as Ho^{+3} and Dy^{+3} have large semi-classical spins, the relatively small value of S ($\frac{5}{2}$), L (5), and J ($\frac{5}{2}$) opened the opportunity to study a more quantum system, specifically one expected to have Ising anisotropy, which no other small moment titanate possessed. $Sm_2Ti_2O_7$ also contains the nominal requirements for dipole-octupole moment fragmentation, with net antiferromagnetic interactions [138] and a predicted $m_j = \pm\frac{3}{2}$ ground state.

Since the original publication by Mauws *et. al* [139] additional neutron scattering results on both $Sm_2Ti_2O_7$ and $Sm_2Zr_2O_7$ have been published by Peçanha-Antonio *et al.* [140], which agree with the underlying ground state presented here with some

differences in the reported crystal field ground state which will be discussed.

In this work the author performed: the neutron triple axis experiment and data analysis, the polarized diffraction experiment and data analysis, and the specific heat analysis. Samples were prepared and single crystals grown by Paul Sarte (U of Manitoba) and Haidong Zhou (UT Knoxville). Crystal field measurements and analysis were performed with the help of Gabriele Sala (ORNL) and Paul Sarte. Muon spin relaxation measurements were performed and analyzed by Alannah Hallas (UBC). Heat capacity measurements were collected by Djamel Ziat (U de Sherbrooke). Additionally the author thanks Adam Aczel (ORNL) for help in the moment refinement for $Sm_2Ti_2O_7$. Other neutron spectroscopy measurements on the sample (not shown) were performed by Alannah Hallas, Jonathan Gaudet (McMaster) and Paul Sarte. The majority of the work here is reproduced from Mauws *et al.*, 2018 [139].

7.2 Methods

Polycrystalline samples of $Sm_2Ti_2O_7$ were prepared by the conventional solid state method (Sm_2O_3, Alpha Aesar 99.99 % and TiO_2 99.999 % metals basis), with stoichiometric ratios of reagents. Repeated heatings at 1450 °C with intermediate regrindings were performed until phase pure. A single crystal of $^{154}Sm_2Ti_2O_7$ (Cambridge isotopes, 99.8 % enrichment) was grown by the optical floating zone method under flowing Ar gas and cut into segments of $\sim$3 g.

Polarized neutron diffraction was performed at the D7 spectrometer at the Institute Laue-Langevin (ILL) [64]. The crystal was mounted in the [HHL] plane and mounted in a dilution refrigerator using a copper mount. Polarization channel z-spin-flip and z-non-spinflip were utilized for measurements, with the polarization normal to the diffraction plane. Measurements were taken at 50 mK and 4 K to act as a background. Single crystal neutron diffraction was also performed at the HB-1A triple axis spectrometer [141] at the Oak Ridge National Laboratory to obtain an order parameter, and refine a more accurate moment. The same sample was mounted in a dilution refrigerator on the same copper mount. Accessible Bragg peaks (18 unique peaks, 34 total) were scanned using ϕ scans (rocking curves), at base temperature

40 mK up to 600 mK. An order parameter was obtained by scanning the (220) peak using 10 mK steps from 40 mK to 600 mK.

Neutron CEF spectroscopy was performed on ARCS [128] at the ORNL, with the crystal mounted on an aluminum wire to minimize background contribution, using a CCR cryostat. Measurements were performed at 5 K and 200 K using E_i = 150 meV and 60 meV.

Specific heat measurements were performed using the quasi-adiabatic technique, the heater and thermometer were directly attached to a single crystal of $Sm_2Ti_2O_7$ which was weakly linked to a dilution refrigerator. Muon spin relaxation measurements were performed at the M15 beam line at TRIUMF. A sample of $Sm_2Ti_2O_7$ was cut into slices with faces aligned along the (001) direction, and fixed to a dilution refrigerator. Incident muons were polarized antiparallel to their momentum, towards the (001) face.

7.3 Crystal Electric field

As a J = $\frac{5}{2}$ ion Sm^{+3} will have three CEF doublets in its ground state multiplet. Figure 7.1 shows the inelastic spectrum of $Sm_2Ti_2O_7$ with an E_i of 60 meV, with minimized background contributions. Due to the small moment phonon interference is significant but a CEF can be seen at 16.3 meV. This excitation was also observed by Raman spectroscopy by Singh *et al.* [138]. They also claim to observe several other excitations, more than should exist in the ground state multiplet, some of which are too weak in intensity to properly identify and some of which are likely virtual excitations. Additionally previous work by Malkin *et al.* [26] made an attempt to fit the crystal field parameters from magnetic susceptibility, and predict crystal fields at 21.4 and 26.4 meV neither of which are observable in the neutron CEF data.

Identifying the second excited crystal field is significantly more difficult, due to a lower intensity, and a more limited Q-range, leading to more phonon interference. We considered excitations visible at 29, 70, and 100 meV. For this analysis the temperature difference between 5 K and 200 K were used to fit the Q-dependence of the excitations, as the population of the 16.3 meV mode reduces the intensity of excited crystal fields at higher temperatures (Fig. 7.2). The mode at 70 meV was identified as the second

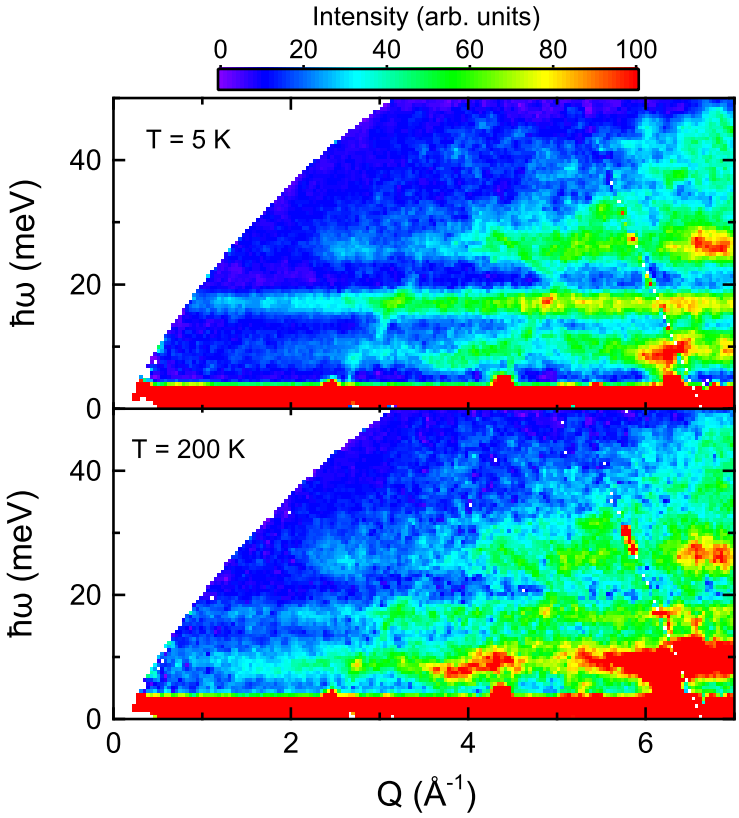

FIGURE 7.1: $S(Q,\hbar\omega)$ for $Sm_2Ti_2O_7$ measured at ARCS with $E_i = 60$ meV: The data set clearly shows a crystal field transition present at 16.3 meV. The other two excitations at 10 meV and 27 meV are phonon levels of Sm^{3+} that have been observed in other rare earth pyrochlores (e. g. Ref. [133]). Moreover, due to the exotic form factor of Sm^{3+}, the intensity of this crystal field excitation decreases at low Q, which is well captured by our MC simulation.

CEF of the ground state multiplet. Figure 7.3 shows the Q-dependence of the excited states after a temperature difference, compared to the form factor of Sm^{+3}. It is worth noting that these crystal fields are difficult to identify both due to the small moment of Sm^{+3} as well as the unusual form factor of Sm^{+3} (Fig. 7.3) which does not decrease monotonically unlike most form factors.

With the intensity of these modes identified the CEF of $Sm_2Ti_2O_7$ is calculated under the weak field approximation, where only the ground state J = $\frac{5}{2}$ multiplet is considered. This allows for a reduction in CEF parameters, as the full crystal field manifold of six parameters could not be fit to this limited data set. The Stevens' parameters of B_{20} = 3.397 meV, B_{40} = 0.123 meV, and $B_{43} = 8.28{\cdot}10^{-8}$ meV provide a solution to the crystal field that is non-unique, but are consistent with our CEF excitations (Fig. 7.2). The results are reported in table 7.1 yielding a ground state of

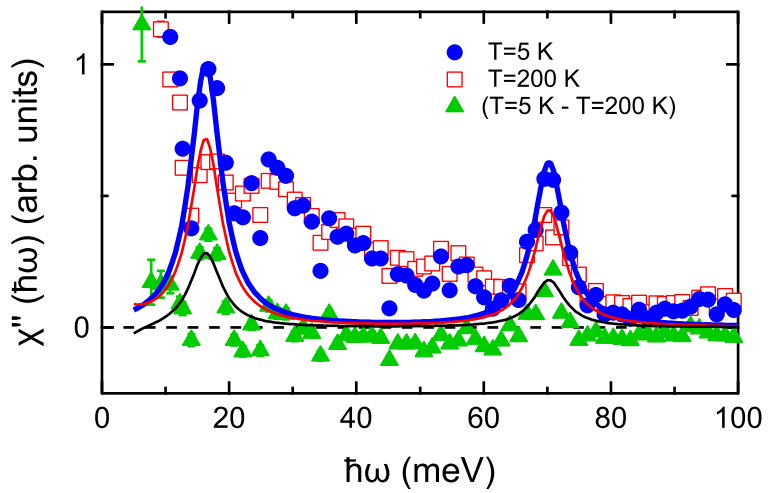

FIGURE 7.2: Comparison of $\chi''(\hbar\omega)$ at 5 K and 200 K. Individual Q cuts in the $E_i = 150$ meV data set ($1 \leq Q \leq 5$ Å^{-1}), corrected for the Sm absorption, are plotted as a function of temperature. The comparison with our fit (solid lines) shows an excellent agreement between our CEF model and the INS data at both temperatures. The green markers and black line represent the temperature difference between the two data sets and our fit respectively.

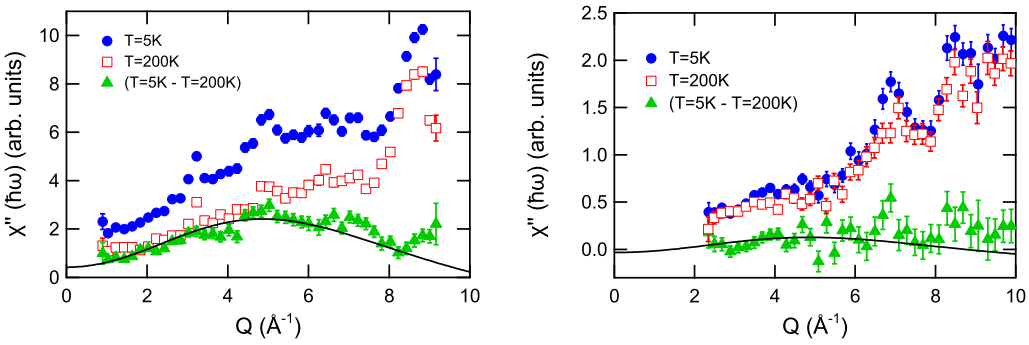

FIGURE 7.3: Energy cuts for $Sm_2Ti_2O_7$. (a) Data set at $E_i = 60$ meV showing the Q-dependence of the first CEF transition. (b) Data set at $E_i = 150$ meV showing the Q-dependence of the second CEF transition. The Q-dependence of the crystal field transitions measured at ARCS show a remarkable agreement with the Sm^{3+} magnetic form factor. The fitting function consisted of a constant background, a small Q^2 term to account for a phonon background, and a multiplicative term times the square of the magnetic form factor. The Landé g-factor for Sm was fixed to 2/7.

TABLE 7.1: Crystal field analysis results for $Sm_2Ti_2O_7$ calculated within a point charge model and fitting the two experimentally-determined energy levels.

E_{obs} (meV)	E_{fit} (meV)	-5/2	-3/2	-1/2	1/2	3/2	5/2
0.0	0.0	0	0	0	0	-1	0
0.0	0.0	0	1	0	0	0	0
16.3	16.52	0	0	1	0	0	0
16.3	16.52	0	0	0	-1	0	0
70.0	70.28	0	0	0	0	0	1
70.0	70.28	1	0	0	0	0	0

$m_j = \pm\frac{3}{2}$. It is worth noting that this crystal field has been artificially simplified to the simplest solution that reproduces the neutron data and may not be a complete solution, as it is not unique. It is telling however that no temperature dependent virtual excitation at 200 K is observed between 16.3 meV and 70.0 meV which would appear at 53.7 meV. This is explained by this crystal field manifold as no coupling will exist between $\pm\frac{1}{2}$ and $\pm\frac{5}{2}$ as a neutron can only induce a transition of $\pm\frac{1}{2}$. This crystal field configuration yields a ground state moment of 0.43 μ_B.

It is worth noting that the CEF parameters here were calculated in the Stevens' formalism, these are related to the Wybourne parameters by a parameter dependant scaling factor. For self-consistency in the Wybourne formalism this equates to B_0^2 = 164.6 meV, B_0^4 = 393.41 meV, and B_3^4 = $1.12{\cdot}10^{-5}$ meV. These are related by $B_{kq} = \lambda_{kq}\theta_k B_q^k$ where B_{kq} is the in the Stevens' formalism and B_q^k is in the Wybourne formalism, λ_{kq} and θ_k are tabulated in Boothroyd (1990-2014) and Hutchings (1964) respectively [68, 70].

7.4 Néel Ordering

To search for a magnetic transition in $Sm_2Ti_2O_7$, muon spin relaxation and specific heat measurements were employed. Figure 7.4 (a) shows the asymmetry relaxation of the μSR data in zero field, indicating the rate of muon dephasing is increasing at lower temperatures, suggesting that the system leaves the uniform field of a paramagnetic state. The asymmetry was well-fit by a Gaussian relaxation function, $A(t) = A_0 e^{-\lambda t^2}$, where λ is the relaxation rate. The relaxation rate increase monotonically down to 0.1 K before plateauing, this plateau is typical of rare earth systems probed by μSR, and can exist in systems with long-range order. More telling of a long-range

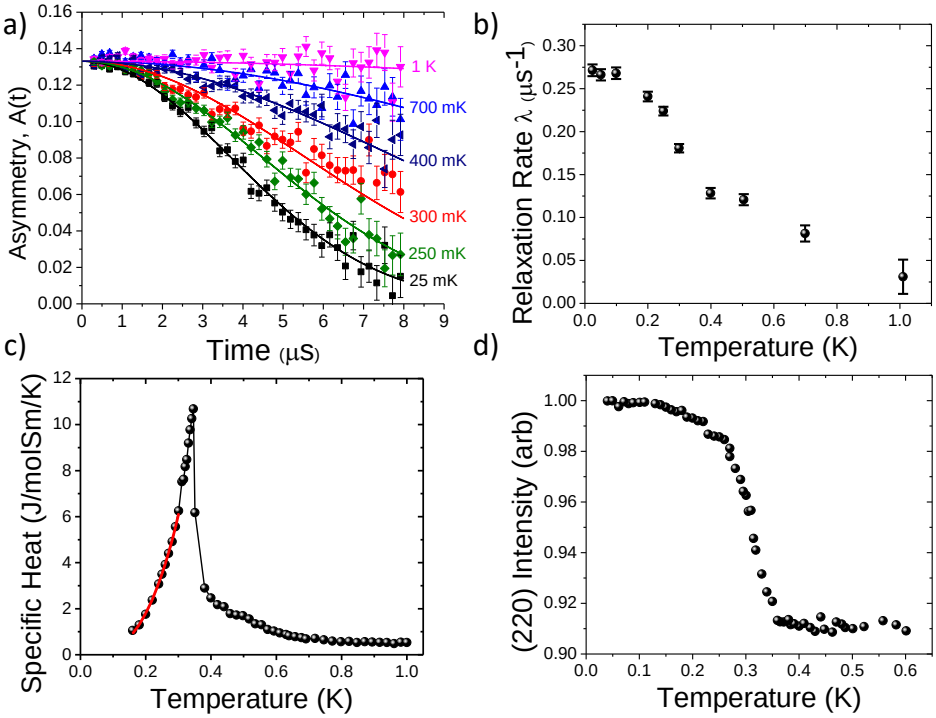

FIGURE 7.4: (a) The asymmetry of the zero-field muon spin polarization for $Sm_2Ti_2O_7$ evolves significantly between 1 K and 25 mK. The asymmetry spectra are well fit at all temperatures by a Gaussian relaxation function. (b) The fitted μSR relaxation rate as a function of temperature. (c) Specific heat measurements on $Sm_2Ti_2O_7$ reveal a magnetic ordering transition at $T_N = 0.35$ K. The red curve is a T^3 power law that was used to extract the magnetic entropy down to 0 K. (d) The intensity of the (220) magnetic Bragg reflection as a function of temperature also reveals an ordering transition around $T_N = 0.35$ K.

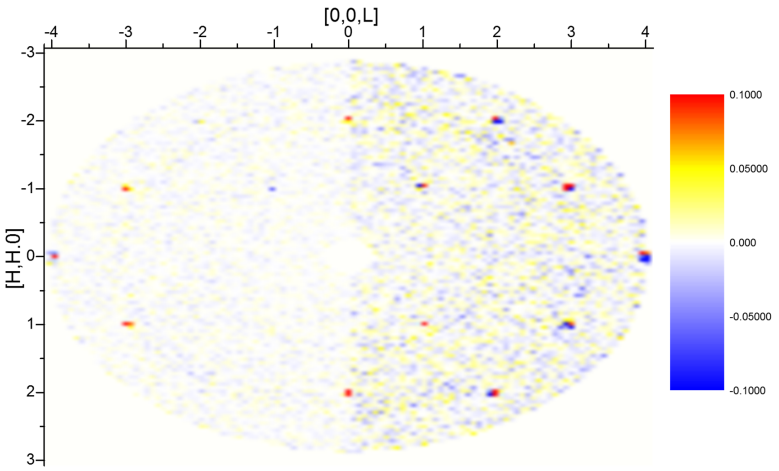

FIGURE 7.5: D7 diffraction data in the (HHL) plane, shown as 50 mK - 4 K temperature-difference plots. The left side shows the spin flip channel, while the right side presents the total scattering. Data has been smoothed for ease of viewing, as peak widths were less than the instrumental Q-resolution ($\sim 1°$ in 2θ).

TABLE 7.2: Peak intensities of the magnetic Bragg reflections in $Sm_2Ti_2O_7$ compared against the calculated values for all of the possible k = (0,0,0) ordered structures for the 16*c* Wyckoff position in the $Fd\bar{3}m$ pyrochlore lattice. The best agreement is obtained with the Γ_3 all-in all-out structure.

	(111)	(002)	(222)	(220)	(113)	(004)
Observed	0	0	0	1.0±0.4	0.78±0.27	0
Γ_3 $\phi(1)$	0	0	0	1.00	0.66	0
Γ_5 $\phi(2,3)$	0.88	0	0	1	0.35	0
Γ_7 $\phi(4,5,6)$	0.52	1.00	0.44	0.11	0	0
Γ_9 $\phi(7,9,11)$	0.69	1.00	0.44	0.43	0.51	0.67
Γ_9 $\phi(8,10,12)$	0.06	0.37	0.16	0.44	0.76	1.00

order transition are the specific heat measurements (Fig. 7.4 (c)). Here a lambda-like anomaly can be seen at T_N = 0.35 K, with a discontinuity associated with a first-order phase transition. The red line in Figure 7.4 (c) is a fit to a T^3 power law and can be seen to have a reasonable agreement, which is consistent with the population of antiferromagnetic spinwaves in a three-dimensional antiferromagnet at the small temperature limit. Integrating the entropy from $\frac{C}{T}$ up to 1 K yields an entropy of 0.84·Rln2, which is slightly short of the expected Rln2, but that may be due to the difficulty of empirically integrating a discontinuous transition.

The polarized diffuse scattering spectrometer D7 in diffraction mode was used to look for long-range and short-range correlations. Figure 7.5 shows the z-spin-flip and z-non-spin-flip scattering as a difference above and below the Néel temperature. Magnetic Bragg peaks are clearly observable in the spin-flip scattering at the (002) and (113) positions, as no nuclear scattering is permitted in the spin flip scattering. These peaks are indicative of the Γ_3 all-in, all-out structure. While D7 is an ideal instrument in looking for diffuse magnetic scattering, none is observed in $Sm_2Ti_2O_7$. This may be due to a lack of diffuse scattering or an extremely small signal.

In order to refine the magnetic structure the HB-1A spectrometer was used in an elastic configuration. Figure 7.4 (d) shows the order parameter from tracking the (220) peak, although the statistics and point spacing were not sufficient to reliably fit a critical exponent. The integrated intensities from the HB-1A data were used to fit the Γ_3 irreducible representation in FullProf Suite, yielding a moment of 0.44(7) μ_B, in agreement with the total crystal field moment of 0.43 μ_B. The form factor used for this determination was input manually into FullProf Suite as it used the spin-only j_0

function. Instead the first two radial components of the analytically approximated magnetic form factors are used such that F(Q) = <j_0(Q)> + $\frac{2-g}{g}$<j_2(Q)> under the dipole approximation [142].

7.5 Discussion

$Sm_2Ti_2O_7$ appears to be a simple antiferromagnet with T_N = 0.36 K by all experimental measures, although a couple of discrepancies remain. Attempts at measuring the magnetic inelastic response of $Sm_2Ti_2O_7$ with experiment performed on the Cold Neutron Chopper Spectrometer (ORNL) by collaborators did not observe any signal, likely due to the vanishingly small moment of Sm^{+3} and the difficulty of performing neutron experiments on these systems. As such the dipole-octupole crystal field ground state of $\pm\frac{3}{2}$ could still allow for moment fragmentation similar to what is seen in Nd^{+3} pyrochlores. Although the agreement of the refined moment and the crystal field moment would mean that the inelastic signature would likely be vanishingly small.

An extensive work on $Sm_2Ti_2O_7$ and $Sm_2Sn_2O_7$ that also uses ^{154}Sm for neutron scattering was published by Peçanha-Antonio *et al.* [140] after the initial publication of this work. The most significant conclusions of this works agree well with our results, including the observation of the Γ_3 ground state, but it is worth considering the discrepancies. Analysis of rare eath zirconates including $Sm_2Zr_2O_7$ is also presented in the thesis of J. Xu [143] that will be considered.

Between all three works there are discrepancies in the crystal field scheme. A limitation of this work was the limited energy range used to probe the higher energy muliplets $^6H_{\frac{7}{2}}$ above 100 meV. Both of the other papers observe and fit additional crystal field levels near 130, 155, 170, 183 meV associated with this J = $\frac{7}{2}$ multiplet. As such the other papers incorporate the full six parameter description of the crystal field that includes higher multiplet terms in the ground state doublet. Normally contributions from the higher multiplets are negligible in pyrochlores but the small contributions presented in [140] do cause a significant reduction of the crystal field moment to 0.16 μ_B for $Sm_2Ti_2O_7$ and 0.27 μ_B for $Sm_2Sn_2O_7$. The work by Xu yields a moment for $Sm_2Zr_2O_7$ yields a moment of 0.39 μ_B. These discrepancies between

various samarium pyrochlores are likely too large to be described by cation size change. The issue that remains is that these works do not observe the second excited state in the ground state manifold that we observe at 70 meV, and report excitations at 29.7 meV for $Sm_2Ti_2O_7$ or 35.7 meV for $Sm_2Zr_2O_7$ with very small but still possibly detectable intensities. The crystal field parameters presented in these studies are more similar to other rare earth pyrochlores than what are presented here, and do likely provide a better description of the crystal field, but still contain significant differences. The question of the total crystal field moment still remains somewhat ambiguous. The work by Peçanha-Antonio *et al.* were not able to measure a moment for $Sm_2Ti_2O_7$ due to the small signal. As such the crystal field moment still need to be rationalized with the diffraction moment, which should be less ambiguous than the crystal field fits given the limited data available in those measurements.

7.6 Conclusions

The magnetic ground state of the final member of the rare earth titanate pyrochlore series has been investigated. While the system does show dipole-octupole symmetry, no signatures of moment fragmentation is noted within experimental error. An Ising antiferromagnetic ground state is observed, with a Néel temperature of 0.36 K, and an ordered moment of 0.44(7) μ_B. Some discrepancies remain in the crystal field, but there is agreement that the ground state is predominantly $\pm\frac{3}{2}$. While a measurement and fit of the spin-wave spectrum would be ideal to derive an underlying Hamiltonian, this measurement may be prohibitively difficult due to the small moment of Sm^{+3} on the pyrochlore lattice.

Chapter 8

Conclusions and Future Directions

8.1 Conclusion on the Charge Disordered Pyrochlores

The goal of working on the Ln_2ScNbO_7 pyrochlores was in part to investigate a new series of magnetically frustrated materials to look for new exotic physics. Additionally, investigating the differences between the magnetic ground states of these materials from their parent compounds was used to determine the affects that chemical disorder played on magnetically frustrated ground states. Chemical disorder is relevant to a number of systems that appear to have exotic magnetic ground states. The Ln_2ScNbO_7 systems act as an extreme example of how disorder on non-magnetic sites can impact the ground states of magnetic systems, at least for rare earth frustrated magnets. In fact, the results here seem to indicate that the low energy crystal fields of rare earth systems are the most dramatically impacted component of rare earth magnetism when non-magnetic disorder is introduced. So, while these results likely can't be extended to light transition metal systems, they are relevant for systems with dominant spin-orbit coupling. In general, the chemical disorder leads to a heterogenous environment of electronic ground states in the rare earth ions. A ground state that relies on the built-in anisotropy or symmetry of the electronic ground states is sensitive to non-magnetic disorder. Gd_2ScNbO_7 acts as a nice control for this statement as the lack of spin orbit coupling leaves the system qualitatively similar to the parent $Gd_2B_2O_7$ systems.

The structure of the Ln_2ScNbO_7 pyrochlores has been investigated by diffraction and total scattering techniques using X-rays and neutrons (Chapter 3). Powder samples of Ln_2ScNbO_7 (Ln = La, Pr, Nd, Sm, Gd, Tb, Dy) have been prepared,

although in the large cation samples a $LnNb_{1-x}Sc_xO_{4-x}$ impurity remains, that can be removed by floating zone crystal growth. Single crystals of Ln = Pr, Nd, Sm, Gd, Tb, Dy have been prepared by the floating zone method, although crystal masses for Ln = Tb, and Dy are limited in size ($\sim$ 200 mg) due to instability in the crystal growths. Neutron diffraction was used to provide better contrast to oxygens and B-site cations for Rietveld refinement. Neutron measurements show significant anisotropic displacement factors, with the (Nb,Sc) site showing the largest distortions, extending to the 48f oxygens and the lanthanide site. To better understand the short-range correlations of Sc and Nb ions, pair distribution analysis of neutron data was utilized. This showed that in the large cation systems Ln = La, Pr, and Nd there are strong nearest-neighbor correlations favouring alternating Sc-Nb pairs. The strength of these correlations seem to approach charge-ice values where each B-site tetrahedron has two Sc and two Nb ions. The smaller cation systems such as Ln = Tb, the correlations appear weaker although this trend is largely inconclusive due to the limited samples used for neutron experiments and the large associated error with the fitting process.

The importance of the disorder towards the magnetic ground state is apparent in all of the systems for which the magnetic ground state was studied. In Nd_2ScNbO_7 the moment fragmentation phenomenon observed in other neodymium pyrochlores is significantly altered. The ratio of the static moment to the dynamic moment is changed from the conventional $\sim$ 50% to $\sim$ 90 %. Additionally, the spin wave spectrum becomes undetectably broad, and the dispersionless gapped excitation becomes nearly isotropic, although the gap energy remains nearly unchanged. These deviations cannot be explained within the typically reported linear spin wave theory of moment fragmentation. Here the deviation is tentatively explained by the breaking of dipole-octupole symmetry normally assumed for neodymium pyrochlores. A broad range of crystal field excitations is fit as a sum of a diffuse and discrete components, and the discrete component is fit to a hexagonal crystal field scheme. The discrete excitations do appear to have the dipole-octupole symmetry required for moment fragmentation in these neodymium systems, which may explain why some signatures are still observed. However, the diffuse excitations take up 86(2) % of the spectral weight, and don't appear to be gapped away from the electronic ground state. It is

likely that symmetry breaking from these unquantified crystal fields is responsible for the deviation from moment fragmentation behaviour. In general, the introduction of ion disorder on the magnetic site does partially destroy the moment fragmentation phenomenon that is reliably seen in other neodymium pyrochlores.

A stark difference can be seen in Gd_2ScNbO_7 which does not vary as dramatically from the parent compounds as the other charge disordered systems. As Gd^{+3} is a spin only ion, there should be no significant effect on the electronic ground state of the system by local disorder. The system quenches into a glassy state with spins predominantly orientating in the xy direction. As there is no spin-orbit coupling this xy order is an emergent phenomenon from the spin interactions, that is well known in other gadolinium pyrochlores. Although other gadolinium systems order at some temperature below a liquid-like phase Gd_2ScNbO_7 does not show any long-range ordering transition down to 20 mK. This lack of a secondary transition is likely related to the heterogeneous exchange introduced by the disorder, although there is limited evidence to explain these discrepancies.

Another example of how crystal field disorder affects the underlying magnetic ground states in pyrochlores is in Dy_2ScNbO_7. Instead of the ferromagnetic Ising, spin ice ground state observed in other dysprosium pyrochlores, a glassy ground state with no observable anisotropy and weak net antiferromagnetic correlations is observed. Again, this can be explained by the low-lying broad crystal fields that appear to overlap with the ground state. It is likely that the heterogeneous crystal field environment allows for non-Ising spin states. The distribution of local anisotropies and exchange interactions yields a system with small net antiferromagnetic interactions with an $< S \cdot S >$ of -0.08 and a short correlation length of 2.3(3) Å, lower than the nearest neighbor distance. Although the RMC fitting method likely underestimates these values, they still indicate a system with large amounts of quenched disorder.

An interesting comparison can be made between Dy_2ScNbO_7 and Gd_2ScNbO_7. The lack of orbital contributions in the S = $\frac{7}{2}$ Gd^{+3} implies that the frustrating affects leading to spin quenching are due to exchange disorder. In Dy_2ScNbO_7 this is also likely the case, but in addition to exchange disorder there appears to be an additional frustrating affect of anisotropy disorder. This is evidenced by the lower average correlation magnitude and the on-average isotropic distribution of spins, whereas

Dy^{+3} pyrochlores typically show strong Ising anisotropies. This anisotropy disorder can also cause the system to freeze into a glassy state and may be relevant to other rare earth systems with significant non-magnetic disorder.

8.2 Relevance to Frustrated Rare Earth Magnetism

$Sm_2Ti_2O_7$ was the last member of the rare earth titanate series to be investigated. The compounds of this series have been studied extensively as they presented the first examples of some interesting phenomenon including spin ice and order by disorder mechanisms [144]. $Sm_2Ti_2O_7$ also possessed the correct symmetry to show moment fragmentation behaviour, and due to the small Ising moment, it was also considered a candidate for quantum spin ice behaviour. Here we show that by all measurements performed $Sm_2Ti_2O_7$ is an Ising antiferromagnet, with no observable signatures of moment fragmentation. Due to the exceptionally small moment ($< 0.43\ \mu_B$) of the Sm^{+3} ion in $Sm_2Ti_2O_7$ measurements beyond diffraction are difficult to consider, and the diffraction measurements themselves are somewhat difficult to analyze which has led to a slight controversy over the magnitude of the ordered moments. Although in general there is good agreement on the ground state order of $Sm_2Ti_2O_7$, this has rounded out the rare earth titanate series, as all magnetically relevant members have been studied extensively (even though questions remain about some of the more complicated systems).

Returning to the charge disordered pyrochlores, the results presented here give some insight into disorder in other frustrated systems. The $AA'B_2F_7$ pyrochlores, where B is a 3d transition metal and A, A' are an alkali and alkali earth metal, were mentioned previously as analogous charge disordered pyrochlores, due to the (+1,+2) charge disorder on the non-magnetic A-site. From these results it would seem that the impact of non-magnetic disorder is less significant in transition metal systems with minimal spin-orbit coupling. The influence of broadened crystal fields would not have the same impact on their single ion properties. The only remaining influence is the exchange disorder introduced by the local distortions. As seen in Gd_2ScNbO_7, this can lead to quenched disorder and glass properties, but the short-range picture of the magnetic ground state still appears similar. This matches well with what

has been observed in the $AA'B_2F_7$ pyrochlores [44, 45]. However in systems like $YbMgGaO_4$, a potential spin liquid compound, the crystal field broadening observed [145] may be more relevant to the disordered ground state than the exchange disorder [11]. Although even here the crystal field broadening due to the Ga/Mg site mixing doesn't seem to be as extreme as in the Ln_2ScNbO_7 pyrochlores [145]. Comparing this to Nd_2ScNbO_7 it would be interesting to investigate if there is significant short-range correlations between Ga/Mg, that lead to a less disordered crystal field environment. In fact there has been some work investigating how the structural distortions affect the system using *ab initio* calculations. However, the calculations force a random distribution of Ga and Mg ions which may be nearly periodic on a short length scale [146].

More generally, this work has shown that in rare earth systems exchange disorder induced by chemical disorder is not the only important impact of disorder. The disorder introduced into crystal fields can alter the anisotropy of spin-orbit coupling and alter the g-tensor to a point where there is effectively a heterogeneous environment of magnetic ions. This introduces new problems, where exchange disorder has been modeled in some theoretical work, and the author is not aware of theoretical models that include crystal field disorder in rare earth magnetically frustrated systems. As the major concern of having disorder in a frustrated system is 'mimicry' where a disordered glassy material mimics the experimental signatures of more interesting theoretical models, crystal field disorder models may have to be developed to properly understand frustrated systems with non-magnetic ion disorder, or any disorder that distorts the local ion environment.

8.3 Future Directions

The obvious continuation is the investigation of the magnetic ground states of the other Ln_2ScNbO_7 systems, Ln = Pr, Sm, Tb. A significant amount of work, not presented here, has been performed on these systems already. This work was not reported either due to an incompleteness of the data, or the involvement of external collaboration, such as in the terbium case. The preliminary work on Pr_2ScNbO_7

seems to suggest a non-magnetic singlet ground state with low-lying magnetic excitations, however necessary diffraction measurements have been delayed preventing publication here. Nominally the trend of large ion systems showing more ordered crystal fields than the smaller cations appears to remain true for Ln = Pr and Tb. Publication of these results may better support the conclusions presented here. Analysis of the chemical disorder presented here may be improved as well by a more robust RMC analysis of the total scattering data, this would be aided by single crystal total scattering analysis, but RMC analysis of 3D total scattering data is still quite intensive work.

As discussed, this work has been largely experimental. Collaboration with theory in order to develop models of crystal field disorder would be beneficial. The data could be modeled by anisotropic displacement factors and calculated with point charge calculations. It is worth noting that point charge calculations on rare earth systems can be of limited use and are often qualitatively wrong. More advanced theoretical techniques would be required that take into account local ion configurations. The end goal of this work would be to apply these models to more 'relevant' systems in the literature that are seeing interest due to their apparently exotic physics which has to be disentangled from the disorder-induced effects.

The Ln_2ScNbO_7 systems do still provide interest in and of themselves. Gd_2ScNbO_7 appears to be a fairly unconventional spin glass, with a Mydosh parameter that varies from that expected of an insulating system, along with an emergent spin anisotropy. Investigating the magnetic excitations to see if dispersion relations or a gap are present (neither of which should be by conventional wisdom) could help understand the unorthodox behaviour. Bulk property measurements on gadolinium (and other) systems in a field on crystals aligned to high symmetry directions would be desirable to map out more detailed phase diagrams of these systems. This work is already ongoing for Dy_2ScNbO_7.

The host of Ln_2GaSbO_7 and other charge disordered pyrochlore systems could be investigated to see if they confirm the conclusions of this work, as well as provide additional small cations systems such as holmium to study. Some X-ray total scattering measurements were performed on these systems, but as with the Ln_2ScNbO_7 systems there was insufficient contrast between ions to refine the B-site correlations.

Additionally, doping series could be investigated to look at the transition of the parent compound to charge disordered phase. For example it may be worth investigating the $Nd_2Sc_xNb_xZr_{2-x}O_7$ system to see if the increase in moment order is continuous in the transition between compounds. In general, this method of doping could allow for the transition between charge disordered and parent compounds to be investigated.

Bibliography

(1) Keimer, B; Moore, J. *Nature Physics* **2017**, *13*, 1045–1055.

(2) Moore, J. E. *Nature* **2010**, *464*, 194–198.

(3) Bolotin, K. I.; Ghahari, F.; Shulman, M. D.; Stormer, H. L.; Kim, P. *Nature* **2009**, *462*, 196–199.

(4) Venema, L.; Verberck, B.; Georgescu, I.; Prando, G.; Couderc, E.; Milana, S.; Maragkou, M.; Persechini, L.; Pacchioni, G.; Fleet, L. *Nature Physics* **2016**, *12*, 1085–1089.

(5) Tokura, Y.; Kawasaki, M.; Nagaosa, N. *Nature Physics* **2017**, *13*, 1056–1068.

(6) Samarth, N. *Nature Materials* **2017**, *16*, 1068–1076.

(7) Balents, L. *Nature* **2010**, *464*, 199–208.

(8) Castelnovo, C.; Moessner, R.; Sondhi, S. L. *Nature* **2008**, *451*, 42–45.

(9) Rao, C.; Nagarajan, R; Vijayaraghaven, R *Superconductor Science and Technology* **1993**, *6*, 1.

(10) Freedman, D. E.; Han, T. H.; Prodi, A.; Muller, P.; Huang, Q.-Z.; Chen, Y.-S.; Webb, S. M.; Lee, Y. S.; McQueen, T. M.; Nocera, D. G. *Journal of the American Chemical Society* **2010**, *132*, 16185–16190.

(11) Zhu, Z.; Maksimov, P.; White, S. R.; Chernyshev, A. *Physical Review Letters* **2017**, *119*, 157201.

(12) Taniguchi, T; Kadowaki, H.; Takatsu, H.; Fåk, B; Ollivier, J; Yamazaki, T.; Sato, T.; Yoshizawa, H; Shimura, Y; Sakakibara, T, et al. *Physical Review B* **2013**, *87*, 060408.

(13) Kermarrec, E; Maharaj, D.; Gaudet, J; Fritsch, K; Pomaranski, D; Kycia, J.; Qiu, Y.; Copley, J.; Couchman, M.; Morningstar, A., et al. *Physical Review B* **2015**, *92*, 245114.

(14) Baroudi, K.; Gaulin, B. D.; Lapidus, S. H.; Gaudet, J.; Cava, R. *Physical Review B* **2015**, *92*, 024110.

(15) Gardner, J. S.; Gingras, M. J.; Greedan, J. E. *Reviews of Modern Physics* **2010**, *82*, 53.

(16) Ahrens, L. H. *Geochimica et cosmochimica Acta* **1952**, *2*, 155–169.

(17) Wiebe, C. R.; Hallas, A. M. *APL materials* **2015**, *3*, 041519.

(18) Shannon, R. D. *Acta crystallographica section A: crystal physics, diffraction, theoretical and general crystallography* **1976**, *32*, 751–767.

(19) Moessner, R.; Chalker, J. T. *Physical Review Letters* **1998**, *80*, 2929.

(20) Palmer, S.; Chalker, J. *Physical Review B* **2000**, *62*, 488.

(21) Cotton, F. A., *Chemical applications of group theory*; John Wiley & Sons: 2003.

(22) Rau, J. G.; Gingras, M. J. *Annual Review of Condensed Matter Physics* **2019**.

(23) Li, Y.-D.; Wang, X.; Chen, G. *Physical Review B* **2016**, *94*, 201114.

(24) Benton, O. *Physical Review B* **2016**, *94*, 104430.

(25) Stewart, J.; Ehlers, G; Wills, A.; Bramwell, S. T.; Gardner, J. *Journal of Physics: Condensed Matter* **2004**, *16*, L321.

(26) Malkin, B.; Lummen, T.; Van Loosdrecht, P.; Dhalenne, G; Zakirov, A. *Journal of Physics: Condensed Matter* **2010**, *22*, 276003.

(27) Gaudet, J.; Smith, E.; Dudemaine, J; Beare, J.; Buhariwalla, C.; Butch, N. P.; Stone, M. B.; Kolesnikov, A. I.; Xu, G.; Yahne, D., et al. *Physical Review Letters* **2019**, *122*, 187201.

(28) Kimura, K.; Nakatsuji, S; Wen, J.; Broholm, C; Stone, M. B.; Nishibori, E; Sawa, H *Nature Communications* **2013**, *4*, 1–6.

(29) Yasui, Y.; Soda, M.; Iikubo, S.; Ito, M.; Sato, M.; Hamaguchi, N.; Matsushita, T.; Wada, N.; Takeuchi, T.; Aso, N., et al. *Journal of the Physical Society of Japan* **2003**, *72*, 3014–3015.

(30) Gingras, M. J.; McClarty, P. A. *Reports on Progress in Physics* **2014**, *77*, 056501.

(31) Bramwell, S. T.; Gingras, M. J. *Science* **2001**, *294*, 1495–1501.

(32) Norman, M. *Reviews of Modern Physics* **2016**, *88*, 041002.

(33) Han, T.-H.; Helton, J. S.; Chu, S.; Nocera, D. G.; Rodriguez-Rivera, J. A.; Broholm, C.; Lee, Y. S. *Nature* **2012**, *492*, 406–410.

(34) Han, T.-H.; Norman, M.; Wen, J.-J.; Rodriguez-Rivera, J. A.; Helton, J. S.; Broholm, C.; Lee, Y. S. *Physical Review B* **2016**, *94*, 060409.

(35) Paddison, J. A.; Daum, M.; Dun, Z.; Ehlers, G.; Liu, Y.; Stone, M. B.; Zhou, H.; Mourigal, M. *Nature Physics* **2017**, *13*, 117–122.

(36) Zhang, X.; Mahmood, F.; Daum, M.; Dun, Z.; Paddison, J. A.; Laurita, N. J.; Hong, T.; Zhou, H.; Armitage, N.; Mourigal, M. *Physical Review X* **2018**, *8*, 031001.

(37) Blanchard, P. E.; Clements, R.; Kennedy, B. J.; Ling, C. D.; Reynolds, E.; Avdeev, M.; Stampfl, A. P.; Zhang, Z.; Jang, L.-Y. *Inorganic Chemistry* **2012**, *51*, 13237–13244.

(38) Hallas, A. $Ho_2Ge_2O_7$ and $Pr_2Zr_2O_7$: a tale of two spin ices, 2013.

(39) Blanchard, P. E.; Liu, S.; Kennedy, B. J.; Ling, C. D.; Avdeev, M.; Aitken, J. B.; Cowie, B. C.; Tadich, A. *The Journal of Physical Chemistry C* **2013**, *117*, 2266–2273.

(40) Koohpayeh, S. M.; Wen, J.-J.; Trump, B. A.; Broholm, C. L.; McQueen, T. M. *Journal of Crystal Growth* **2014**, *402*, 291–298.

(41) Ross, K. A.; Yaraskavitch, L. R.; Laver, M.; Gardner, J. S.; Quilliam, J. A.; Meng, S; Kycia, J. B.; Singh, D. K.; Proffen, T. h.; Dabkowska, H. A., et al. *Physical Review B* **2011**, *84*, 174442.

(42) Lau, G. C.; Freitas, R. S.; Ueland, B. G.; Muegge, B. D.; Duncan, E. L.; Schiffer, P; Cava, R. J. *Nature Physics* **2006**, *2*, 249–253.

(43) Ehlers, G.; Gardner, J. S.; Qiu, Y; Fouquet, P; Wiebe, C. R.; Balicas, L; Zhou, H. D. *Physical Review B* **2008**, *77*, 052404.

(44) Sanders, M.; Krizan, J.; Plumb, K.; McQueen, T.; Cava, R. *Journal of Physics: Condensed Matter* **2016**, *29*, 045801.

(45) Ross, K. A.; Krizan, J. W.; Rodriguez-Rivera, J. A.; Cava, R. J.; Broholm, C. L. *Physical Review B* **2016**, *93*, 014433.

(46) Zouari, S.; Ballou, R.; Cheikh-Rouhou, A.; Strobel, P. *Materials Letters* **2008**, *62*, 3767–3769.

(47) Strobel, P.; Zouari, S.; Ballou, R.; Cheikh-Rouhou, A.; Jumas, J.-C.; Olivier-Fourcade, J. *Solid State Sciences* **2010**, *12*, 570–577.

(48) Ke, X; Ueland, B. G.; West, D. V.; Dahlberg, M. L.; Cava, R. J.; Schiffer, P *Physical Review B* **2007**, *76*, 214413.

(49) Hodges, J.; de Réotier, P. D.; Yaouanc, A; Gubbens, P.; King, P.; Baines, C *Journal of Physics: Condensed Matter* **2011**, *23*, 164217.

(50) Kobayashi, Y; Miyashita, T; Fukamachi, T; Sato, M *Journal of Physics and Chemistry of Solids* **2001**, *62*, 347–350.

(51) West, A. R., *Solid state chemistry and its applications*; John Wiley & Sons: 2014.

(52) Subramani, S., *Basics of single crystal growth techniques*; Lap Lambert Academic Publishing: 2017; Vol. 1.

(53) Kittel, C.; McEuen, P., *Introduction to Solid State Physics*; Wiley New York: 1976; Vol. 8.

(54) Ashcroft, N. W.; Mermin, N. D., et al. Solid state physics [by] Neil W. Ashcroft [and] N. David Mermin. 1976.

(55) Rodríguez-Carvajal, J. *Physica B* **1993**, *192*, 55–69.

(56) Toby, B. H.; Von Dreele, R. B. *Journal of Applied Crystallography* **2013**, *46*, 544–549.

(57) Siddons, D. P.; Hulbert, S. L.; Stephens, P. W. In *AIP Conference Proceedings*, 2007; Vol. 879, pp 1767–1770.

(58) Furrer, A.; Mesot, J. F.; Strässle, T., *Neutron scattering in condensed matter physics*; World Scientific Publishing Company: 2009; Vol. 4.

(59) Lynn, J. W. *Journal of Applied Physics* **1994**, *75*, 6806–6810.

(60) Wills, A. S. *Physica B: Condensed Matter* **2000**, *276*, 680–681.

(61) Wills, A *Le Journal de Physique IV* **2001**, *11*, Pr9–133.

(62) Takeshi, E.; Billinge, S. J. In *Pergamon Materials Series*; Elsevier: 2012; Vol. 16, pp 55–111.

(63) Tucker, M. G.; Keen, D. A.; Dove, M. T.; Goodwin, A. L.; Hui, Q. *Journal of Physics: Condensed Matter* **2007**, *19*, 335218.

(64) Stewart, J. R.; Deen, P. P.; Andersen, K. H.; Schober, H; Barthélémy, J.-F.; Hillier, J. M.; Murani, A. P.; Hayes, T; Lindenau, B *Journal of Applied Crystallography* **2009**, *42*, 69–84.

(65) Neuefeind, J.; Feygenson, M.; Carruth, J.; Hoffmann, R.; Chipley, K. K. *Nuclear Instruments and Methods in Physics Research Section B: Beam Interactions with Materials and Atoms* **2012**, *287*, 68–75.

(66) Paddison, J. A.; Stewart, J. R.; Goodwin, A. L. *Journal of Physics: Condensed Matter* **2013**, *25*, 454220.

(67) Blech, I. A.; Averbach, B. *Physics Physique Fizika* **1964**, *1*, 31.

(68) Boothroyd, A. T. SPECTRE-a computer program for calculating spectroscopic properties of rare-earth ions in crystals (1990-2014).

(69) Walter, U *Journal of Physics and Chemistry of Solids* **1984**, *45*, 401–408.

(70) Hutchings, M. T. In *Solid state physics*; Elsevier: 1964; Vol. 16, pp 227–273.

(71) Rotter, M et al. McPHASE, a software package for the calculation of phase diagrams and magnetic properties of rare-earth systems, 2002-2008.

(72) Toth, S; Lake, B *Journal of Physics: Condensed Matter* **2015**, *27*, 166002.

(73) Xu, G.; Xu, Z.; Tranquada, J. *Review of Scientific Instruments* **2013**, *84*, 083906.

(74) Quantum Design VSM Brochure, https://www.qdusa.com/siteDocs/productBrochures/1084-500_PPMS_VSM.pdf.

(75) Quantum Design Physical Property Measurement System: Heat Capacity Option User's Manual.

(76) Mauws, C.; Hiebert, N.; Rutherford, M.; Zhou, H. D.; Huang, Q.; Stone, M. B.; Butch, N. P.; Su, Y.; Choi, E. S.; Yamani, Z.; Wiebe, C. R. *Journal of Physics: Condensed Matter* **2021**, *33*, 245802.

(77) Sarin, P.; Hughes, R. W.; Lowry, D. R.; Apostolov, Z. D.; Kriven, W. M. *Journal of the American Ceramic Society* **2014**, *97*, 3307–3319.

(78) Farrow, C.; Juhas, P; Liu, J.; Bryndin, D; Božin, E.; Bloch, J; Proffen, T.; Billinge, S. *Journal of Physics: Condensed Matter* **2007**, *19*, 335219.

(79) Fennell, T; Harris, M.; Calder, S; Ruminy, M; Boehm, M; Steffens, P; Lemée-Cailleau, M.-H.; Zaharko, O; Cervellino, A; Bramwell, S. *Nature Physics* **2019**, *15*, 60.

(80) Fairbank, V. E.; Thompson, A. L.; Cooper, R. I.; Goodwin, A. L. *Physical Review B* **2012**, *86*, 104113.

(81) Sears, V. F. *Neutron News* **1992**, *3*, 26–37.

(82) Petit, S.; Lhotel, E.; Canals, B.; Ciomaga Hatnean, M.; Ollivier, J.; Mutka, H.; Ressouche, E.; Wildes, A. R.; Lees, M. R.; Balakrishnan, G. *Nature Physics* **2016**, *12*, 746–750.

(83) Anand, V. K.; Abernathy, D. L.; Adroja, D. T.; Hillier, A. D.; Biswas, P. K.; Lake, B *Physical Review B* **2017**, *95*, 224420.

(84) Brooks-Bartlett, M.; Banks, S. T.; Jaubert, L. D.; Harman-Clarke, A.; Holdsworth, P. C. *Physical Review X* **2014**, *4*, 011007.

(85) Sala, G; Gutmann, M.; Prabhakaran, D; Pomaranski, D; Mitchelitis, C; Kycia, J.; Porter, D.; Castelnovo, C; Goff, J. *Nature Materials* **2014**, *13*, 488–493.

(86) Ladak, S.; Read, D.; Branford, W.; Cohen, L. *New Journal of Physics* **2011**, *13*, 063032.

(87) Granroth, G.; Kolesnikov, A.; Sherline, T.; Clancy, J.; Ross, K.; Ruff, J.; Gaulin, B.; Nagler, S. In *Journal of Physics: Conference Series*, 2010; Vol. 251, p 012058.

(88) Bain, G. A.; Berry, J. F. *Journal of Chemical Education* **2008**, *85*, 532.

(89) Schweika, W; Böni, P *Physica B: Condensed Matter* **2001**, *297*, 155–159.

(90) Copley, J.; Cook, J. *Chemical Physics* **2003**, *292*, 477–485.

(91) Xu, J.; Anand, V. K.; Bera, A. K.; Frontzek, M.; Abernathy, D. L.; Casati, N.; Siemensmeyer, K.; Lake, B. *Phys. Rev. B* **2015**, *92*, 224430.

(92) Huang, Y.-P.; Chen, G.; Hermele, M. *Physical Review Letters* **2014**, *112*, 167203.

(93) Canals, B.; Lacroix, C. *Physical Review Letters* **1998**, *80*, 2933.

(94) Raju, N.; Dion, M; Gingras, M.; Mason, T.; Greedan, J. *Physical Review B* **1999**, *59*, 14489.

(95) Del Maestro, A.; Gingras, M. J. *Physical Review B* **2007**, *76*, 064418.

(96) Wills, A.; Zhitomirsky, M.; Canals, B; Sanchez, J. P.; Bonville, P; de Réotier, P. D.; Yaouanc, A *Journal of Physics: Condensed Matter* **2006**, *18*, L37.

(97) Paddison, J. A.; Cairns, A. B.; Khalyavin, D. D.; Manuel, P.; Daoud-Aladine, A.; Ehlers, G.; Petrenko, O. A.; Gardner, J. S.; Zhou, H.; Goodwin, A. L., et al. *arXiv preprint arXiv:1506.05045* **2015**.

(98) Gardner, J.; Stewart, J.; Ehlers, G In *AIP Conference Proceedings*, 2010; Vol. 1202, pp 3–7.

(99) Li, X; Cai, Y.; Cui, Q; Lin, C.; Dun, Z.; Matsubayashi, K; Uwatoko, Y; Sato, Y; Kawae, T.; Lv, S., et al. *Physical Review B* **2016**, *94*, 214429.

(100) Bonville, P; Hodges, J. A.; Ocio, M; Sanchez, J.; Vulliet, P; Sosin, S; Braithwaite, D *Journal of Physics: Condensed Matter* **2003**, *15*, 7777.

(101) Hallas, A. M.; Arevalo-Lopez, A. M.; Sharma, A. Z.; Munsie, T; Attfield, J. P.; Wiebe, C. R.; Luke, G. M. *Physical Review B* **2015**, *91*, 104417.

(102) Mauws, C. *To be published* **2021**.

(103) Mydosh, J. A., *Spin glasses: an experimental introduction*; Taylor & Francis: 1993.

(104) Huang, C. *Journal of Magnetism and Magnetic Materials* **1985**, *51*, 1–74.

(105) Zhou, H. D.; Wiebe, C. R.; Harter, A; Dalal, N. S.; Gardner, J. S. *Journal of Physics: Condensed Matter* **2008**, *20*, 325201.

(106) Mydosh, J. A., *Spin glasses: an experimental introduction*; CRC Press: 2014.

(107) Cywinski, R.; Kilcoyne, S. H.; Lee, S. L., *Muon science: muons in physics, chemistry, and materials ; proceedings of the Fifty First Scottish Universities Summer School in Physics, St. Andrews, August 1998*; Scottish Universities Summer School in Physics.

(108) Dunsiger, S. R.; Kiefl, R. F.; Chakhalian, J. A.; Greedan, J. E.; Macfarlane, W. A.; Miller, R. I.; Morris, G. D.; Price, A. N.; Raju, N. P.; Sonier, J. E.; et al. *Physical Review B* **2006**, *73*, DOI: 10.1103/physrevb.73.172418.

(109) Dunsiger, S. R.; Kiefl, R. F.; Chow, K. H.; Gaulin, B. D.; Gingras, M. J. P.; Greedan, J. E.; Keren, A.; Kojima, K.; Luke, G. M.; Macfarlane, W. A.; et al. *Journal of Applied Physics* **1996**, *79*, 6636.

(110) Dunsiger, S. R.; Kiefl, R. F.; Chow, K. H.; Gaulin, B. D.; Gingras, M. J. P.; Greedan, J. E.; Keren, A.; Kojima, K.; Luke, G. M.; MacFarlane, W. A.; Raju, N. P.; Sonier, J. E.; Uemura, Y. J.; Wu, W. D. *Phys. Rev. B* **1996**, *54*, 9019–9022.

(111) Paddison, J. A.; Ehlers, G.; Petrenko, O. A.; Wildes, A. R.; Gardner, J. S.; Stewart, J. R. *Journal of Physics: Condensed Matter* **2017**, *29*, 144001.

(112) Shinaoka, H.; Tomita, Y.; Motome, Y. *Physical Review Letters* **2011**, *107*, 047204.

(113) Bellier-Castella, L; Gingras, M. J.; Holdsworth, P. C.; Moessner, R *Canadian Journal of Physics* **2001**, *79*, 1365–1371.

(114) Silverstein, H.; Fritsch, K; Flicker, F; Hallas, A.; Gardner, J. S.; Qiu, Y.; Ehlers, G; Savici, A.; Yamani, Z; Ross, K., et al. *Physical Review B* **2014**, *89*, 054433.

(115) Thygesen, P. M.; Paddison, J. A.; Zhang, R.; Beyer, K. A.; Chapman, K. W.; Playford, H. Y.; Tucker, M. G.; Keen, D. A.; Hayward, M. A.; Goodwin, A. L. *Physical Review Letters* **2017**, *118*, 067201.

(116) Ratcliff, W.; Lee, S.-H.; Broholm, C.; Cheong, S.-W.; Huang, Q. *Phys. Rev. B* **2002**, *65*, 220406.

(117) Den Hertog, B. C.; Gingras, M. J. *Physical Review Letters* **2000**, *84*, 3430.

(118) Bramwell, S. T.; Gingras, M. J. P. *Science* **2001**, *294*, 1495.

(119) Ramirez, A. P.; Hayashi, A; Cava, R. J.; Siddharthan, R; Shastry, B. *Nature* **1999**, *399*, 333–335.

(120) Zhou, H. D.; Cheng, J. G.; Hallas, A. M.; Wiebe, C. R.; Li, G; Balicas, L; Zhou, J. S.; Goodenough, J. B.; Gardner, J. S.; Choi, E. S. *Physical Review Letters* **2012**, *108*, 207206.

(121) Cui, Q.; Cai, Y.-Q.; Li, X.; Dun, Z.-L.; Sun, P.-J.; Zhou, J.-S.; Zhou, H.-D.; Cheng, J.-G. *Chinese Physics B* **2020**, *29*, 047502.

(122) Den Hertog, B. C.; Gingras, M. J. P. *Phys. Rev. Lett.* **2000**, *84*, 3430–3433.

(123) Pomaranski, D; Yaraskavitch, L. R.; Meng, S; Ross, K. A.; Noad, H. M.; Dabkowska, H. A.; Gaulin, B. D.; Kycia, J. B. *Nature Physics* **2013**, *9*, 353–356.

(124) Castelnovo, C.; Moessner, R.; Sondhi, S. L. *Nature* **2008**, *451*, 42–45.

(125) Paulsen, C.; Giblin, S. R.; Lhotel, E.; Prabhakaran, D; Balakrishnan, G.; Matsuhira, K; Bramwell, S. T. *Nature Physics* **2016**, *12*, 661–666.

(126) Morris, D. J. P.; Tennant, D.; Grigera, S.; Klemke, B; Castelnovo, C; Moessner, R; Czternasty, C; Meissner, M; Rule, K.; Hoffmann, J.-U., et al. *Science* **2009**, *326*, 411–414.

(127) Rutherford, M. Thesis, to be published, McMaster University, 2021.

(128) Abernathy, D. L.; Stone, M. B.; Loguillo, M.; Lucas, M.; Delaire, O; Tang, X.; Lin, J.; Fultz, B *Review of Scientific Instruments* **2012**, *83*, 015114.

(129) Ke, X; Dahlberg, M. L.; Morosan, E; Fleitman, J. A.; Cava, R. J.; Schiffer, P *Physical Review B* **2008**, *78*, 104411.

(130) Jana, Y. M.; Sengupta, A; Ghosh, D *Journal of Magnetism and Magnetic Materials* **2002**, *248*, 7–18.

(131) Lau, G. C.; Muegge, B. D.; McQueen, T. M.; Duncan, E. L.; Cava, R. J. *Journal of Solid State Chemistry* **2006**, *179*, 3126–3135.

(132) Bramwell, S. T.; Field, M. N.; Harris, M. J.; Parkin, I. P. *Journal of Physics: Condensed Matter* **2000**, *12*, 483.

(133) Ruminy, M; Pomjakushina, E; Iida, K; Kamazawa, K; Adroja, D. T.; Stuhr, U; Fennell, T *Physical Review B* **2016**, *94*, 024430.

(134) Hallas, A. M.; Paddison, J. A.; Silverstein, H. J.; Goodwin, A. L.; Stewart, J. R.; Wildes, A. R.; Cheng, J. G.; Zhou, J. S.; Goodenough, J. B.; Choi, E. S., et al. *Physical Review B* **2012**, *86*, 134431.

(135) Matsubara, F; Shirakura, T; Endoh, S; Takahashi, S *Journal of Physics A: Mathematical and General* **2003**, *36*, 10881.

(136) Takeshi, E.; Billinge, S. J. In *Pergamon Materials Series*; Elsevier: 2012; Vol. 16, pp 325–369.

(137) Egami, T.; Billinge, S. J., *Underneath the Bragg peaks: structural analysis of complex materials*; Elsevier: 2003.

(138) Singh, S.; Saha, S.; Dhar, S. K.; Suryanarayanan, R.; Sood, A. K.; Revcolevschi, A. *Phys. Rev. B* **2008**, *77*, 054408.

(139) Mauws, C.; Hallas, A.; Sala, G.; Aczel, A. A.; Sarte, P.; Gaudet, J; Ziat, D; Quilliam, J.; Lussier, J.; Bieringer, M, et al. *Physical Review B* **2018**, *98*, 100401.

(140) Peçanha-Antonio, V.; Feng, E.; Sun, X.; Adroja, D.; Walker, H. C.; Gibbs, A. S.; Orlandi, F.; Su, Y.; Brückel, T. *Physical Review B* **2019**, *99*, 134415.

(141) Fernandez-Baca, J. A.; Lumsden, M. D.; Winn, B.; Zarestky, J; Zheludev, A *Neutron News* **2008**, *19*, 18–21.

(142) Rotter, M *Journal of Magnetism and Magnetic Materials* **2004**, *272*, E481–E482.

(143) Xu, J. Magnetic properties of rare earth zirconate pyrochlores, Technische Universität Berlin, 2017.

(144) Champion, J.; Harris, M.; Holdsworth, P.; Wills, A.; Balakrishnan, G.; Bramwell, S.; Čižmár, E; Fennell, T; Gardner, J.; Lago, J, et al. *Physical Review B* **2003**, *68*, 020401.

(145) Li, Y.; Adroja, D.; Bewley, R. I.; Voneshen, D.; Tsirlin, A. A.; Gegenwart, P.; Zhang, Q. *Physical Review Letters* **2017**, *118*, 107202.

(146) Lima, M. P. *Journal of Physics: Condensed Matter* **2019**, *32*, 025505.